



GRAN SASSO SCIENCE INSTITUTE

DEPARTMENT OF ASTROPARTICLE PHYSICS

XXX CYCLE - 2014/2018 PHD THESIS

**Sensitivity of the
KM3NeT/ARCA Phase-1 detector
to a diffuse neutrino emission from
the Southern sky**

Mora Durocher

PhD supervisor

Dr. Rosa CONIGLIONE

PhD advisors

Dr. Piera SAPIENZA

Dr. Luciano PANDOLA

1. Reviewer: Dr. Elisa BERNARDINI

2. Reviewer: Dr. Isabelle LHENRY-YVON

3. Reviewer: Dr. Paolo DESIATI

Day of the defense: November 9th 2018

Signature from head of PhD committee

Dr. Roberta SPARVOLI

Dr. Edvige CORBELLI

Dr. Ivan DE MITRI

Dr. Pasquale BLASI

Dr. Piero ULLIO

Abstract

KM3NeT is a large research infrastructure that will host two deep-sea neutrino detectors in the Mediterranean Sea. The ORCA (Oscillation Research with Cosmics in the Abyss) detector, which will be located 40 km offshore Toulon (France), is optimised for the study of atmospheric neutrino oscillations. Whereas the ARCA (Astroparticle Research with Cosmics in the Abyss) detector, which will be located 80 km offshore Capo Passero (Italy), is dedicated to the search for high-energy neutrinos (above 1 TeV) from astrophysical sources. Moreover ARCA will explore the IceCube signal from a different field of view, with an improved angular resolution and different systematic uncertainties.

A grid of thousands of sensitive optical sensors will detect the faint Cherenkov light produced by relativistic charged particles emerging from neutrino interactions. The collected photon arrival times and the spatial positions of these sensors are used to reconstruct the direction of the neutrinos and to associate them with potential distant cosmic sources. The ARCA detector will consist of two structures called “building blocks”. Each building block is composed of 115 strings and each string comprises 18 large spherical sensors, called “digital optical modules”. The novel design of these digital optical modules helps to optimize the photocathode area by implementing 31 small photomultiplier tubes within a glass sphere and makes it possible, with only one digital optical module, to identify atmospheric muon events.

Once completed, the ARCA installation will add up to an instrumented volume of about 1 km³. The first construction phase of ARCA will consist of 24 strings and will subsequently amount to an instrumented volume of about 0.1 km³. The underwater neutrino detector can start taking data from the deployment of the first string. At the Capo Passero site, two strings have been deployed and the first results demonstrate the ability to efficiently reconstruct events, which were then compared to Monte Carlo simulations. The excellent agreement between data and Monte Carlo

simulations confirms the ability to accurately reproduce the detector's performance.

The purpose of this work is to predict the capabilities of the first 24 strings of the ARCA detector by relying on Monte Carlo simulations. The work reported in this thesis focuses on the evaluation of the discovery potential of ARCA Phase-1 to the muon neutrino diffuse flux by selecting the upgoing muon tracks which cross the detector volume. The reconstruction of the muon tracks with respect to the direction of the incident muon neutrinos is performant enough to achieve an angular resolution better than 0.15° at high energies (above 10 TeV). Furthermore, the detection of the IceCube isotropic diffuse flux at 3σ significance level is expected to be achieved within some 4 years (about 10 years at 5σ). Two techniques were applied to optimize event selection by using track reconstruction parameters and to derive the corresponding discovery flux with suitable significance.

This work concludes that, in spite of the detector's size at this first construction phase, interesting scientific findings can be expected from the ARCA installation with reasonable sensitivity. Improved results can be obtain by performing a multivariate analysis to better identify background events and also by taking into account cascade-like events.

To my parents, who have given everything for me to pursue this path. To my mother, for her full support throughout this venture; and to my father, who nurtured the seed of curiosity and always pushed me forward.

Acknowledgements

I would like to show appreciation to the individuals who have helped me throughout my thesis. It is due to their efforts that I have reached this point today. Starting with the fine people in l'Aquila, I would like to thank Francesco Vissani, not only for welcoming me into this program but also for helping me find the means to move forward. I would also like to thank all the other PhD students of GSSI for making my stay there extremely enjoyable.

Progressing to LNS, I would like to thank my supervisor Rosa Coniglione for always pointing me in the right direction, for assisting me through all the fine details and for her invaluable guidance. I would also like to thank Luciano Pandola for his counsel during my stay at GSSI and at LNS, and for facilitating my integration to both agencies. I would also like to thank Girogio Riccobene, Simone Biagi, Agata Trovato and Salvatore Viola for providing me with useful directions and lasting friendship.

Last but not least, I would like to thank the members of the KM3NeT collaboration for accepting me in their midst and for inspiring me at each and every meeting I've attended.

Contents

Abstract	iii
Introduction	1
1 HIGH-ENERGY NEUTRINO DETECTION	5
1.1 Detection Principles	6
1.1.1 High-Energy Neutrino Interactions	6
1.1.2 Muon Propagation	13
1.1.3 Cherenkov Radiation	14
1.1.4 Light Transmission Properties	15
1.2 Background	17
1.2.1 Environmental Optical Background	17
1.2.2 Physical Background	21
1.3 Cherenkov Neutrino Telescopes	23
1.3.1 NESTOR and NEMO	23
1.3.2 ANTARES	25
1.3.3 ICECUBE	26
2 THE KM3NET DETECTOR	29

CONTENTS

2.1	The Installation Sites	31
2.2	Building Blocks and Detection Units	33
2.3	Digital Optical Modules and PhotoMultiplier Tubes	37
2.4	Time Calibration	41
2.4.1	Intra-DOM Calibration	42
2.4.2	Inter-DOM Calibration	44
2.5	First Results	47
2.5.1	PPM-DU	47
2.5.2	DU1 and DU2	48
3	HIGH-ENERGY NEUTRINO ASTRONOMY	51
3.1	Cosmic-Rays	52
3.2	Neutrino Astronomy	56
3.2.1	Neutrinos from Hadronic Processes	56
3.2.2	Astrophysical Neutrino Sources	59
3.3	Models and Limits	63
3.3.1	Waxman-Bahcall	64
3.3.2	Mannheim-Protheroe-Rachen	64
3.3.3	IceCube Results and Flux Assumptions	65
3.4	Atmospheric Neutrinos	73
4	SIMULATION AND RECONSTRUCTION TOOLS	79
4.1	Simulation Tools	81
4.1.1	Detector Geometry	81

4.1.2	Generation of Neutrino Events	81
4.1.3	Generation of Atmospheric Muons	87
4.1.4	Propagation of Particles and Light Production	88
4.1.5	Generation of Optical Background and Triggering	92
4.2	Reconstruction Tool	93
4.2.1	JGandalf Chain	97
4.2.2	Reconstruction Parameters	100
5	PERFORMANCE ANALYSIS	105
5.1	Neutrino Effective Areas	105
5.1.1	Neutrino Effective Volume	106
5.1.2	Neutrino Effective Area	107
5.2	Energy and Angular Resolution	108
5.2.1	Energy Resolution	108
5.2.2	Angular Resolution	109
5.3	Search Methods	110
5.3.1	Discovery Potential with the Cut-and-Count Method	111
5.3.2	Sensitivity with the Cut-and-Count Method	112
5.3.3	Likelihood Ratio Test	113
5.4	Results	115
5.4.1	Event Generation	115
5.4.2	Pre-Selection Cut	116
5.4.3	Results from the Cut-and-Count Method	119

CONTENTS

5.4.4	Results from the Likelihood Ratio test	121
5.4.5	Resulting Energy and Angular Resolution	126
	Conclusion	131
	References	133

INTRODUCTION

Violent phenomena are some of the most intriguing events in the universe despite being so little understood. The high-energy diffuse photon flux observed from Earth confirms the strong occurrence of these events but the extent of knowledge on the matter is somewhat limited. They are a considerable challenge for astroparticle physicists but one that is gladly accepted.

Consequently, high-energy messengers - hadrons, gamma rays, gravitational waves and neutrinos - are adopted to communicate as much information as possible on these phenomena. In 2013, the IceCube collaboration had made some essential advancements in this field by observing a series of high energy neutrino candidates from an extraterrestrial origin at a significant statistical level. These 28 events were rejected to originate from a purely atmospheric background at a 4σ level. Despite not being able to pinpoint the exact extraterrestrial sources, as the detected neutrinos were scarce in time and space, this announcement was nevertheless a major turning point in astroparticle physics. It is now crucial for other detectors to corroborate these findings.

To achieve a better understanding of the high-energy Universe and of the mechanisms responsible for the production of high-energy particles, observations using different techniques and probes are vital. Neutrinos are exceptional messengers for that purpose since they interact only weakly with matter and are not influenced by interstellar magnetic fields. They can consequently travel very long inter-stellar and inter-galactic distances without being deflected or absorbed. However the comparatively low fluxes and small interaction probabilities make the detection of high-energy neutrinos challenging. In 1960, Markov and Zheleznykh proposed that one way to detect high-energy neutrinos was to consider huge volumes of natural material, such as ice or seawater.

CONTENTS

Neutrino astronomy would thus be able to provide information from violent astrophysical processes, obscure to high-energy gamma-rays and charged particles. By piecing together information from cosmic-ray, neutrino and gamma-ray telescopes the search for a coherent picture of the inner workings of astrophysical objects continues. The observations of cosmic-rays with energies up to some 10^{20} eV proves the existence of astrophysical phenomena able to accelerate hadrons up to extreme energies and whose interaction with surrounding particles could produce neutrinos. The latter are expected to exhibit the same energy spectrum as the accelerated cosmic parent particles, which follow a harder energy spectrum than most neutrinos generated in the Earth's atmosphere.

A large number of high-energy neutrino sources are believed to be located in our Milky Way galaxy such as SuperNova Remnants, Pulsar Wind Nebulae, X-ray binaries and microquasars. Active Galactic Nuclei and Gamma Ray Bursts are among the extra-galactic objects that could be producing neutrinos. They are all considered possible sources in which particles are accelerated to high energies through shock acceleration processes. The prediction of the diffuse neutrino flux from unresolved astrophysical sources is based on cosmic ray (CR) and gamma-ray observations. Furthermore, considering the combination of these unresolved sources of high-energy neutrinos, their integrated flux can be detected before the flux of any individual source can reach the detection threshold.

Neutrino detection is an indirect process, made possible via the charged leptons produced in weak charged current interactions between neutrinos and the nucleons of the considered medium. In transparent media, tracks of relativistic particles can be reconstructed by using the generated Cherenkov radiation, which can be seen by a three-dimensional grid of optical sensors. Among neutrino flavors, muon neutrinos are the favored probe for astrophysics, since muons' range in water reaches up to several kilometers at the energies of interest. This allows a more precise reconstruction of their direction and an effective volume higher than the instrumented volume. Furthermore, at high energies, the neutrino and the muon it creates are almost collinear and a measurement of the direction of the muon passing through the detector gives an accurate estimation of the neutrino that produced it.

Following the scientific results obtained with the ANTARES neutrino telescope and

the insight acquired from the NESTOR and NEMO pilot projects, the KM3NeT collaboration has launched the installation of the next generation km³ deep-sea neutrino telescope in the Mediterranean Sea. From its favorable location in the Northern hemisphere, the KM3NeT detector will be able to map 87% of the sky, including most of our Galaxy and the Galactic Center. It will consist of a grid of thousands of sensitive optical sensors called “digital optical modules” (DOMs), whose novel design makes it possible to optimize the photo-cathode area by implementing 31 small photomultiplier tubes (PMTs) within a 17-inch diameter glass sphere.

KM3NeT will host two deep-sea neutrino detectors: the ORCA (Oscillation Research with Cosmics in the Abyss) component and the ARCA (Astroparticle Research with Cosmics in the Abyss) component. ORCA will be located 40 km offshore Toulon (France) and is meant to study the fundamental properties of neutrinos, more specifically, ORCA is optimized to examine atmospheric neutrino oscillations. Whereas ARCA, which will be located 80 km offshore Capo Passero (Italy), is dedicated to finding high-energy neutrinos (above 1 TeV) from astrophysical sources, which includes neutrinos from the cosmic ray accelerators in our Galaxy. Moreover ARCA will explore the IceCube signal from a different field of view, with an improved angular resolution and different systematic uncertainties.

The ARCA detector will consist of two structures called “building blocks”. Each building block is composed of 115 strings and each string comprises 18 DOMs. The collected photon arrival times and the spatial positions of the DOMs are used to reconstruct the direction of the neutrinos and to associate them with potential distant cosmic sources. The first construction phase of the ARCA detector will consist of 24 strings, which amounts to an instrumented volume of about 0.1 km³.

The purpose of this work is to predict the capabilities of these first 24 strings of ARCA by relying on Monte Carlo simulations. In this thesis, the discovery potential and the sensitivity of ARCA Phase-1 to the muon neutrino diffuse flux are evaluated by selecting the upgoing muon tracks which cross the detector volume. This is done by considering two methods whose target is to confidently differentiate between weak signal events, originating from a diffuse neutrino flux, and a large background of atmospheric muons and neutrinos, both produced by the interaction of primary cosmic-rays with the atmosphere.

CONTENTS

The thesis is arranged as follows:

- Chapter 1 describes detection principles of high-energy neutrinos using Cherenkov radiation under-water(-ice). Some Mediterranean pilot projects and the Ice-Cube detector are also briefly introduced.
- In Chapter 2 some of the essential components of the KM3NeT detector are depicted. The time calibration procedures and the first results of the detection units in situ are reported.
- Chapter 3 puts forward the development of neutrino astronomy from the physics of cosmic rays. A swift overview of the candidate galactic and extra-galactic neutrino sources is presented. The limits and models of the estimated diffuse neutrino flux are put forward.
- Chapter 4 describes the simulation codes used to secure the events that will be employed in this work. This includes the codes which generate the incident neutrinos, their interaction in the medium and the propagation of the emerging secondary particles, the light generation and propagation in water, the detector's response and finally the track reconstruction algorithm.
- In Chapter 5 the performance analysis is carried out and the two implemented methods are explained. Then the results from both approaches are laid out.

Chapter 1

HIGH-ENERGY NEUTRINO DETECTION

High-energy neutrinos (above 1 TeV) can be detected indirectly by neutrino telescopes: the detection principle relies on measuring the Cherenkov radiation induced by high-energy charged particles that are produced in a neutrino interaction inside or near the instrumented volume. The extremely large detector volume needed to detect neutrinos from distances beyond our Sun make the use of any other material than water or ice very difficult (1). Tracks of relativistic particles can be reconstructed by detecting the light produced via the Cherenkov effect in transparent media with a three-dimensional network of optical sensors, using the hit time and position information of the photo-sensors.

In particular, high-energy muons which are produced in charged current muon-neutrino interactions can travel large distances (their range in water or rock is of several kilometers for $E_\mu \geq 1$ TeV). As a matter of fact they are massive enough ($m_\mu \sim 200 m_e$) not to lose all their energy via radiative processes, facilitating an accurate determination of the direction. In addition, at the typical neutrino energies considered, the direction of the muon closely follows that of the incident neutrino. For these reasons, neutrino telescopes are primarily designed for detecting ν_μ charged current interactions (considered as the “golden channel”) since the resulting muon has a long range in seawater and is almost colinear to the incident ν_μ . Electron and tau neutrinos can also be distinguished through the detection of their electromagnetic and hadronic cascade, resulting in a much lower angular accuracy. Neutral current interactions of high-energy neutrinos can also be detected by measuring their hadronic cascade.

Neutrinos arrive from all directions but only a small fraction of them will actually

1. HIGH-ENERGY NEUTRINO DETECTION

interact with the surrounding instrumented volume, as their cross section is exceptionally small. However, neutrino telescopes are not background free: the detector will typically look downward as downgoing neutrino-induced muons would be completely drowned by atmospheric muons and upgoing muons can only be produced by interactions of upgoing neutrinos. As atmospheric muons can only penetrate the atmosphere and up to several kilometres of ice or water (see Figure 1.15), only atmospheric neutrinos that have traversed the Earth represent an irreducible background for the study of cosmic neutrinos. Consequently, neutrino detectors must be located deeply under a large amount of shielding and search for upgoing events in order to reduce these backgrounds.

1.1 Detection Principles

Neutrinos are the neutral counterparts of the charged leptons: e , μ and τ , thus there are three types of “active” neutrinos in the Standard Model of particle physics: ν_e , ν_μ and ν_τ . Neutrinos are fermions, i.e. spin- $\frac{1}{2}$ particles. Apart from their gravitational interactions, neutrino weak force interactions with matter are divided in two kinds: Neutral Current (NC) interactions mediated by the neutral Z bosons and Charged Current (CC) interactions involving the exchange of W^+ and W^- bosons. As far as is known, they are fundamental particles without constituents, have extremely small masses ($m < 2$ eV) and lack electric charge ($\mu < 0.29 \times 10^{-10} \mu_B$).

Neutrino telescopes rely on some basic principles in order to efficiently detect high-energy neutrinos. Here these principles will be described, including the interactions undergone by high-energy neutrinos inside the detector volume, leaving distinct traces. The fundamentals of event reconstruction and the management of background events will also be explained.

1.1.1 High-Energy Neutrino Interactions

Neutrinos with energy higher than 20 GeV can interact with target nucleons mostly through deep inelastic scattering. As shown in Figure 1.1, Neutral Current (NC) interactions are similar for all flavors and different neutrinos flavors will produce different event classes. Thus the neutrino flavor and the type of interaction taking

place greatly affect the signature of the neutrino event seen by the detector. For NC interactions, the neutrino will react with a nucleon of the nucleus, resulting in a lower energy scattered neutrino and a hadronic shower; whereas the Charged Current (CC) interactions produce a relativistic charged lepton and a hadronic shower in the final state:

$$(NC) \quad \nu_l(\bar{\nu}_l) + N \rightarrow \nu_l(\bar{\nu}_l) + X \quad l = e, \mu, \tau \quad (1.1)$$

$$(CC) \quad \nu_l(\bar{\nu}_l) + N \rightarrow l(\bar{l}) + X \quad l = e, \mu, \tau \quad (1.2)$$

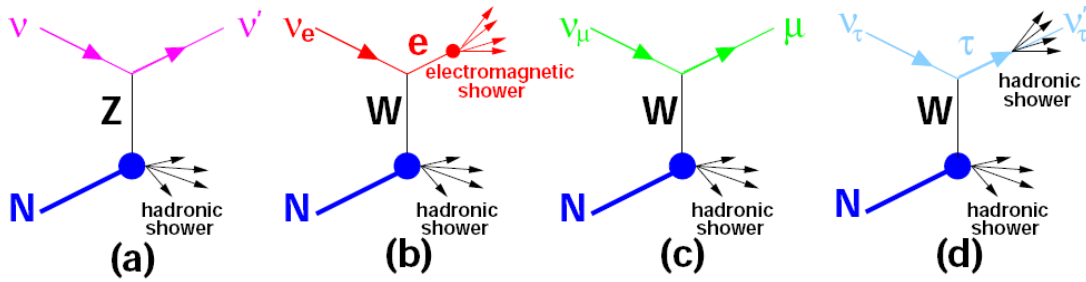


Figure 1.1: Depiction of neutrino interactions applicable to neutrino telescopes. (a) Neutral Current interaction, same for all flavors. (b) ν_e Charged Current interaction creating an electromagnetic shower. (c) ν_μ Charged Current interaction creating a muon track. (d) ν_τ Charged Current interaction creating a hadronic shower. (2)

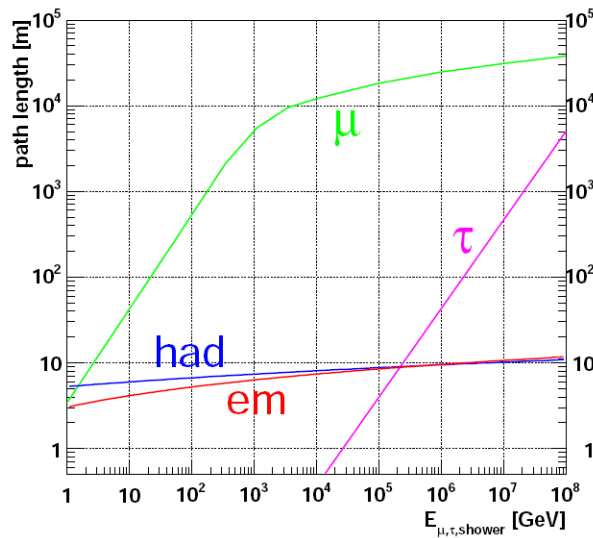


Figure 1.2: Path lengths of muons, taus, and electromagnetic and hadronic showers in water (3).

The emerging lepton inherits the flavor of the incident neutrino. ν_e will thus pro-

1. HIGH-ENERGY NEUTRINO DETECTION

duce an electron which then creates an electromagnetic shower to overlap with the hadronic shower. ν_μ will generate a muon track and a hadronic shower and is considered to be the “golden channel” for neutrino astronomy and Figure 1.2 shows why: the long muon range at $E_\mu > 1$ TeV makes it possible to detect the muons produced far outside the instrumented detector volume and supplies great assistance for direction reconstruction. Finally, ν_τ will produce a τ lepton which will travel a certain distance before decaying into, among other possibilities, another hadronic shower. This type of event with two hadronic showers is often called a “double bang” event. There are two main types of τ decays which will directly lead to either a muon or an electron through another CC interaction

$$\tau^+ \rightarrow \mu^+ + \nu_\mu + \bar{\nu}_\tau, \quad \tau^- \rightarrow \mu^- + \bar{\nu}_\mu + \nu_\tau \quad (\text{B.R.} = 17.41\%) \quad (1.3)$$

$$\tau^+ \rightarrow e^+ + \nu_e + \bar{\nu}_\tau, \quad \tau^- \rightarrow e^- + \bar{\nu}_e + \nu_\tau \quad (\text{B.R.} = 17.83\%) \quad (1.4)$$

In Figure 1.3, the neutrino and antineutrino CC cross sections are shown: the upper panels display measurements performed at lower energies, from 50 MeV to 500 GeV; whereas the lower panel present some more recent results obtained by the IceCube collaboration for neutrino energy between 6.3 TeV and 980 TeV (5). The cross sections for neutrino energies lower than 500 GeV were collected over many decades using a variety of neutrino targets and detector technologies (4). The contributing processes are the Quasi-Elastic scattering (QE), the RESonance production (RES) and the Deep Inelastic Scattering (DIS). Below about 5-10 TeV the cross section, for both neutrino and antineutrino, increases roughly proportionally to the neutrino energy as shown in Figure 1.4.

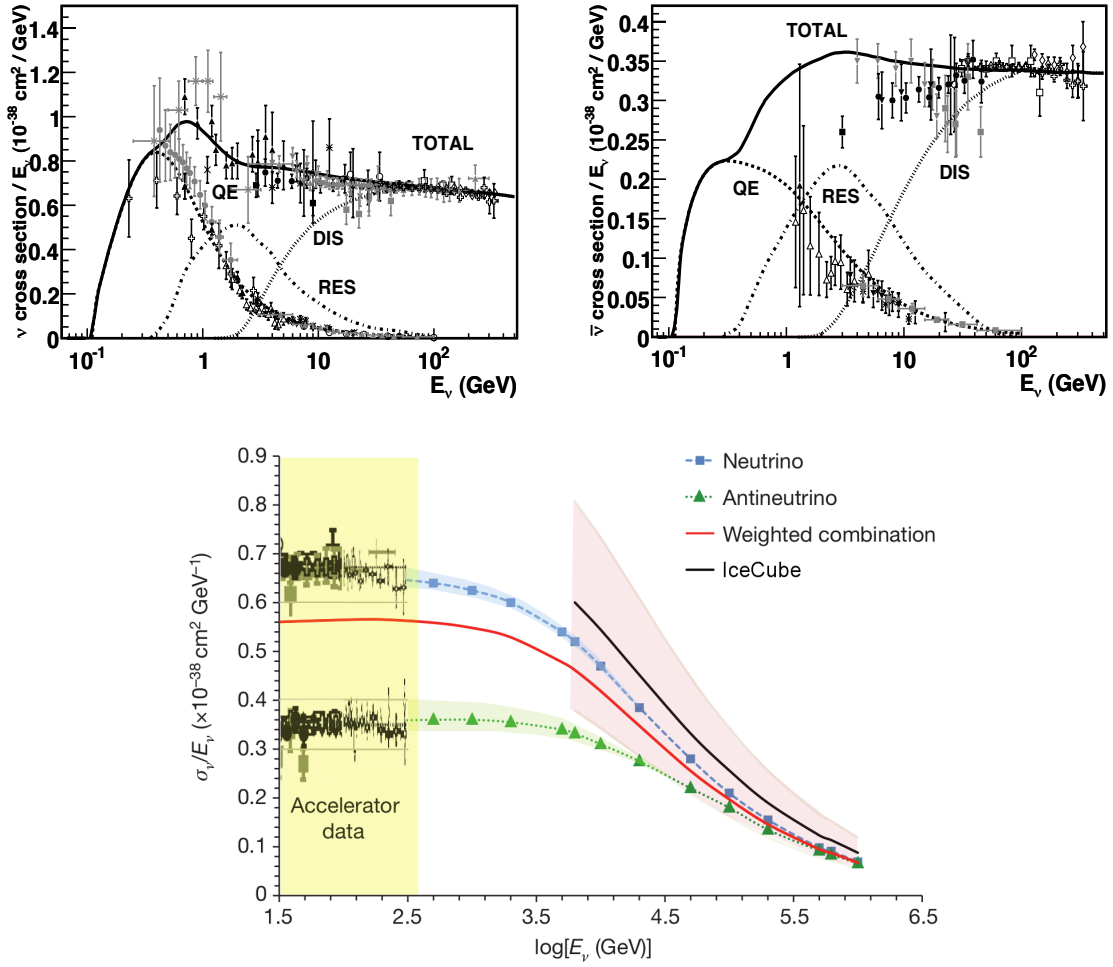


Figure 1.3: Upper panel: Total neutrino (left) and antineutrino (right) per nucleon CC cross sections divided by neutrino energy and plotted as a function of energy (4). Lower panel: Measured neutrino CC interaction cross-sections, divided by the neutrino energy (5). The blue and green lines are the standard model predictions for ν_μ and $\bar{\nu}_\mu$, respectively, with the uncertainties on the DIS cross-sections shown by the shaded bands. The red line corresponds to the expected mixture of ν_μ and $\bar{\nu}_\mu$ in the IceCube sample. The black line shows the IceCube result and the pink band shows the total 1σ (statistical plus systematic) uncertainty.

1. HIGH-ENERGY NEUTRINO DETECTION

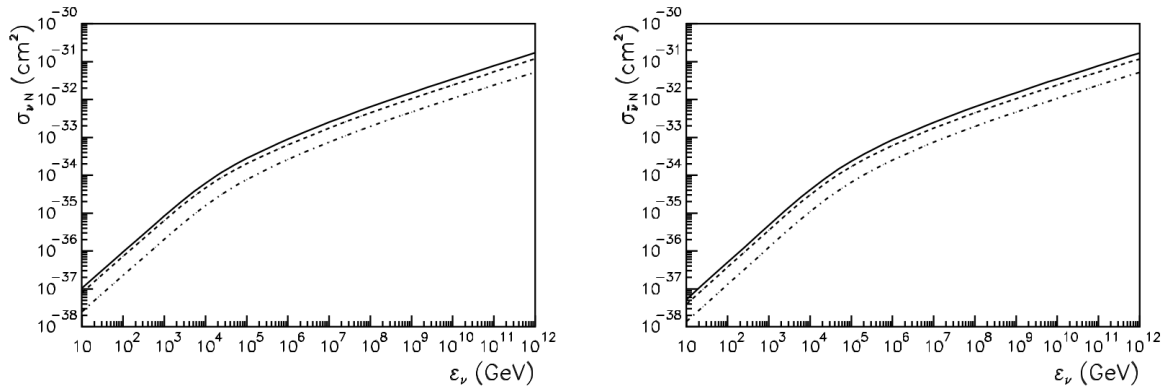


Figure 1.4: Cross sections for νN (left) and $\bar{\nu} N$ (right) interactions at high energies. The CC (dashed line), NC (point-dashed lines) and total (solid lines) cross sections are indicated (6).

For higher energies, the cross section for νN DIS interactions is written in terms of the Bjorken scaling variables $x = Q^2/2M\nu$ and $y = \nu/E_\nu$ (6)

$$\frac{d^2\sigma}{dx dy} = \frac{2G_F^2 M E_\nu}{\pi} \left(\frac{M_W^2}{Q^2 + M_W^2} \right)^2 [xq(x, Q^2) + x\bar{q}(x, Q^2)(1-y)^2] \quad (1.5)$$

where $-Q^2$ is the invariant momentum transfer between the incident neutrino and outgoing lepton, $\nu = E_\nu - E_l$ is the energy loss in the target frame, M and M_W are the nucleon and intermediate-boson masses, $q(x, Q^2)$ and $\bar{q}(x, Q^2)$ are the quark and anti-quark distribution functions, and G_F is the Fermi constant.

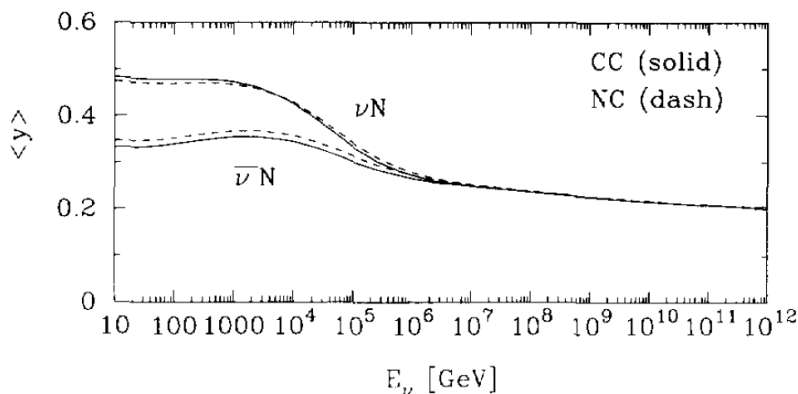


Figure 1.5: Energy dependence of the inelastic parameter y for CC (solid lines) and NC (dashed lines) interactions as a function of the incident neutrino energy (6).

The inelasticity y is another important parameter to characterize the interaction. It describes the fraction of the initial neutrino energy taken by the hadronic shower $E_l =$

$(1 - y)E_\nu$. As can be seen in Figure 1.5, the behaviour of neutrino and antineutrino differs below 10^6 GeV. Around 10 GeV the percentage of energy transferred to the shower is about 50% in case of νN interaction and 35% for $\bar{\nu} N$. Whereas above 10^6 GeV, y is about 0.2 for both neutrinos and antineutrinos.

From 10^{10} GeV to 10^{15} GeV the total cross-sections are given within 10% by (7)

$$\sigma_{CC}^{\nu N} = 5.53 \times 10^{-36} \left(\frac{E_\nu}{1\text{GeV}} \right)^{0.363} \text{ cm}^2 \quad (1.6)$$

$$\sigma_{NC}^{\nu N} = 2.31 \times 10^{-36s} \left(\frac{E_\nu}{1\text{GeV}} \right)^{0.363} \text{ cm}^2 \quad (1.7)$$

$$\sigma_{CC}^{\bar{\nu} N} = 5.52 \times 10^{-36} \left(\frac{E_\nu}{1\text{GeV}} \right)^{0.363} \text{ cm}^2 \quad (1.8)$$

$$\sigma_{NC}^{\bar{\nu} N} = 2.29 \times 10^{-36} \left(\frac{E_\nu}{1\text{GeV}} \right)^{0.363} \text{ cm}^2 \quad (1.9)$$

The neutrino interaction length is defined as

$$L_{int}(E_\nu) = \frac{1}{\sigma_{\nu N}(E_\nu) \langle \rho \rangle} \quad (1.10)$$

where $\langle \rho \rangle$ is the average crossed medium density. An increase of the νN and $\bar{\nu} N$ cross section, with increasing E_ν , will thus lead to a decrease of the neutrino interaction length as indicated in Figure 1.6. Consequently, for energies above about 40 TeV, the interaction length gets shorter than the Earth's diameter (12742 km), meaning that a significant part of the incident neutrinos at higher energies in getting absorbed in the Earth.

1. HIGH-ENERGY NEUTRINO DETECTION

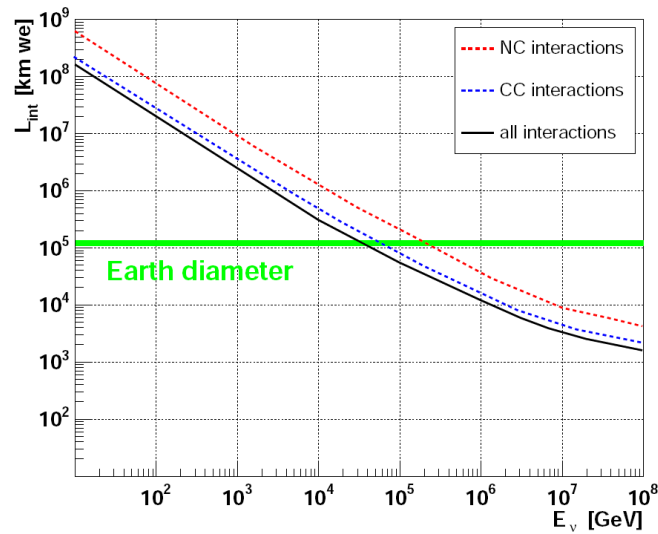


Figure 1.6: Interaction lengths, given in km water equivalent, as a function of the neutrino energy for different types of νN interactions. (2)

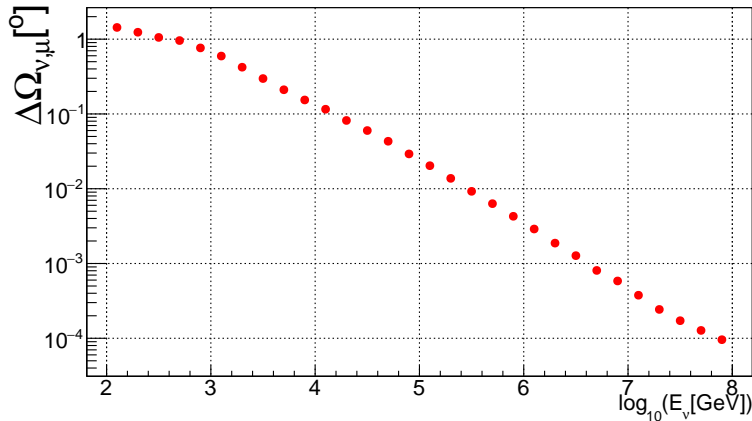


Figure 1.7: Median of the angle between the neutrino and the produced muon directions for each neutrino energy bin.

As seen in Figure 1.3, at the energies of interest (above 100 GeV), the DIS is the dominant process. The kinematics of this interaction is such that the angle between the directions of the neutrino and the produced muon decreases with energy, as shown in Figure 1.7. As only the muon direction can be reconstructed, this imposes a limit on the neutrino telescope's achievable angular resolution. In fact, the latter is determined by the muon track reconstruction above energies of a few TeV. The original neutrino direction can thus be inferred from the measured muon direction

as the uncertainty introduced by the scattering angle is negligible compared to the detector's angular resolution.

1.1.2 Muon Propagation

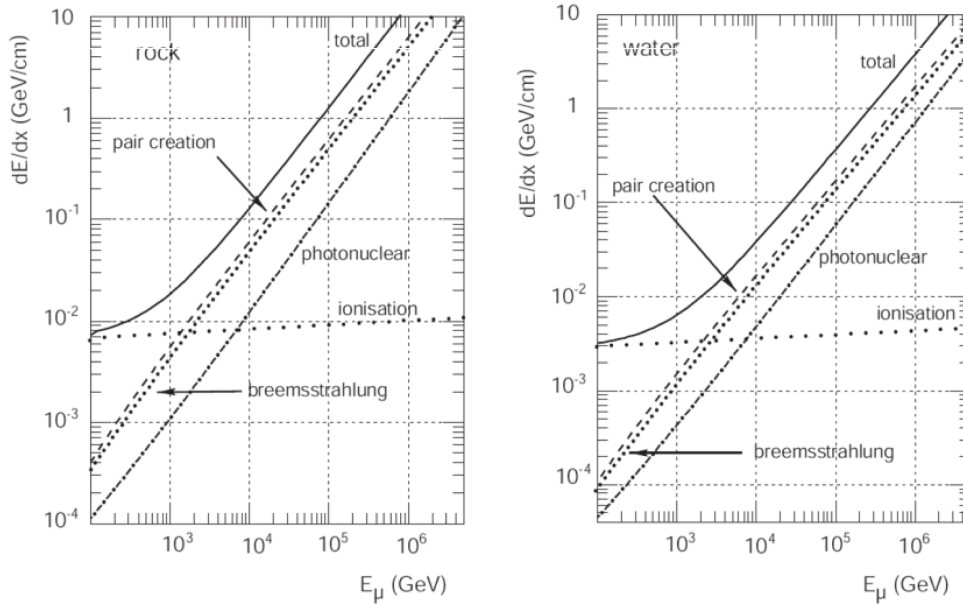


Figure 1.8: Partial and total muon energy losses in rock (left) and water (right) as a function of the muons energy. (8)

When a high energy muon propagates in a transparent medium, such as water or ice, it loses a small amount of energy through the emission of Cherenkov radiation. Although this process is of more interest for high-energy neutrino detectors, the majority of the muon energy loss is due to several other mechanisms, as can be seen in Figure 1.8:

1. *ionization of matter* is the dominant process at energies below 1 TeV. The muon causes atomic excitations and ionization of matter during its travel.
2. *e^+e^- pair production* is the dominant process at energies above 1 TeV. Spontaneous radiation emitted by the muon will produce an e^+e^- pair;
3. *bremsstrahlung*. The muon decelerates through the emission of radiation but this time resulting from electromagnetic interactions with nuclei and electrons of surrounding atoms;

1. HIGH-ENERGY NEUTRINO DETECTION

4. *photo-nuclear interactions.* The muons exchanges a virtual photon with a nucleus of the surrounding medium.

For muons with energy above 1 TeV the average rate of energy loss can be expressed according to

$$-\frac{dE}{dx} = a(E) + b(E)E \quad (1.11)$$

As muon energy increases to 10 TeV, ionization effects account for only 9% of the total muon energy loss, with a much reduced contribution as muon energy increases. At high energies, at first approximation, the ionization term a and the radiative losses term b can be considered as energy independent. To the approximation that these slowly-varying functions are constant and using Equation 1.11, it's possible to compute the mean range R of a muon as

$$R = \frac{1}{b} \ln \left(1 + \frac{E_\mu b}{a} \right) \quad (1.12)$$

1.1.3 Cherenkov Radiation

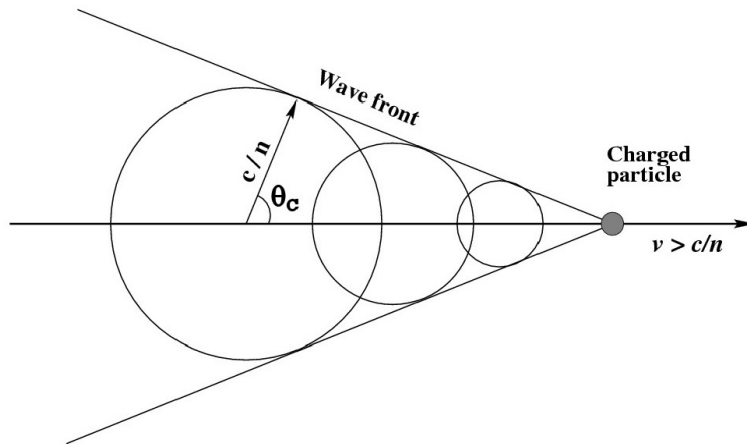


Figure 1.9: Schematic view of a longitudinal section of the Cherenkov light cone. (2)

One of the most significant identification methods for high-energy particles is based on the Cherenkov effect. When a charged particle with velocity v traverses a dispersive medium of refractive index n , excited atoms in the vicinity of the particle become polarized. If v is greater than the speed of light in the medium c/n , a part of the excitation energy reappears as coherent radiation emitted at a characteristic

angle θ_C with respect to the direction of the motion, as can be seen in Figure 1.9. The angle θ_C is linked to n and v by the Mach relation

$$\cos \theta_C = \frac{1}{\beta n} \quad (1.13)$$

with $\beta = v/c$. The number of Cherenkov photons N emitted by a particle of charge ze per unit wavelength interval $d\lambda$ and unit distance travelled dx is given by

$$\frac{d^2N}{dx d\lambda} = \frac{2\pi\alpha z^2}{\lambda^2} \left(1 - \frac{1}{\beta^2 n^2(\lambda)} \right) \quad (1.14)$$

where λ is the wavelength of the photon and α is the fine structure constant. The differential energy loss into Cherenkov photons in water or ice is a few percent of the total differential energy loss of a charged particle as it crosses the medium with a speed very close to c . In the wavelength range between 300 nm and 600 nm where water is transparent, this results in a number of about 3.4×10^4 Cherenkov photons emitted per meter travelled in seawater. With relatively so few photons produced per meter segment of muon track, both an exceptionally transparent medium and sensitive detector are required. In this relevant wavelength region, the refractive index of water is $n \sim 1.35$, assuming a highly relativistic particle with $\beta \sim 1$ will lead to a Cherenkov angle of $\theta_C \simeq 42.2^\circ$.

1.1.4 Light Transmission Properties

The attenuation of the Cherenkov light in water sets an upper limit to the distance between the telescope's optical sensors. In order to properly describe the transparency of seawater as a function of wavelength, it is necessary to measure the parameters describing absorption and scattering, such as the absorption length $\lambda_{abs}(\lambda)$, the scattering length $\lambda_s(\lambda)$ and the attenuation length $1/\lambda_{att}(\lambda) = 1/\lambda_{abs}(\lambda) + 1/\lambda_s(\lambda)$. Each of these lengths represents the path after which a beam of initial intensity I_0 and wavelength λ is reduced in intensity by a factor of $1/e$ through absorption and/or scattering according to

$$I_{abs,s,att}(x) = I_0 \exp\left(-\frac{x}{\lambda_{abs,s,att}}\right) \quad (1.15)$$

where x is the optical path traversed by the beam. In the literature, the coefficients of absorption $a = 1/\lambda_{abs}(\lambda)$, and scattering $b = 1/\lambda_s(\lambda)$, are used to characterise the

1. HIGH-ENERGY NEUTRINO DETECTION

light transmission through matter. The sum of scattering and absorption coefficients is called “attenuation coefficient” c .

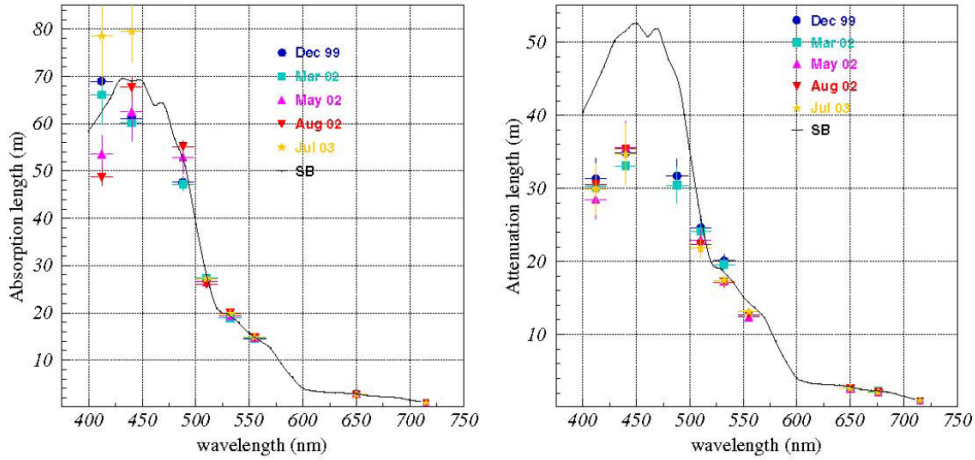


Figure 1.10: Absorption length (left) and attenuation length (right) measured at the Capo Passero site at four seasons. The black line indicates the values for optically clean salt water (9).

As shown in Figure 1.11, water is transparent only to a narrow range of wavelengths ($350 \text{ nm} \leq \lambda \leq 550 \text{ nm}$). In particular, λ_{abs} is about 100 m for deep polar ice and about 70 m for clear ocean waters (10). From these values one can get a preliminary rough estimate of the number of optical sensors that are needed to instrument a km^3 of water, which turns out to be about 5000.

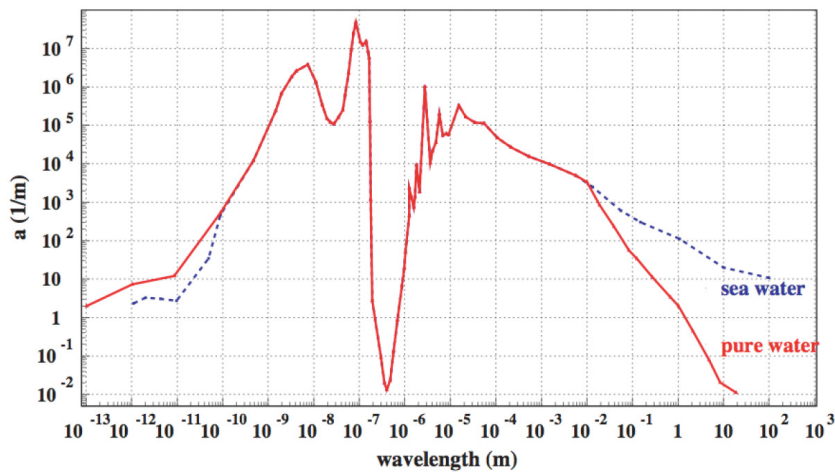


Figure 1.11: Light absorption coefficient a as a function of wavelength for pure water (red solid line) and seawater (blue dashed line) (10).

1.2 Background

1.2.1 Environmental Optical Background

The reconstruction of muon tracks depends quite strongly on time and spatial position information of the photon hits. To tackle optical natural backgrounds the neutrino telescope is located in the deep-sea environment. Although this helps to shield the detector from sunlight for example, there still exists two possible sources of light background: Cherenkov light produced in the propagation of charged particles originating in the decay of radioactive elements in the seawater and luminescence induced by biological organisms, the so called bioluminescence. While the ^{40}K decay is stable as a function of time and location in the detector, the bioluminescence activity can fluctuate significantly in time.

Bioluminescence

There are two contributions to bioluminescent light, one varying on time scales of hours to days (presumably from bacteria) and one coming in “bursts” with durations of a few tens of seconds (assigned to larger size organisms). The most direct assessment of bioluminescence and its impact on the neutrino telescope is by measuring the intensities of deep-sea background light over long-term periods. To investigate the occurrence of bioluminescent organisms, water samples have been retrieved from different depths at a location near the Capo Passero Site. Subsequently, the density of luminescent bacteria cultivatable at atmospheric pressure has been determined. The results in Figure 1.12 indicate that such bacteria are essentially absent at depths beyond 2500 m. A seasonal effect was found at the Capo Passero site where values were higher in the autumn than in spring between 500 m and 2400 m. No pronounced seasonal effect in the abundance of bioluminescent animals was found at the Pylos site. Nevertheless at these detectors’ depth the bioluminescence level is very low.

1. HIGH-ENERGY NEUTRINO DETECTION

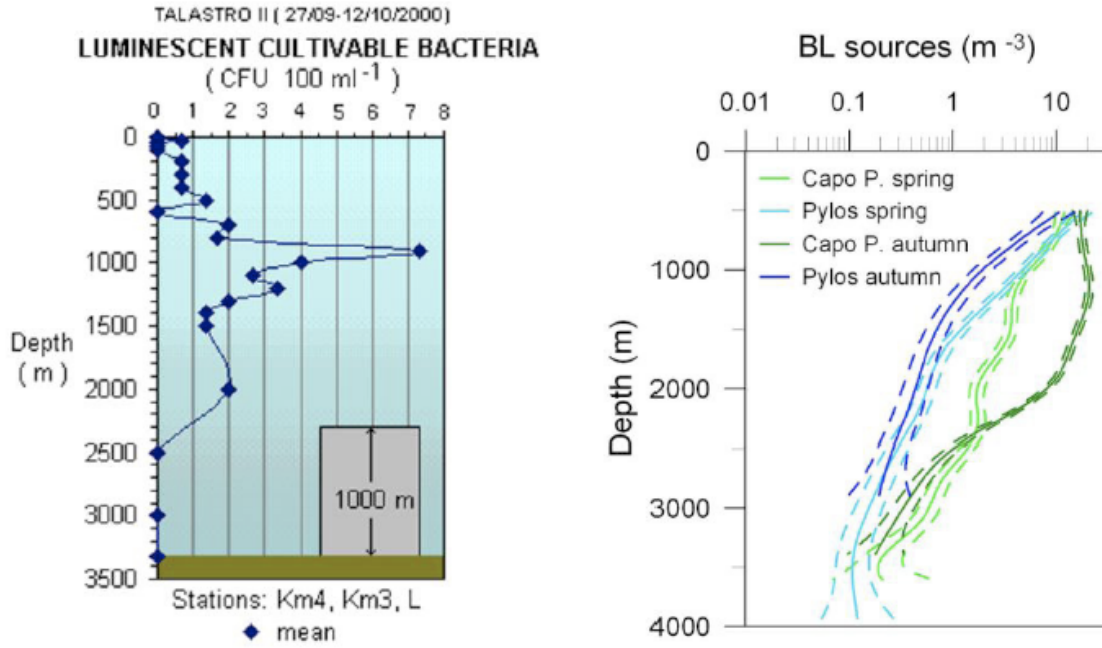
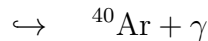
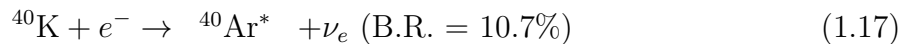


Figure 1.12: Left panel: Concentration of luminescent bacteria cultivable at atmospheric pressure as a function of depth. The data have been obtained from water samples taken at the Capo Passero site. Right panel: Density of bioluminescent animals at the Capo Passero and Pylos sites, in autumn 2008 and spring 2009 (dashed lines show 95%CL).

Radioactivity

Several radioactive elements can be found in seawater, the most abundant is ^{40}K , which has two main decay channels:



The first process yields an electron with an energy up to 1.3 MeV. This energy exceeds the Cherenkov threshold for electrons in sea water (0.25 MeV), and is sufficient to produce up to 150 Cherenkov photons. Another source of electrons above the Cherenkov threshold is the Compton scattering of 1.46 MeV photons, which are produced in the process of electron capture. Light pulses due to ^{40}K decays are uncorrelated on time scales of a few nanoseconds. However radioactive decays may

produce many photons within 1 ns, giving raise to narrow coincidences on neighboring PMTs.

In Figure 1.13, the baseline rates of various Optical Modules (OMs) of the NEMO Phase-2 tower in Capo Passero are recorded throughout the whole operation period (11). The upper panel displays the rates recorded by the four OMs of the first floor and the lower panel shows the rates recorded by one of the down-looking OMs for each floor of the tower. The rates have values of about 50-60 kHz, corresponding to the expected contribution of ^{40}K decays in water. The sporadic peaks above this baseline, but always below 100 kHz, can be attributed to periods with a higher level of bioluminescence activity. The ^{40}K component is typically steady and homogeneous over the full detector whereas bioluminescence bursts can cause rates that are much larger, but affect only a local group of OMs. Both components thus differ significantly in their impact on data taking, filtering and analysis. The upper panel of Figure 1.13 provides some insight for a comparison between OMs at the same depth but with different orientation, showing that also in this case the rates are similar. However, a slight decrease with time of the rates measured with the two horizontally looking OMs can be observed. The origin of this can reasonably be attributed to the deposit of a thin sediment layer on the uppermost part of the OM.

1. HIGH-ENERGY NEUTRINO DETECTION

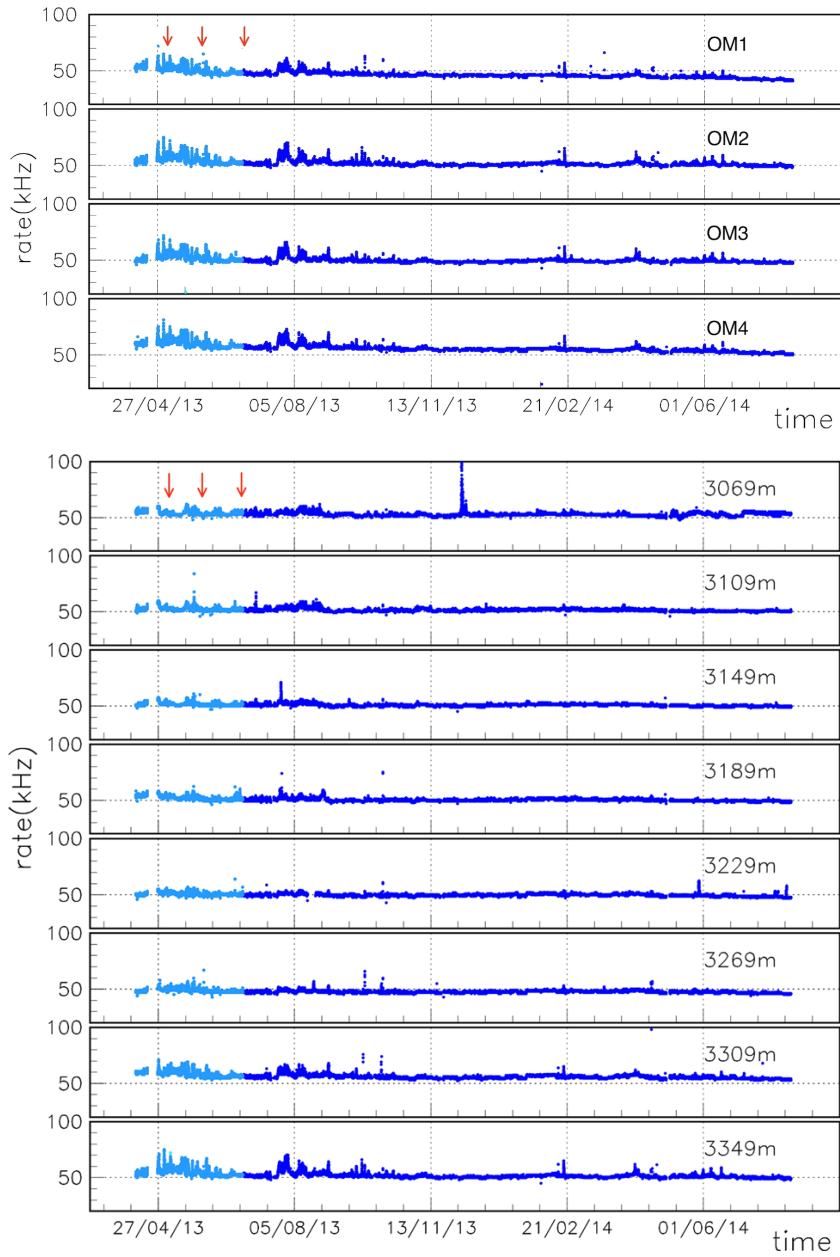


Figure 1.13: Baseline rate measured for the whole operation period of the NEMO tower in Capo Passero. The light blue dots correspond to the commissioning period of the detector and the arrows indicate the dates when PMT high voltage adjustments were performed (11). Upper: Measurement by the four OMs of the first floor. OM 1 and 4 are horizontally looking and OM 2 and 3 are downward looking. Lower: Measurements at different depths by down-looking PMTs.

1.2.2 Physical Background

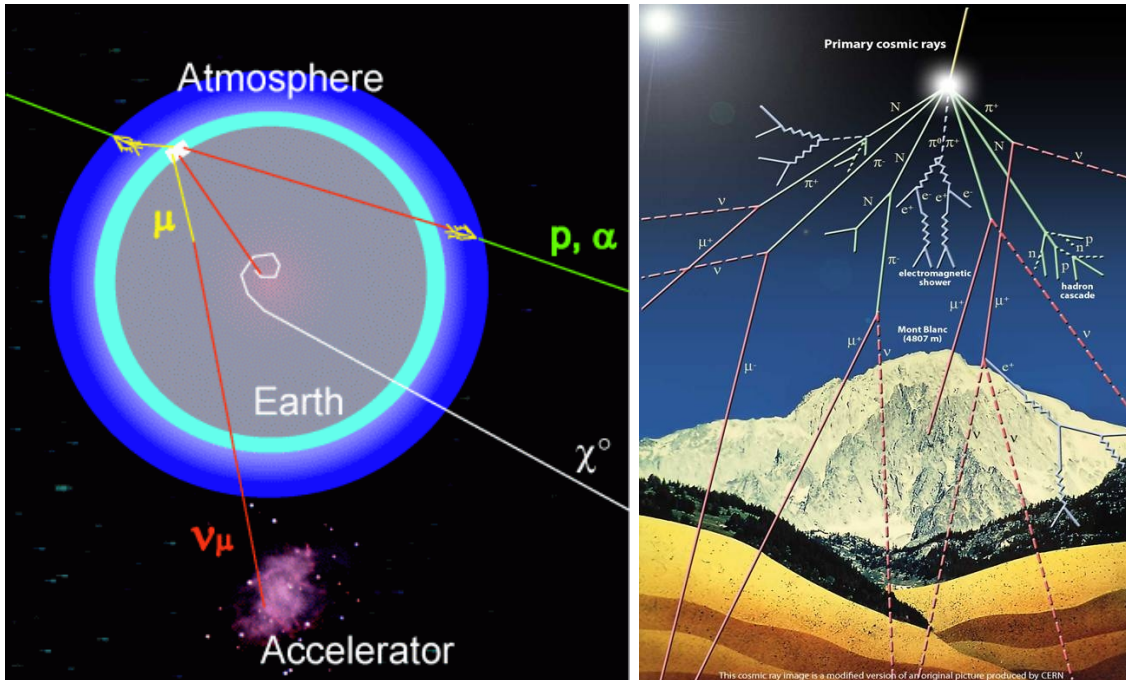


Figure 1.14: Left panel: Sketch showing the origin of atmospheric muons and neutrinos. Signal neutrinos (in red), either from cosmic accelerators or dark matter particles, transverse the Earth and emit a secondary particle that reaches the detector (in pink). Right panel: Illustration with more details about the interaction of primary cosmic rays with the atmosphere, producing both atmospheric muons and atmospheric neutrinos.

The cosmic neutrino sources, which will be discussed in Chapter 3, can produce a detectable neutrino-induced muon flux. However, only a fraction of the total muon flux that arrives at the detector is produced by astrophysical sources, the rest is background that must be rejected. There are two sources of background and both of them originate from the interaction of cosmic rays in the atmosphere, as seen in Figure 1.14. When a cosmic proton interacts with an atmospheric nucleus it gives rise to a hadron cascade composed of many particles including π^+ and π^- . The latter are unstable and produce muons and neutrinos when they decay. Consequently from primary cosmic rays' cascades are produced on one hand, atmospheric muons, and on the other hand, atmospheric neutrinos, which will later produce muons. The details of these mechanisms will be described in Chapter 3.

1. HIGH-ENERGY NEUTRINO DETECTION

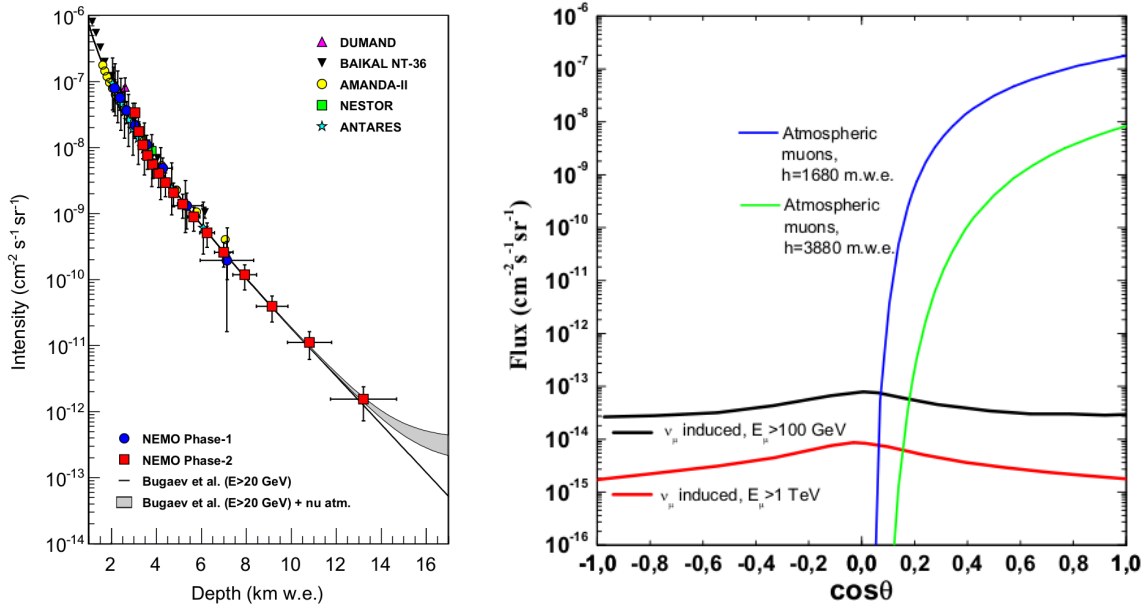


Figure 1.15: Left panel: Atmospheric muon intensity as a function of depth of water equivalents measured by various detectors, including NEMO Phase-1 and NEMO Phase-2 (12). Right panel: Different contributions, as a function of the cosine of the zenith angle, of the atmospheric muons for two different depths; and of the atmospheric neutrino induced muons, for two different muon energy thresholds.

The right panel of Figure 1.15 describes the muon flux induced by atmospheric neutrinos and the direct atmospheric muon flux as a function of the cosine of the zenith angle. For downward events, the atmospheric muon flux largely exceeds that of muons induced by atmospheric neutrinos by many orders of magnitude, although it is completely suppressed in the upgoing direction. This is explained by the fact that atmospheric muons, can cross the atmosphere and reach the Earth surface or the sea but will be absorbed after several kilometers (12), as noticed on the left panel of Figure 1.15. Therefore the expected muon background is solely constituted of downgoing particles, which can in principle be rejected by restricting the search for signal events exclusively to upgoing reconstructed events since upgoing muons can only be produced by interaction of upgoing neutrinos. Regrettably, misreconstructed downgoing events can mimic upgoing neutrino-induced muons, adding another thick layer of difficulty considering the few tens of events per year being looked for with the detector, and making it severely important to reduce the atmospheric muon flux by installing the detector at large depths and by improving the reconstruction technique.

An additional source of background comes from upgoing muons produced by at-

atmospheric neutrinos that have partially or fully crossed the Earth (Chapter 3.4). Atmospheric neutrinos are an irreducible background component, since they are indistinguishable from astrophysical neutrinos. However at high energies it is expected that the cosmic neutrino diffuse flux may dominate over the atmospheric neutrino background, due to their different energy spectral indices ($\gamma \sim 3.7$ for atmospheric ν and $\gamma \sim 2$ for cosmic ν).

1.3 Cherenkov Neutrino Telescopes

Without bringing up too many details, the telescopes that came before KM3NeT in the Mediterranean Sea will be introduced. Their research activities aimed at developing and validating key technologies for a km³-scale underwater neutrino telescope and characterizing deep-sea sites suitable for the installation of the KM3NeT telescope. The IceCube neutrino detector, whose results will be analyzed in Chapter 5, will also be described.

1.3.1 NESTOR and NEMO

The first initiative for a neutrino telescope in the Mediterranean Sea was the NESTOR (Neutrino Extended Submarine Telescope with Oceanographic Research) project which started in 1989. The site is located in the Ionian Sea close to Pylos in the Peloponnese. In 2003 the first floor structure was successfully deployed at a depth of about 4000 m, measuring 12 m in diameter and consisting of 12 OMS with 15-inch PMTs each.

1. HIGH-ENERGY NEUTRINO DETECTION

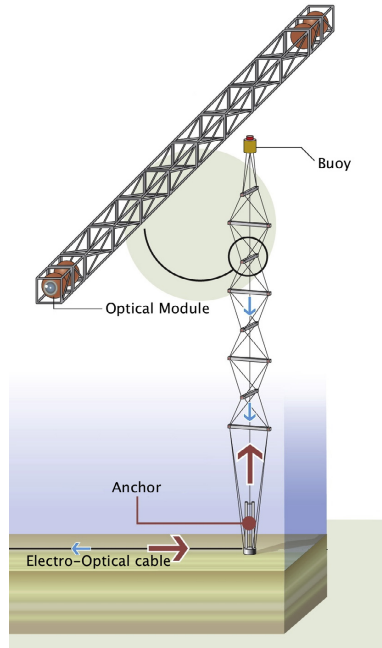


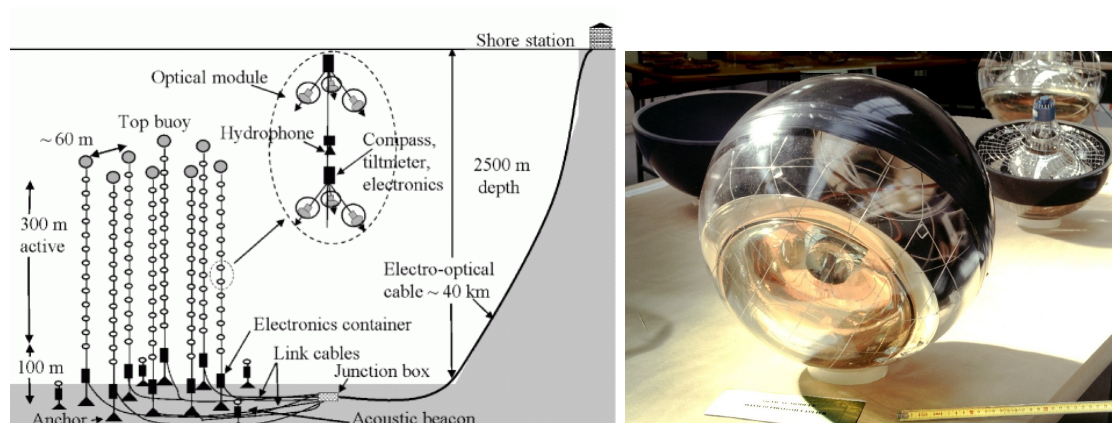
Figure 1.16: Sketch of the NEMO Phase-2 tower. Vertical distances are not to scale.
(11)

The NEMO (NEutrino Mediterranean Observatory) project was located in the Western Ionian Sea off Eastern Sicily (Italy). The collaboration started in 1998 and in 2007 the first pilot project was a tower-like detection unit (NEMO Phase-1 tower), which operated at about 2000 m depth for five months 20 km offshore Catania. In March 2013, a larger scale prototype (NEMO Phase-2 tower) was deployed offshore Capo Passero, in the south-east of Sicily, at an average depth of 3500 m (11). The underwater infrastructure is connected to the shore station located in Portopalo di Capo Passero via a 100 km electro-optical cable laid in 2008. The structure of the tower provides an unambiguous reconstruction of the muon direction even with a single detection unit. This detector operated continuously for more than one year until August 2014, when it was disconnected for an upgrade of the infrastructure in preparation for the installation of the Italian node of the KM3NeT detector.

The 380 m high tower is a three-dimensional semi-rigid structure composed of eight horizontal floors in marine grade aluminum. It is anchored to the seabed and kept vertical by an appropriate buoyancy on the top. The tower floor, a 8 m long structure, is connected to the next ones with four tensioning ropes such that each floor is perpendicular to its vertical neighbors. The floors are vertically spaced by 40 m, with the lowermost one located 100 m above the sea bottom. Each floor holds four OMs

(13), two at each end, one looking vertically downwards and the other horizontally outwards. An OM is composed by a PhotoMultiplier Tube (PMT) enclosed in a 13-inch pressure resistant glass sphere. The PMT is a 10-inch Hamamatsu R7081-SEL with 10 dynode stages. Mechanical and optical contact between the PMT and the internal glass surface is ensured by an optical silicon gel. A μ -metal cage shields the PMT from the Earth magnetic field. The tower is also equipped with hydrophones and compasses for positioning (14), and with Conductivity, Temperature, Depth (CTD) sensors and current speed meter for environmental monitoring. Each OM also contains a high-voltage supply circuit, read-out electronics and an optical system for timing calibration.

1.3.2 ANTARES



(a) Schematic view of the ANTARES detector layout. (b) ANTARES Optical Module.

The Astronomy with a Neutrino Telescope and Abyss environmental RESearch (ANTARES) project is located in the Mediterranean Sea, about 40 km of the French town of Toulon at a depth of 2475 meters. The full detector was completed in May 2008 and has been operating continuously. The telescope consists of twelve detection lines with 25 storeys each, except for one line which holds only 20 storeys because acoustic devices are installed. A standard story includes three OMs each housing a 10-inch Hamamatsu PMT, a special gel for optical coupling, a μ -metal cage for magnetic shielding and a local control module containing the electronics. Each PMT has a sensitive area of 440 cm² and a maximal Quantum Efficiency (QE) around 25%. There is a total of 885 active OMs oriented 45° downwards in order to optimize their

1. HIGH-ENERGY NEUTRINO DETECTION

acceptance to upgoing light and to reduce the effect of sedimentation and biofouling. The horizontal distance between neighboring lines ranges from 60 to 75 meters, reaching an instrumented volume of about 0.025 cubic kilometers. Each line has a length of 450 m and is kept taut by a buoy located at its top. On each line, the distance between each storey is 14.5 m and the lower 100 meters are not instrumented. The lines are connected to a central junction box, which in turn is connected to a shore station via an electro-optical cable. The ANTARES neutrino telescope is optimized to detect neutrinos with energies above 100 GeV. The detector started taking data in January 2007, when it was composed of only five detection lines. It was upgraded to ten detection lines in December 2007 and was completed in May 2008 with its twelve line configuration. Although ANTARES is currently the largest neutrino detector viewing the Galactic Center, an efficient search for high-energy neutrinos (above 10 TeV) originating from galactic and extra-galactic sources requires a much larger deep sea neutrino telescope (KM3NeT).

1.3.3 ICECUBE

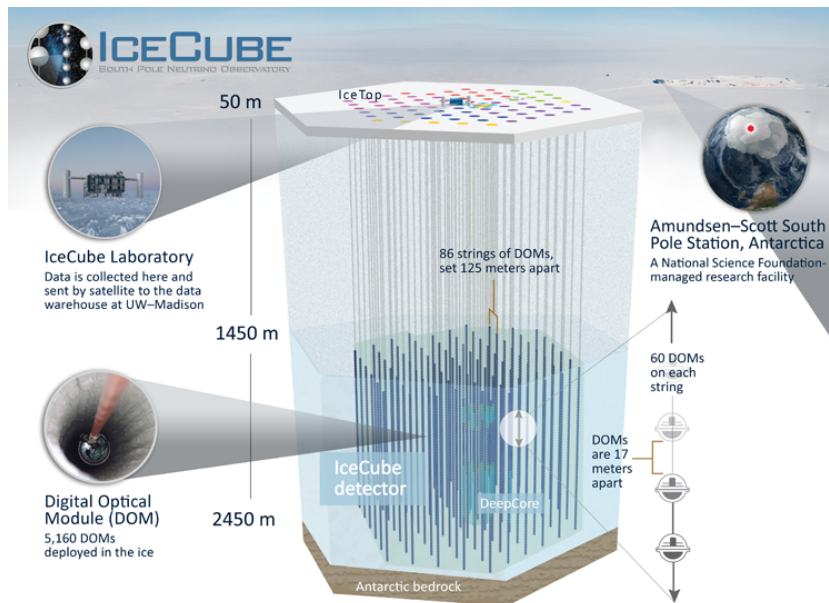


Figure 1.18: Schematic view of the IceCube detector layout. (15)

On the other hemisphere, IceCube (15) is the first built km^3 neutrino observatory, located near the Amundsen-Scott South Pole Station. Its predecessor, AMANDA (Antartic Muon And Neutrino Detector Array) was completed in 2001. It served

as a test bench for technologies and as a prototype for IceCube, whose construction began during the 2005-2006 Austral summer and was completed in December 2010. Although IceCube has been operational since the installation of its first string, it was only when it reached its 79-string configuration, whose construction phase lasted from May 2010 to May 2011 and represented approximately 90% of the full detector, that IceCube obtained its status of a km³-scale detector. The in-ice component of IceCube consists of 5160 DOMs installed at depths between 1450 and 2450 meters in the Antarctic ice. Each DOM contains a 10-inch PMT and associated electronics. Their peak QE is approximately 25% and they are operated at a gain of 10^7 . There are 80 vertical strings each containing 60 PMTs (plus 6 strings for Deep Core) and with a vertical separation of 17 m between each DOM. They have been installed, using hot drills, on a hexagonal grid with 125 m spacing. The full detector (IC-86) has been operational since May 2011. Six strings at the center of the array were deployed more compactly, with a horizontal separation of about 70 m and a vertical DOM spacing of 7 m. This denser configuration lowers the neutrino energy threshold to some tens of GeV, making it possible for IceCube to observe neutrino oscillations from atmospheric cosmic ray showers, over a baseline across the Earth. On the other hand, IceTop consists of 81 stations located on the surface of the glacier, on top of the same number of IceCube strings. Each station has two tanks equipped with two downward facing DOMs. IceTop detects air showers from primary cosmic rays in the 300 TeV to 1 EeV energy range and serves as a veto and calibration detector for IceCube. This surface array measures the cosmic-ray arrival directions in the Southern Hemisphere as well as the flux and composition of cosmic rays.

1. HIGH-ENERGY NEUTRINO DETECTION

Chapter 2

THE KM3NET DETECTOR

KM3NeT (16) is a large research infrastructure that will host two deep-sea neutrino detectors in the Mediterranean Sea, which is a convenient location to observe high-energy neutrino sources in the inner part of the Galaxy. The primary goal of the KM3NeT project is not only the detection of high-energy neutrino sources in the Universe but also the determination of the neutrino mass hierarchy. These objectives are strongly motivated by two recent important discoveries, namely the high-energy astrophysical neutrino signal reported by IceCube and the electron neutrinos contribution to the third neutrino mass eigenstate. In order to reach these objectives, two separate components were established: the Astroparticle Research with Cosmics in the Abyss (ARCA) component whose main scientific objective is the detection of high-energy neutrinos (above 1 TeV) of astrophysical origin, which includes finding neutrinos from the cosmic ray accelerators in our Galaxy; and the Oscillation Research with Cosmics in the Abyss (ORCA) component whose main goal is to study the fundamental properties of neutrinos (such as the neutrino mass hierarchy and some of the neutrino oscillation parameters) by exploiting the abundant fluxes of neutrinos produced in the interactions of cosmic rays with the Earth's atmosphere. The KM3NeT technology aims to instrument, at minimal cost and maximal reliability, the largest possible volume of seawater with a three dimensional spatial grid of ultra-sensitive photo-sensors, while remaining sensitive to neutrino interactions in the target energy range. All components are designed for at least ten years of operation with negligible loss of efficiency. The system should provide nanosecond precision on the arrival time of single photons, while the position and orientation of the photo-sensors must be known to a few centimeters and few degrees respectively,

2. THE KM3NET DETECTOR

in order to optimize the reconstruction of the muon trajectory and infer the arrival direction of the incident neutrino.

The whole project is organized in a single collaboration with a central management and common data analysis and repository centers. Following the acquisition of substantial funds, the first phase of KM3NeT was launched early 2013. Three deep-sea sites were selected for the optical properties of the water, distance to shore and local infrastructure. Structures are already being installed 40 km offshore Toulon (France) at a depth of 2500 m and 80 km offshore Capo Passero (Sicily, Italy) at a depth of 3500 m; constructions will later be extended 20 km offshore Pylos (Peloponnese, Greece) at depths between 3000 m and 4550 m. The ultimate goal is to fully develop the KM3NeT Research Infrastructure to comprise a distributed installation at the three foreseen sites and operate it for ten years or more. The Collaboration aspires to establish a European Research Infrastructure Consortium (ERIC) hosted in the Netherlands. The list of design features of the KM3NeT neutrino telescope includes a Digital Optical Module (DOM) with 31 3-inch PMTs, an integrated data-transmission and clock system, and a high-efficiency power network. All data are sent from the deep sea to the shore where they are processed in real-time by a farm of commodity PCs. The filtered data are sent to various computer centers around Europe for offline analyses. The remote operation of the deep-sea facility and the fast access to these computer centers make it possible to take and analyse data from anywhere in the world.

The angular resolution, the geographical location and the size of the telescope make KM3NeT an ideal instrument to observe upward-going neutrinos from about 3.5π sr of the sky, in particular the Galactic Center (GC) and most of the Galactic plane, where HESS discovered many TeV-gamma sources that are very promising neutrino candidate sources. Several astrophysical sources are expected to produce high-energy neutrinos spanning several orders of magnitude in energy. The KM3NeT detector design has been optimized in the energy range between 1 TeV and 1 PeV for the detection of point-like sources with a power law neutrino energy spectrum close to 2. As a prime example, neutrinos from Supernova remnants may produce a significant signal (5 sigma) within a reasonable amount of time (3-5 years). Furthermore, a study was launched to find out whether a measurement of the mass hierarchy of neutrinos using the same technology but a different detector layout is feasible. The

KM3NeT infrastructure will also host a network of cabled observatories with a wide array of dedicated instruments for oceanographic, geophysical and marine biological research.

2.1 The Installation Sites

The Mediterranean Sea offers optimal conditions, on a worldwide scale, to host an underwater neutrino telescope. Careful studies of candidate sites have been carried out, identifying several suitable sites for an undersea neutrino telescope. The most relevant criteria that lead to the choice of these sites are:

- Closeness to the coast to ease deployment and reduce the expense of the power and signal cable connections to shore;
- A sufficient depth to reduce background from atmospheric muons, and to suppress their misreconstruction as upgoing;
- Good optical properties of the water, i.e. absorption and scattering lengths close to the ones of optically pure sea water for light in the wavelength range of 350 nm to 550 nm;
- Low level of bioluminescence;
- Low rates of biofouling (bacterial film deposition and marine life accretion) on optical surfaces;
- Low rates of sedimentation;
- Stable low sea current velocities.

A long term characterization of the sites has been performed by studying a large number of oceanographical properties, like deep-sea water optical properties (absorption and diffusion), water environmental properties (temperature, salinity), biological activity (see Chapter 1.2.1), optical background, water currents, sedimentation and seabed nature. For instance, the light transmission at the Capo Passero site has been investigated. Indeed the absorption and attenuation coefficients have been measured at nine wavelengths ranging from 410 nm to 715 nm for four different seasons (9),

2. THE KM3NET DETECTOR

as shown previously in Figure 1.10. Comparing these results at deep waters with optically pure seawater show a close compatibility and no seasonal dependence of the optical parameters.

The KM3NeT-Italy infrastructure is located at $36^{\circ} 16' N$ $16^{\circ} 06' E$ at a depth of 3500 m, about 100 km offshore from Porto Palo di Capo Passero, Sicily, Italy (Figure 2.1). The site is the former NEMO site and is shared with the EMSO facility for Earth and Sea science research. This KM3NeT-Italy infrastructure will be devoted to ARCA research, which calls for large spacing between photo-sensors to target astrophysical neutrinos at TeV energies and above. In December 2008, the first Main Electro-Optic Cable (MEOC) was deployed. A new Cable Termination Frame (CTF) with five output ports and two secondary Junction Boxes (JBs) were successfully connected in July 2015.

The KM3NeT-France infrastructure is located at $42^{\circ} 48' N$ $6^{\circ} 02' E$ at a depth of 2475 m, about 40 km offshore from Toulon, France (see Fig. 6, left). The site is outside of the French territorial waters and about 10 km west of the site of the existing ANTARES telescope. The KM3NeT-France infrastructure will carry out ORCA research, requiring a denser photo-sensor configuration to target atmospheric neutrinos in the few-GeV range. For both previous sites, the power/data will be transferred to/from the infrastructure via two MEOCs comprising 36 to 48 optical fibers.

The KM3NeT-Greece site is located in the open sea off the southeastern tip of the Peloponnese in the vicinity of the town of Pylos and there are several locations under investigation. One of the extremely desirable features of this region of the Mediterranean Sea is the existence of those four sizeable plateaus that can accommodate a neutrino telescope at depths ranging from 3000 m to 4550 m. The most shallow site, at 13 km from the nearest landfall and 3000 m depth, allows for convenient deployment and can be used for tests; while the deepest site, at 26 km distance from Sapientza ($36^{\circ} 33' N$ $21^{\circ} 30' E$) and at a depth of 4550 m, allows for the deployment of a detector with reduced background from the downgoing muons from cosmic rays and higher sensitivity to very high energy neutrinos. A shore station is available which requires new facilities for power and computing.

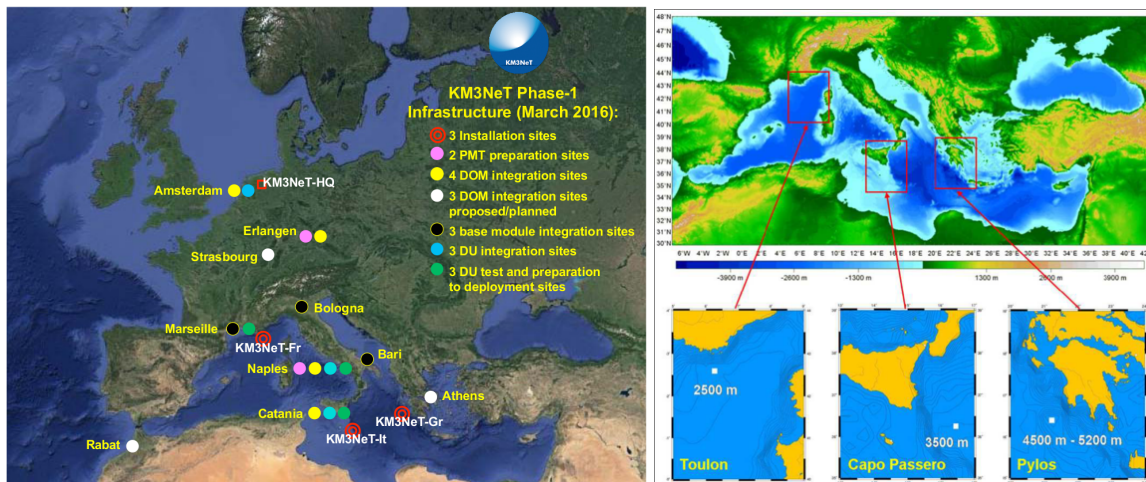


Figure 2.1: Left panel: Map of the various preparation, integration and installation sites of KM3NeT Phase-1 up to March 2016. (17) Right panel: The location of KM3NeT’s three installation sites.

Furthermore, from the detector’s location in the Mediterranean Sea, 87% of the sky will be mapped including most of the Galaxy and the Galactic Center, where some interesting unexplained phenomena are observed with other astroparticle detectors.

2.2 Building Blocks and Detection Units

Each detection string with its 18 DOMs are referred to as Detection Units (DU). For KM3NeT/ARCA, each DU is about 700 m in height, with DOMs spaced 36 m apart in the vertical direction, starting about 80 m from the sea floor. For KM3NeT/ORCA, each DU is 200 m in height with DOMs spaced 9 m apart in the vertical direction, starting about 40 m from the sea floor. Each string comprises two thin (4 mm diameter) parallel dyneema ropes to which the DOMs are attached via a titanium collar. Additional spacers are added in between the DOMs to maintain the ropes parallel. Attached to the ropes is the vertical electro-optical cable, a pressure balanced, oil-filled, plastic tube that contains two copper wires for the power transmission and 18 optical fibers for the data transmission to shore. At each storey two power conductors and a single fiber enter the glass sphere via a penetrator and are branched out via the breakout box. Even though the string design minimises drag and itself is buoyant, additional buoyancy is introduced at the top of the string

2. THE KM3NET DETECTOR

to reduce the horizontal displacement of the top relative to the base for the case of large sea currents.

For deployment and storage, the string is coiled around a large spherical 2 m wide frame, the so-called launcher vehicle, in which the DOMs slot into dedicated cavities (see Figure 2.2). The launcher vehicle is lowered to the seabed from a surface vessel. Once the launcher vehicle has reached the seabed, the buoy is released, the string unfurls and rises to its full height. The launcher vehicle is then recovered for subsequent deployments. The anchor at the bottom of the DU is the interface with the seabed infrastructure. It is external to the launcher vehicle and is sufficiently heavy to keep the string fixed on the seabed. The anchor houses an interlink cable, equipped with a wet-mateable connectors, and the base container. The base container incorporates dedicated optical components and an acoustic receiver used for positioning of the detector elements.

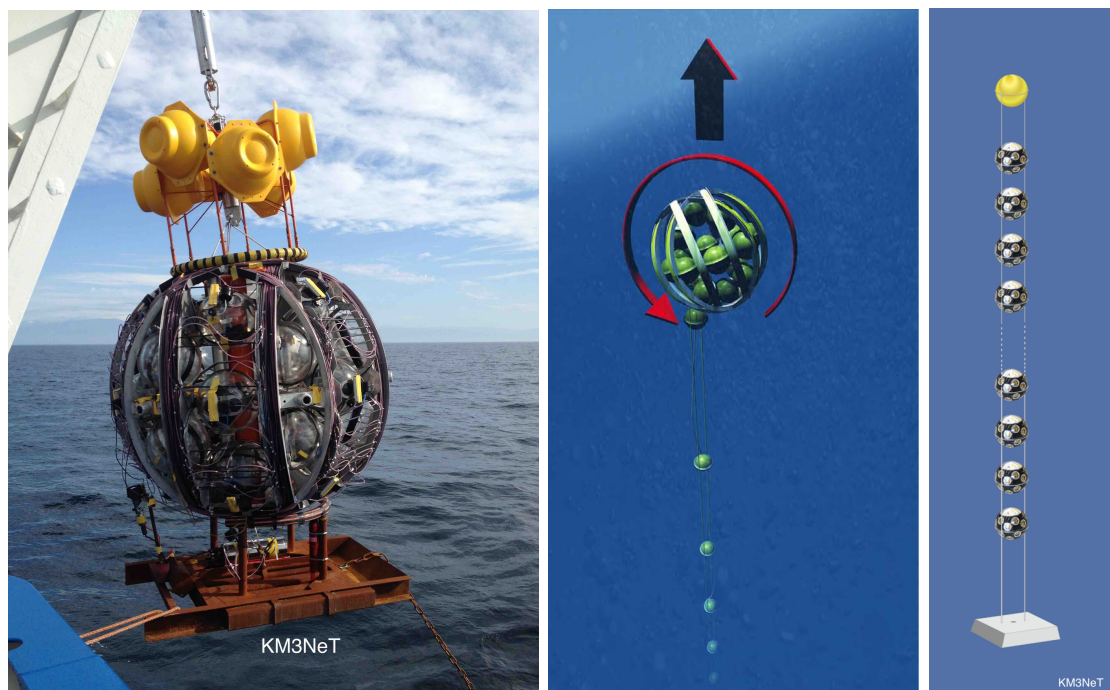


Figure 2.2: Left panel: Launch vehicle deployment. Center panel: Principle of the launch vehicle unfurling. Right panel: Detection string. (16, 17)

A prototype DOM (Pre Production Model DOM, PPM-DOM) was successfully attached to one ANTARES line in April 2013 in order to validate the DOM concept and technology (Figure 2.2, left). Afterward, in May 2014, a prototype Detection Unit (Pre Production Model DU, PPM-DU) with three DOMs was installed at the

2.2 Building Blocks and Detection Units

Capo Passero site and operated in situ for over a year (Figure 2.2, right). This prototype, unlike the PPM-DOM, implements the mechanical structure, the electro-optical connections and the data transmission system developed for the final DU design. Through the study of correlated signals in different DOMs generated from LED nanobeacons and from atmospheric muons, a synchronisation at a nanosecond level between DOMs was obtained. In December 2015, a first full-size production string of 18 DOMs was successfully installed at the KM3NeT-Italy site. In May 2016, two more strings were deployed but one was then recovered for inspection in July 2016. Both the PPM-DOM and the PPM-DU are displayed in Figure 2.3.

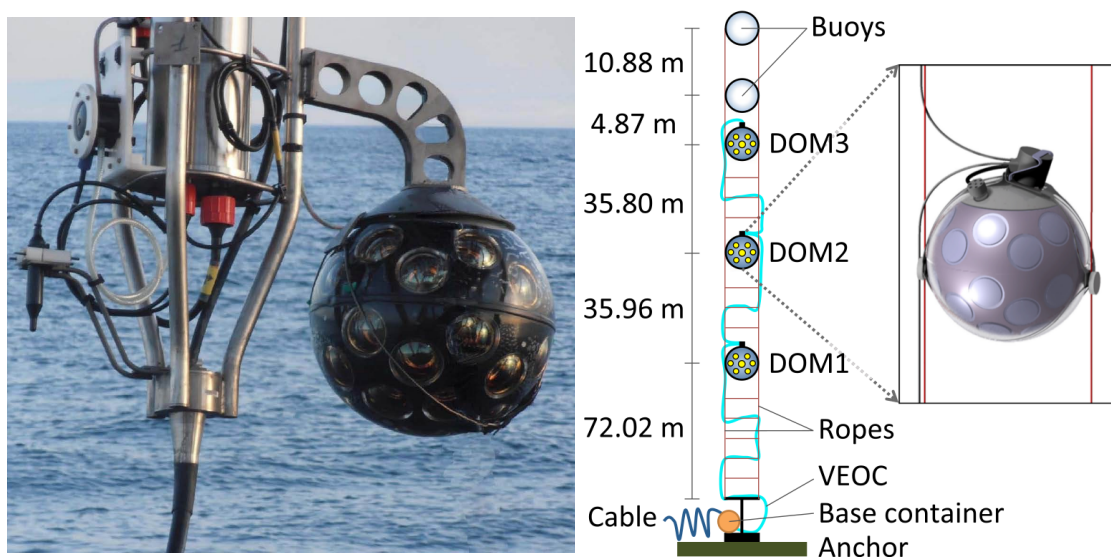


Figure 2.3: Left panel: Prototype DOM connected to the instrumentation line of ANTARES during deployment (18). Right panel: Schematic representation of the PPM-DU at the Capo Passero site (not to scale) (19).

A collection of 115 strings forms a single KM3NeT building block. The modular design makes it possible for building blocks with different spacings between lines/DOMs to be constructed, in order to target different neutrino energies. The full KM3NeT telescope comprises seven building blocks distributed on three sites. Currently, the KM3NeT Collaboration is proceeding with the first construction phase (Phase-1), equivalent to about 0.2 building blocks. For that purpose, 24 strings will be configured for ARCA and deployed at the KM3NeT-Italy site. In addition, the deployment of a group of eight towers is foreseen. These towers, based on the NEMO towers, have 14 floors with 20 m distance between each floor. Although one tower has been

2. THE KM3NET DETECTOR

installed in April 2013, the towers are currently at lower priority for deployment. The layout of this first group of DUs is shown in Figure 2.4 (upper right) with the green dots numbered 1-8 and the red dots numbered 9-32 corresponding to the position of the 8 towers and 24 strings respectively, while JB1-JB3 route the DUs signals to the MEOC. In addition to the already operating cable serving the Phase-1 detector a new cable will be installed for Phase-2 (Figure 2.4, left). Finally, the full KM3NeT telescope comprises seven building blocks distributed on all three sites.

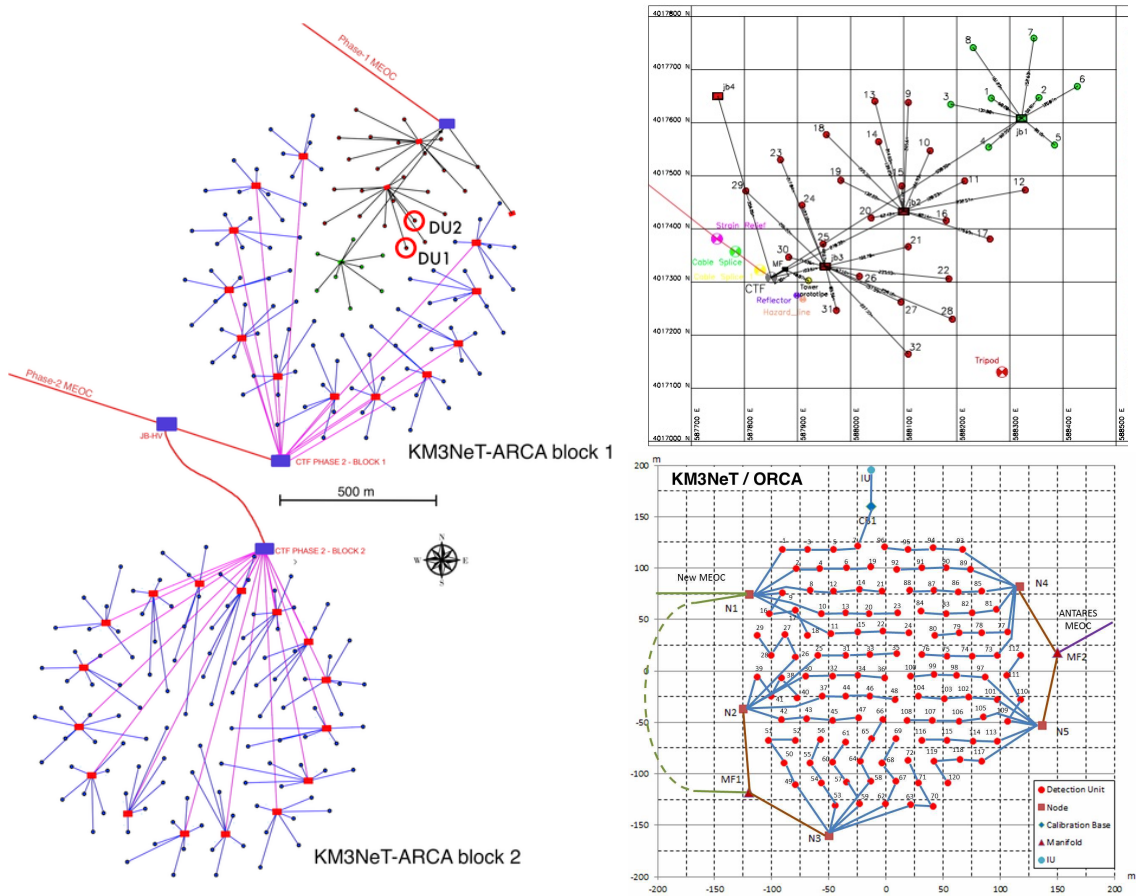


Figure 2.4: Left panel: Layout of the two ARCA building blocks for KM3NeT Phase-2. Upper right panel: Layout of ARCA Phase-1 with its 24 strings (red) and 8 towers (green). Lower right panel: Layout of the ORCA building block. (17)

Three building blocks are planned for Phase-2.0: two KM3NeT/ARCA blocks at the Italian site and one KM3NeT/ORCA block at the French site. The ARCA detector with its two building blocks, will provide an instrumented volume of about one cubic kilometer, i.e. of similar size as the IceCube detector. The horizontal distance between DUs is about 95 m and the vertical distance between adjacent DOMs is 36

2.3 Digital Optical Modules and PhotoMultiplier Tubes

m. The footprint of both blocks is shown in Figure 2.4 (left). Close to the underwater installation the MEOC is split in two branches, each one terminated with a CTF. Each CTF is connected to secondary junction boxes, 12 for the ARCA block 1 and 16 for the ARCA block 2. Each secondary junction box allows the connection of up to 7 KM3NeT detection strings. The layout of the full ORCA array is illustrated in Figure 2.4 (lower right), depicting the 115 (+5 contingency) DUs, cables and connection devices. The strings are connected to five junction boxes, located on the periphery of the array. Each junction box has eight connectors, each of which can power four strings daisy chained in series. Some daisy chains include calibration units, which incorporate laser beacons and/or hydrophone acoustic emitters. In the baseline design, five connectors on the junction box are dedicated for the neutrino array and one is dedicated for Earth and Sea science sensors and two are spares. For the ORCA configuration, the average horizontal spacing between detection strings is about 20 m. Phase-1 of KM3NeT/ORCA will consist of 7 DUs at the French site and a first line was successfully deployed in September 2017.

In this thesis the work will focus on the first phase of the ARCA/KM3NeT telescope and more specifically on the first 24 strings of the detector and will amount to an instrumented volume of about 0.1 km^3 .

2.3 Digital Optical Modules and PhotoMultiplier Tubes

KM3NeT is based on a multi-PMT DOM, which has several advantages over the conventional approach using one single 10-inch PMT or larger. This alternative DOM is built by means of a larger number of small-size PMTs, thus improving the rejection of environmental background and increasing the sensitivity to high-energy neutrinos. The total photocathode area that can be fitted in a standard pressure-resistant 17-inch diameter glass sphere is significantly larger when using many small PMTs as compared to a single large PMT. The segmentation of the detection area in the multi-PMT DOM helps distinguish single-photon from multi-photon hits with high efficiency and purity. Two-photon hits can be unambiguously recognized if the two photons hit separate tubes. Photons arriving in a plane wave from a particular direction may be sensed by 7 PMTs on average. The probability

2. THE KM3NET DETECTOR

that a signal corresponding to two photo-electrons is shared by two small PMTs is thus $(1 - 1/7) \approx 0.85$.

The influence of the Earth's magnetic field on such small PMTs is negligible and thus a μ -metal shielding is not required. Furthermore, the reliability of the multi-PMT DOM is higher since a failure of a single PMT will have much less impact on the performance of the total DOM as compared to an optical module housing a single large PMT. These PMTs are also less subject to aging thanks to a small integrated anode charge. Since handling the data flow from the large number of PMTs in such a DOM becomes challenging, a cost-efficient readout system has been developed with complete digitization inside the DOM.

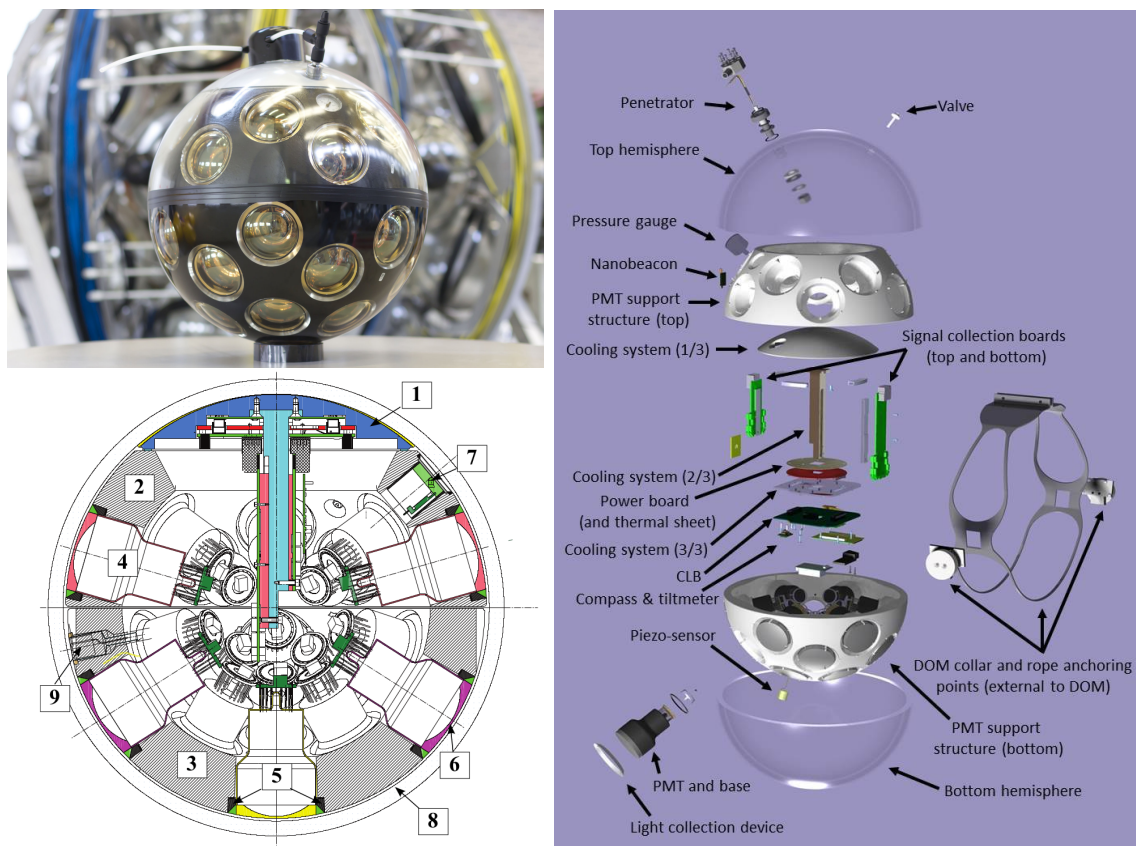


Figure 2.5: Upper left panel: KM3NET Digitale Optical Module. (16, 17) Lower left panel: DOM cross section. The numbers refer to: 1 - Heat conductor; 2,3 - Foam cores; 4 - PMT with PMT base; 5 - Expansion cone; 6 - Optical coupler; 7 - Nanobeacon; 8 - Glass sphere; 9 - Piezo element. Right panel: Exploded view of the DOM's internal structure. (20)

The housing of the multi-PMT DOM is a transparent glass sphere (VITRO-VEX

2.3 Digital Optical Modules and PhotoMultiplier Tubes

glass, wall thickness 14 mm), 432 mm in diameter (see Figure 2.5). The sphere houses 31 PMTs and was built to withstand the ambient hydrostatic pressure up to 600 bar. The sphere is separated into two hemispheres and contains the PMTs, the high-voltage power supplies, front-end and readout electronics. The PMTs are suspended in a foam support structure carrying 12 tubes in the upper hemisphere and 19 in the lower hemisphere. The center of the front face of each PMT is placed 4 mm from the inner surface of the glass sphere. Optical gel fills the cavity between the PMT front face and the glass in order to assure optical contact (optical coupler). The foam support and the gel are sufficiently flexible to make easier the deformation of the glass sphere under the hydrostatic pressure.

The PMTs are arranged in 5 rings with zenith angles of 56° , 72° , 107° , 123° and 148° . In each ring the 6 PMTs are spaced at 60° in azimuth and successive rings are staggered by 30° . The last PMT points vertically downward at a zenith angle of 180° . The expansion cone surrounding each PMT in the multi-PMT DOM is designed to collect photons that would otherwise miss the photocathode, thus increasing the effective photocathode area. As seen in Figure 2.6, the light that comes aside of the PMT entrance window is reflected by the 45° tilted surface into the photocathode. The photon collection efficiency is thus increased by 30% on average by the reflector ring. This opening angle is optimized for maximum collection of light coming perpendicular to the PMT entrance window, which is essential for the direction reconstruction.

2. THE KM3NET DETECTOR

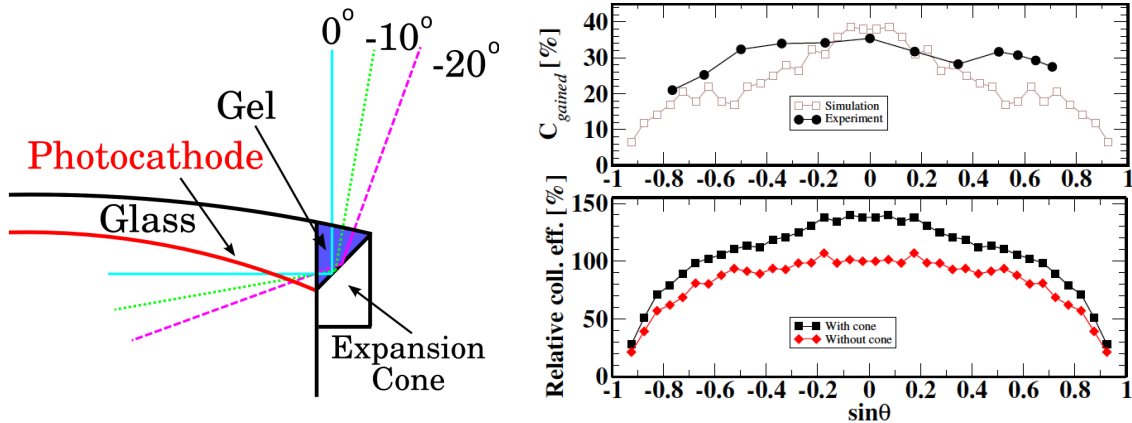


Figure 2.6: Left panel: Depiction of the light collection by an expansion cone. Upper right panel: Gained collection efficiency as a function of the sine of the angle of incidence θ . Lower right panel: Collection efficiency as a function of $\sin \theta$ for a single PMT with and without the expansion cone. (20)

Each PMT has an individual adjustable high-voltage supply integrated in the PMT base. The PMTs collect light and convert it into electronic signals. In order to translate these signals into the arrival time of the photons and the Time-over-Threshold (ToT), they are processed by the Time-to-Digital Converter (TDC) core embedded in the Field Programmable Gate Array (FPGA) which is mounted on the Central Logic Board (CLB). The start time is defined as the time at which the pulse passes beyond a 0.3 p.e. threshold and the ToT is the time the pulse remains above this threshold. The PMT's time resolution is quite small with a Transit Time Spread (TTS) of 4.5 ns (FWHM) thus providing a good timing. The power consumption of a single DOM is about 7 W and the high voltage is set to provide an amplification of 3×10^6 . The PMTs have a convex front face and a ten stage dynode structure with a minimum gain of 10^6 (requiring a supply voltage of ~ 1 kV).

The CLB gathers the signals from all 31 PMTs, arranges them in timeslices of ~ 134 ms and transfers the data to shore via an Ethernet network of optical fibres. Each DOM in a string has a dedicated wavelength to be later multiplexed with other DOM wavelengths for transfer via a single optical fiber to the shore. The broadcast of the onshore clock signal, needed for time stamping in each DOM, is embedded in a Gb Ethernet protocol. The DU base and the shore station integrate a hybrid White Rabbit (WR) protocol, which is a fully deterministic Ethernet-based network

for general purpose data transfer and synchronization, that enables synchronization with sub-nanosecond accuracy and a precision of tens of picoseconds.

A WR link is a pair of nodes, a master and a slave, that are connected via a bidirectional point-to-point link. The WR switches in the shore station form the WR master, and the offshore CLBs are the WR slaves. Instead of having a bidirectional WR link for each slave node (as in standard WR), the master clock signal in the KM3NeT network is distributed via a unidirectional downlink to reack all KM3NeT slave clocks in the CLBs. In return, each CLB has a sperate uplink to shore for the transmission of data. The difference in downlink and uplink paths for the CLBs in the DOM are bypassed by using a hybrid network, which offers a flexibility in the choices of switches for the data processing. In addition, the synchronization procedure differs for the CLBs inside a DOM and CLBs inside a DU base container. This is due to the fact that the CLB in a base container has an uplink with a WR switch, while the CLB in a DOM has an uplink with a standard Ethernet switch.

2.4 Time Calibration

Accurate time calibration (at a nanosecond level) is a critical requirement for a real-time readout system and helps optimize event reconstruction from the signals detected by the different PMTs. This prerequisite is necessary to achieve the desired sub-degree angular resolution for a neutrino telescope. Due to their unique distance from the shorestation, the propagation delay from each digital optical module will be different. These offsets, together with the clock phases, enable time calibration of the data coming from different PMTs and have been measured in situ through powerful light pulse emitters, installed throughout the detector. Time calibration work has been carried out after the deployment of the PPM-DOM, the PPM-DU and both DU1 and DU2, and was determined through:

- intra-DOM calibration (between PMTs in the same DOM), which primarily depends on the PMT transit time, and thus on the electronics inside the DOM and the PMT properties;
- inter-DOM calibration (between DOMs), which primarily depends on LED nanobeacons and also on cable lengths.

2. THE KM3NET DETECTOR

- inter-DU calibration (between DUs), which relies on laser beacons and also on cable lengths, including those between DUs.

Radioactive decays of ^{40}K present in sea water typically produce up to 150 Cherenkov photons per decay (see Chapter 1.2.1). These decays are the main source of the singles rates observed in the PMTs. A single decay occurring in the vicinity of the DOM has a chance to produce a genuine coincidence between signals of different PMTs, which can be exploited for intra-DOM time calibration. On the other hand, each DOM is equipped with a LED nanobeacon, capable of illuminating the surrounding DOMs up to a distance of approximately 400 meters, which can be used to perform the inter-DOM time calibration. The laser beacons are used to monitor the relative offsets among DUs. Since the laser light from the laser at the bottom of the detector is emitted sideways, the laser light can be detected by the lowest DOM in several neighbouring DUs.

2.4.1 Intra-DOM Calibration

The in situ PMT time calibration is based on the observation of light from ^{40}K decays in the seawater. A DOM is capable of detecting multiple photons from a single ^{40}K decay because it contains many PMTs, making it possible to look for coincidences of hits within a single optical module. The vast majority of coincident hits on ≥ 2 PMTs within a DOM in a time window of 20 ns (called ‘‘L1 hits’’) are caused by ^{40}K decays in the vicinity of the DOM. The distribution of the hit time difference between these coincident hits is expected to be approximately gaussian distributed, where the mean is the difference between the transit times (t_i^0) of the PMTs involved, the width is related to the PMT’s transit time spreads (TTS_i) and the integral scales with the product of the PMT efficiencies E_i . The distribution of the hit time difference $R_{i,j}(\Delta t)$, can be parametrized as follow (21)

$$R_{i,j}(\Delta t) = R(\theta_{i,j}) \times E_i \times E_j \times \frac{1}{\sqrt{2\pi}\sigma_{i,j}} \times \exp\left[\frac{(\Delta t - t_i^0 + t_j^0)^2}{2\sigma_{i,j}^2}\right] + R_{i,j}^{random} \quad (2.1)$$

$$\text{where } \sigma_{i,j}^2 = TTS_i^2 + TTS_j^2 + \sigma_{40K}^2 \quad (2.2)$$

In this the parametrization of the expected total coincidence rate of a PMT pair $R(\theta_{i,j})$ and intrinsic time spread due to the spatial distribution of the ^{40}K decays

(σ_{40K}) are determined from dedicated Monte Carlo (MC) simulations. The PMT efficiency is a single number assigned to each PMT to quantify how well it performs in situ compared to the PMT model implemented in the MC simulations.

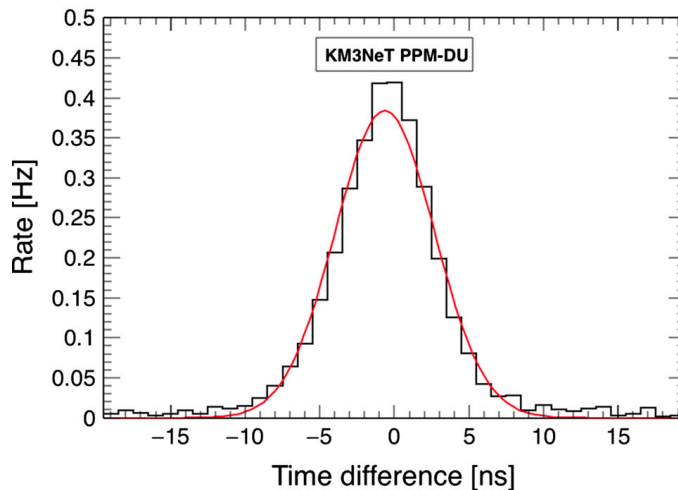


Figure 2.7: Distribution of time differences between the hit times of two adjacent PMTs in DOM1 for one physics run. The red line represents a simultaneous fit of a Gaussian function. The baseline due to combinatorial background has been subtracted from the data (19).

In Figure 2.7, the clear Gaussian peak centered near zero indicates the detection of two photons from the same ^{40}K decay; the flat combinatorial background due to uncorrelated hits on the two PMTs has been subtracted.

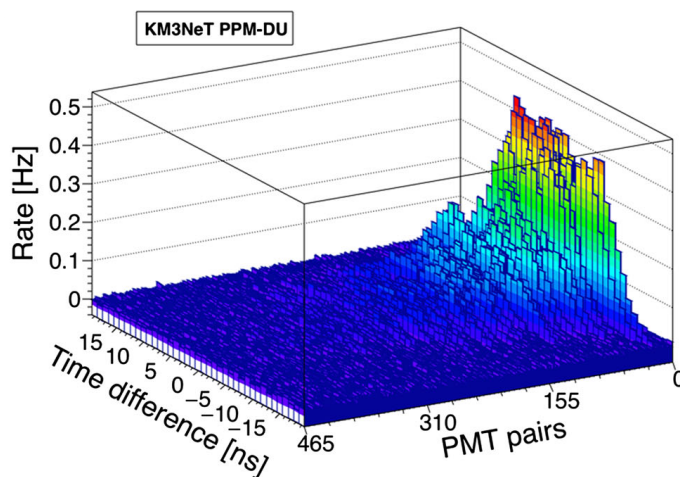


Figure 2.8: Distribution of time differences between the hit times for all PMT pairs in DOM1 for one physics run. The PMT pairs are ordered according to their angular separation (19).

2. THE KM3NET DETECTOR

In Figure 2.8 is shown the time difference between hits in all the possible PMT pairs in a DOM ($\frac{31(31-1)}{2}$) for increasing PMT angular separation. The correlation peak decreases as the angular separation increases due to the limited field of view of each PMT. When the PMTs are back to back the peak disappears leaving only a flat background from random coincidences $R_{i,j}^{random}$, which will be determined by a fit of the tails of each distribution and subtracted from the Δt distributions. A fitting procedure that minimizes the χ^2 is applied to the spectra shown in Figure 2.8 to obtain simultaneously the transit time, TTS and detector efficiency.

As mentioned before, the distribution of hit times differences between all possible combinations of PMT pairs are assumed to follow a Gaussian shape. The mean values, heights and widths of the Gaussian peak are related to the time offsets, efficiencies and intrinsic time spreads of all the PMTs. Typically, a FWHM of 7-10 ns is found for all different PMT pairs, reflecting the intrinsic PMT TTS of up to 5 ns (FWHM). The results of the fitting procedures on these distributions, based on the χ^2 minimum, are reported in (19). They show that the relative time offsets and PMT detection efficiencies are stable over time scales of months.

2.4.2 Inter-DOM Calibration

The time offset between two neighboring DOMs is determined by means of LED nanobeacons. In seen in Chapter 2.3, a nanobeacon is mounted inside each DOM and produces a short light pulse at a fixed wavelength of 470 nm. The LED nanobeacon of a DOM is seen by a selection of PMTs in the lower half of the higher floor DOMs, making it possible to perform the inter-DOM calibration. In Figure 2.9, preliminary results extracted from DU2 are presented. This Figure displays the nanobeacon visibility of DOM1 on a series of higher DOMs during a chosen run. Consequently, decreasing peaks of hits over pulse were recorded by DOM3 to DOM11 with respect to an increasing calibrated hit time, as the each DOM's distance to DOM1 also increases.

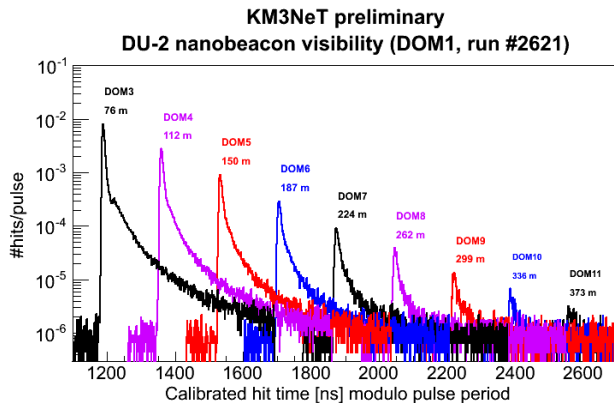


Figure 2.9: DU2 nanobeacon visibility of DOM1 on DOMs 3 to 11 during a chosen run (2621), with the number of hits/pulse as a function of the calibrated hit time (modulo the pulse period) in nanoseconds.

Reconstructing atmospheric muon tracks helps determine the inter-DOM time offsets. In this method muon tracks are reconstructed without using the element of the detector to be time calibrated. If adequate quality cuts are applied, well-reconstructed events can be used as the “true” track, with a small enough error margin. Therefore, the hit times of the excluded element can be compared with what is expected from the reconstructed tracks. Deviations from these expected times can be attributed to misalignment in the assumed time offsets. This procedure can be performed using DUs and DOMs, and each of these would provide the time calibration at different levels (inter-DU and inter-DOM respectively). The track selection would be optimized for each case. Regarding the inter-DOM algorithm, all events with at least 7 DOMs registering an L1 hit are reconstructed, iteratively excluding one of the hit DOMs from the track fit. The distribution of the time difference between the measured hit time on the excluded DOM and the expectation from the reconstructed track, referred to as the hit time residual distribution, is compared to the distribution obtained by applying the same procedure to Monte Carlo simulated events (Figure 2.10).

2. THE KM3NET DETECTOR

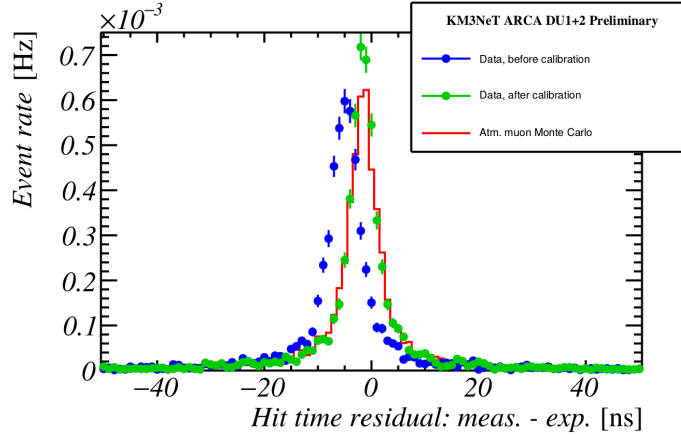


Figure 2.10: Hit time residual distributions obtained from Monte Carlo simulations (red) and data before (blue) and after (green) DOM time offset calibration (21).

The set of Monte Carlo simulated events has been produced on a run-by-run basis, including a detailed model of the PMTs using the fitted PMT efficiencies determined with the ^{40}K intra-DOM calibration method. Furthermore the atmospheric muon flux, photon propagation through the sea water and detector response are simulated (using simulation packages that will be presented in Chapter 4). As seen in Figure 2.10, the hit time residual distribution before calibration does not peak at zero, indicating that the DOM time offset is not yet calibrated. It is thus important to maximizing the agreement between the data and the Monte Carlo model in order to obtain the best fitting DOM time offset. Since the reconstructed track parameters are correlated with the DOM time offsets, the maximization procedure is repeated until convergence is achieved.

2.5 First Results

2.5.1 PPM-DU

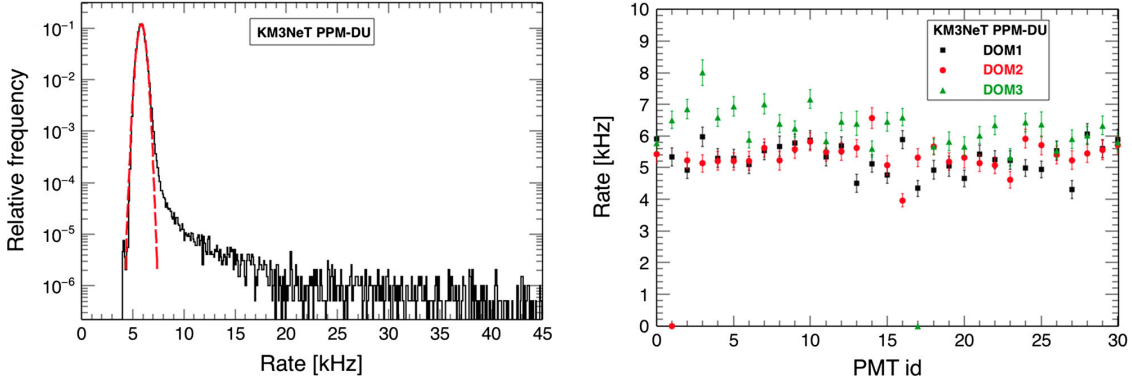


Figure 2.11: Left panel: Rate distribution per timeslice of 134 ms for PMT 16 of DOM1. Right panel: Average value of the singles rates per PMT for the 3 DOMs of PPM-DU per timeslice of 134 ms (19)

The distribution of the average singles rate for one PMT of DOM1 in the PPM-DU is shown in the left panel of Figure 2.11. The Gaussian distribution, peaking at about 6 kHz, is mainly due to ^{40}K decays; the second contribution is due to sporadic bioluminescence background. In the right panel of Figure 2.11, the average values of the Gaussian fit are plotted for all PMTs of the PPM-DU's three DOMs per timeslice of 134 ms, and the error reflects the standard deviation of the fit. The rate was found to be stable over the observation time of seven months within a few percent. Note that in DOM2 and DOM3 only 30 PMTs are involved in the data acquisition. The higher rate of DOM3 can be explained by the fact that it contains PMTs with a larger photo-cathode area and larger reflector rings (Hamamatsu R12199-02) with respect to DOM1 and DOM2 (ETEL D783KFLA). The average coincidence rates for each DOM, and the corresponding r.m.s error, are then given in Table 2.1. The results are summed over the whole DOM. The ratio between the DOM rates is expected to reflect the ratio between the DOM efficiencies to the power of the coincidence multiplicity. This is approximately the case up to a coincidence multiplicity of five. Above this value, the signal on PMTs is not due to single photo-electron producing processes, such as ^{40}K decay, and this relation no longer holds. It is worth mentioning that above a coincidence multiplicity of three the combinatorial background becomes negligible.

2. THE KM3NET DETECTOR

Coincidences	DOM1 [Hz]	DOM2 [Hz]	DOM3 [Hz]
Single	$(166 \pm 4) \times 10^3$	$(162 \pm 12) \times 10^3$	$(188 \pm 14) \times 10^3$
2-fold	307 ± 5	278 ± 5	473 ± 7
3-fold	23.1 ± 0.5	18.6 ± 0.7	44.1 ± 0.9
4-fold	2.03 ± 0.07	1.35 ± 0.08	4.89 ± 0.19
5-fold	0.17 ± 0.02	0.10 ± 0.02	0.53 ± 0.04
6-fold	0.018 ± 0.005	0.012 ± 0.005	0.057 ± 0.011
>6-fold	0.017 ± 0.006	0.017 ± 0.006	0.030 ± 0.011

Table 2.1: Average coincidence rates for the three DOMs, for a time window of 25 ns (19).

2.5.2 DU1 and DU2

The photon counting capability and the directionality provided by the photocathode segmentation already enables a single DOM to identify muons and to be sensitive to their arrival directions, proving it possible for even a single DOM to reject the background and unambiguously identify muon induced signals by selecting high multiplicity coincident hits (18). This conclusion can also be drawn from Figure 2.12 where, for 19.5 days worth of data, the coincidence rates are shown as a function of the multiplicity for the lowest floor of DU 1 and the highest floor of DU 2. The data are compared with a Monte Carlo simulation including both the ^{40}K background and the contribution of atmospheric muon events. The rates decrease rapidly as a function of the coincidence level. At low multiplicities ($m < 7$) the signals from ^{40}K dominate the rates while the muon signature becomes dominant for higher multiplicities. Thus when applying a cut of $m \geq 8$, the selected coincidences will be dominated by the atmospheric muon signal along the entire length of the DUs. Whether we are considering the lower or the higher coincidence levels, data and MC are in good agreement over the entire range, thus providing an extra handle for the identification of muons and allowing for a more precise reconstruction of the direction of the associated particles.

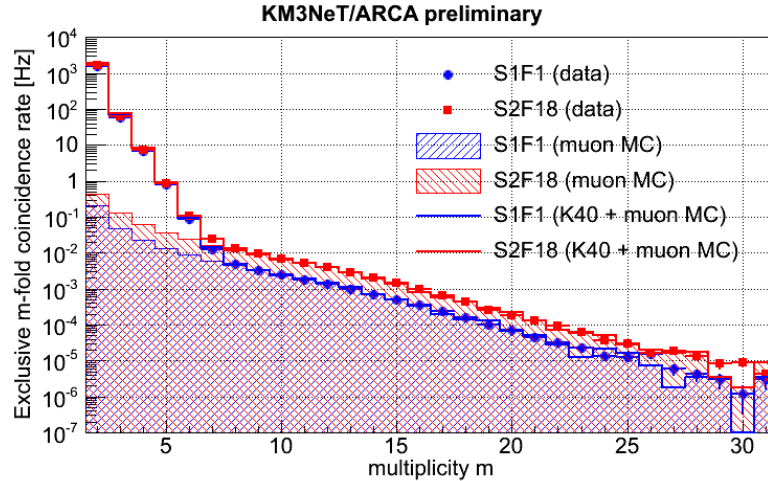


Figure 2.12: Coincidence rate as a function of the multiplicity. Floor 1 of ARCA-DU1 and floor 18 of ARCA-DU2 are shown. The data are overlaid with the expectations from MC simulations of ^{40}K and atmospheric muons. The PMT efficiencies in the ^{40}K simulation have been varied within the systematic uncertainties in order to match the slope observed in data (22).

Figure 2.13 shows the rate of ≥ 8 -fold coincidences as a function of depth (22). The red dashed line is obtained with a Monte Carlo simulation of a detector with identical PMTs. However, large deviations from this ideal detector behaviour are observed in data. In order to correct the data for the different PMT responses the PMT efficiencies determined using the previously discussed ^{40}K calibration were taken into account. A full atmospheric muon MC incorporating these measured PMT efficiencies was produced and compared to the ideal MC with uniform PMT efficiencies. For each DOM, the ratio of the rates observed in these two MC simulation sets was then used to correct the data. These corrected data points are shown in Figure 2.13 along with the uncorrected data. The corrected data points follow the expected ideal behaviour more closely, showing that the in situ calibration improves the agreement between data and Monte Carlo simulations.

2. THE KM3NET DETECTOR

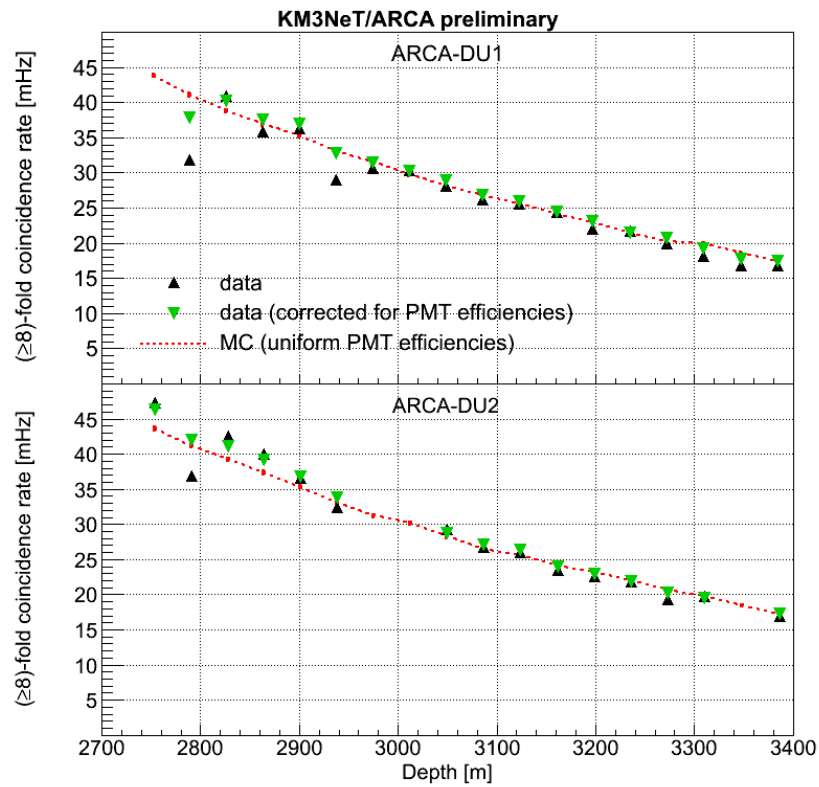


Figure 2.13: ≥ 8 -fold coincidence rate as a function of the depth below the sea surface (22). The red dashed line shows the base expectation from an ideal MC with uniform PMT efficiencies which neglects the differences between individual PMTs. The black points show the uncorrected data. The green points show the data corrected for the effect of the PMT efficiencies. Statistical errors bars are included but are too small to be visible over the markers.

Chapter 3

HIGH-ENERGY NEUTRINO ASTRONOMY

Astrophysics, and more specifically astroparticle physics, has been going through tremendous progress during the last decades. Cosmic observations through various types of messengers has allowed multi-messenger astronomy to widely extend our knowledge of the Universe. Nevertheless many discoveries are left to be made.

One of the ultimate goals of astrophysics is to piece together information from cosmic-ray, neutrino telescopes, telescopes measuring electromagnetic radiation (gamma-ray, optical, infrared, radio, X-ray), and more recently, gravitational waves, into a coherent picture of the inner workings of distant astrophysical objects. Each of these types of particles can provide valuable clues, and there are advantages and disadvantages to each type of study. The detection of cosmic-rays, which are particles accelerated to the highest energies in the sources, has complemented later gamma-ray observations as the emission of the latter have been associated to cosmic-ray production. Yet together with gamma-rays, astrophysical neutrinos are also expected to be the result of cosmic-ray interactions in the cosmic environment.

Neutrino astrophysics is a very active field of research at the present time as neutrinos are key information carriers from violent astrophysical processes. An attractive property of neutrinos is in fact their feeble interactions with their surroundings, which means they can penetrate regions with dense matter without being absorbed and are not deflected by interstellar magnetic fields. Where other particles become trapped or can only propagate through very slow diffusive processes, neutrinos are able to escape. Neutrinos can thus connect regions of matter that would otherwise be isolated from each other, and because they are almost massless, they move effectively at the speed of light. Unfortunately, the fact that neutrinos are so weakly

3. HIGH-ENERGY NEUTRINO ASTRONOMY

interacting also means that they are extremely difficult to detect.

Nevertheless neutrinos can provide information from astrophysical environments, obscure to high-energy gamma-rays and charged particles. Since neutrinos can only be produced in hadronic processes, the detection of even a faint flux of high energy astrophysical neutrinos will also reveal the nature of the most energetic phenomena in the most powerful astrophysical systems. Furthermore, considering the combination of several unresolved cosmic sources of high-energy neutrinos, their integrated flux can be detected before the flux of any individual source can reach the detection threshold.

3.1 Cosmic-Rays

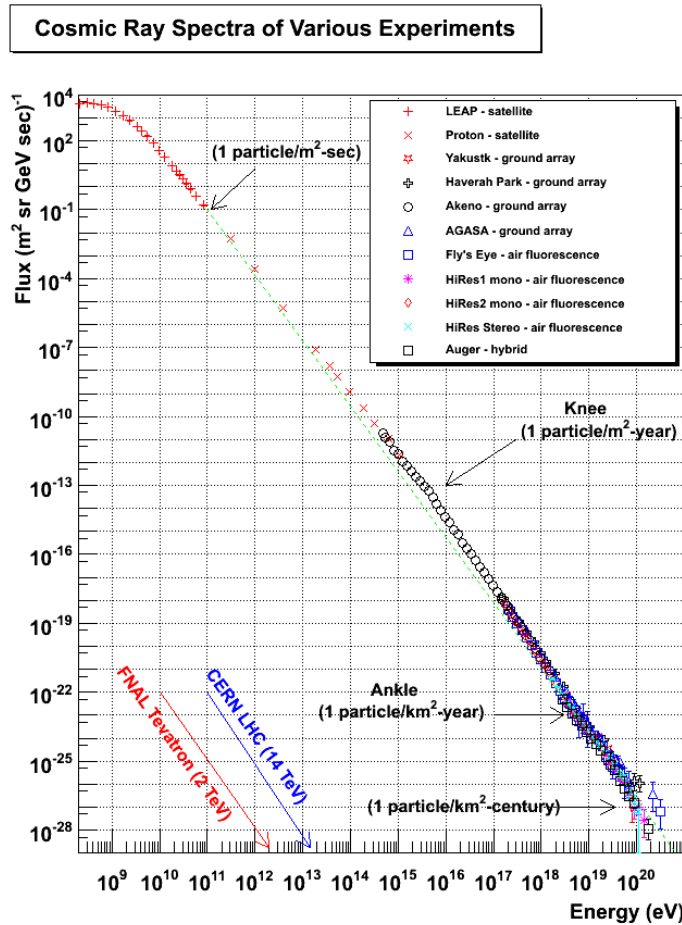


Figure 3.1: The all-particle cosmic ray spectrum and the various experiments relevant for its detection (23).

The atmosphere of the Earth is steadily bombarded by an isotropic flux of charged particles, mostly protons and heavy nuclei, called cosmic-rays (24, 25, 26, 27). They interact with atmospheric nuclei, revealing their existence on the ground by indirect effects such as ionization and formation of showers of secondary charged particles. The discovery of cosmic-rays (CRs) is attributed to Victor Hess who, in 1912, flying in a balloon to an altitude of 5 km discovered that the ionization of the air strongly increases with altitude (28). The only explanation of his measurement, he believed, was that “a radiation of very high penetrating power enters the atmosphere from above”. Despite a century of studies CRs are still a puzzling subject for physicists.

The CR flux extends over many orders of magnitude in energy, up to at least several 10^{20} eV. The differential all-particle flux, shown in Figure 3.1, drops by 32 orders of magnitude down to few particles per 100 km^2 per century, thus requiring different detection techniques for each energy range. At energies below $\sim 10^{14}$ eV a direct measurement is possible through atmospheric balloons or satellites permitting an accurate study of the cosmic ray composition. At higher energies the CRs detection requires detectors with large areas that must be exposed for periods of time too long to be placed on board of a satellite. The measurement is possible only in big infrastructures located on the ground. Such detectors, called air shower arrays, can cover areas of many km^2 and detect the remnants of the atmospheric cascades of particles initiated by the incident primary particle. Another technique used in this energy range is represented by the detection of the fluorescence light produced by the passage of charged particles through the atmosphere and subsequent nitrogen excitation and disexcitation. None of the two techniques is particularly effective in identifying the nature of the primary. Recent experiments, such as The Pierre Auger Observatory (29) in the southern hemisphere and Telescope Array (30) in the northern hemisphere, use both the techniques.

The spectrum in Figure 3.1 incorporates the results of many different experiments. At energies less than ~ 1 GeV it can be explained by the solar activity, in fact at such energies the solar wind shields charged particles coming from outside the solar system. Above a few GeV the CR energy spectrum follows a $E^{-2.7}$ power law up to $E \simeq 3 \times 10^{15}$ eV (3 PeV). At this energy the CR spectrum steepens to a power law E^{-3} , with a break usually referred as “the knee”. This distinct spectral feature may sign the limitation of the confinement in the galaxy (31) and is accompanied by a

3. HIGH-ENERGY NEUTRINO ASTRONOMY

gradual change of composition from light to heavy nuclei, with consecutive cut-off in the flux of the individual mass components starting with protons at a few 10^{15} eV up to iron at around 10^{17} eV as confirmed by the experimental results (32).

At $E \simeq 5 \times 10^{18}$ eV the cosmic ray spectrum flattens again to a power law $E^{-2.7}$ with a break called “the ankle”, interpreted as a crossover of the fading galactic component and the rising of a harder extragalactic component. Cosmic rays above 10^{18} eV are usually called Ultra High Energy Cosmic Rays (UHECR). In the energy region of the ankle, air shower measurements indicate a decrease of the average mass of cosmic rays but at energies higher than $10^{18.5-19}$ eV, the experimental uncertainties are still too large to draw firm conclusions. The knowledge of the UHECR mass composition is an extremely relevant piece of information for the possibility of doing proton astronomy, because only UHE protons could be good astrophysical probes. In fact, the galactic magnetic field $B_G \simeq 3\mu\text{G}$ causes particles with charge Z and energy E to describe helical trajectories with a Larmor radius $R_L = E/(ZeB_G)$ that for a proton with $E \simeq 10^{18}$ eV is of the same order of the thickness of the Galactic disc halo ($\simeq 300$ pc), and for $E \simeq 5 \times 10^{18}$ eV is of the order of the Galactic disk radius ($\simeq 15$ kpc). Therefore, protons with $E > 10^{18.5-19}$ eV go approximately along a straight line while this is not true for heavier nuclei, since R_L depends on Z .

One of the open questions about the highest energy component of the CRs spectrum concerns the Greisen-Zatsepin-Kuzmin (GZK) cutoff (33, 34), which imposes a theoretical upper limit on the energy of cosmic rays from distant sources. Above a threshold of few 10^{19} eV, protons interact with the 2.7K Cosmic Microwave Background radiation (CMB) and lose energy through the resonant pion production

$$p + \gamma \rightarrow \Delta^+ \rightarrow \begin{cases} n + \pi^+, & 1/3 \text{ of all cases} \\ p + \pi^0, & 2/3 \text{ of all cases} \end{cases} \quad (3.1)$$

The threshold energy for the $p\gamma$ interaction is $E_p \simeq 6 \times 10^{19}$ eV with a cross section of $\sigma_{p\gamma} \simeq 100\mu\text{barn}$ so, considering that the average CMB radiation density is $n_\gamma \simeq 400 \text{ cm}^{-3}$, the absorption length of ultra high energy protons in the Universe is roughly

$$L_{p\gamma\text{CMB}} \simeq (n_\gamma \cdot \sigma_{p\gamma})^{-1} < 50 \text{ Mpc} \quad (3.2)$$

well shorter than the distance between cosmological sources and the Earth. A strong suppression of the CR flux is therefore expected above the GZK threshold. Recent measurements made by HiRes (35), Auger (36) and TA (37) experiments are consistent with the presence of a GZK effect. Even in the hypothesis of composition dominated by protons, the proton bending due to cosmic magnetic field and the GZK effect, shrinks the energy and distance region accessible to UHE proton astronomy between 10^{19} eV and $10^{20.5}$ eV to a few hundreds Mpc in distance. Another open question is whether the CR spectrum continues to energies higher than 10^{20} eV, and due to limited statistics or due to the presence of a hard cutoff for physical reasons, it has yet to be detected. Nevertheless, the extension of the proton spectrum to some PeV is crucial for the effective production of neutrinos in the 10-100 TeV range, the optimal energy interval for the TeV neutrino detectors such as IceCube and KM3NeT.

The mechanism most likely responsible for accelerating particles up to observed CR energies is known as “shock acceleration” or “first order Fermi acceleration”. This process occurs when two plasmas collide, forming a shock at the boundary. In this model, particles are magnetically confined to the source and they are elastically scattered by magnetic irregularities that are frozen into the plasma. The continuous scattering on both sides of the shock front result in an energy gain. The differential energy spectrum predicted by the Fermi mechanism is an E^{-2} power law. The observed CR differential energy spectrum is steeper than the typical spectra predicted by the shock acceleration mechanism. Models of CR propagation explain the changing of the spectral index with the CR propagation in the irregular component of the Galactic magnetic field and the nuclear interactions with the gas present in the interstellar medium. Several astrophysical environments are identified as possible candidate where the Fermi acceleration mechanism can take place. Although theories for particle acceleration in the astrophysical plasma have empirical foundation, the models would benefit greatly from neutrino astronomy, which provides crucial information about the accelerated proton spectra at the sources, unaffected by propagation effects.

3.2 Neutrino Astronomy

The direct measurements of cosmic-rays are very important, but can hardly address all outstanding issues alone, in particular the ones related to the localization and identification of the sites of particle accelerators. By looking at the astrophysical neutrino signal, more details can be obtained about the origin of cosmic neutrinos and of ultra-high-energy cosmic-rays (UHECR).

3.2.1 Neutrinos from Hadronic Processes

Some of the possible UHECR sources are associated with relatively dense concentration of matter or a photon field. Such a configuration, in which accelerated particles interact with material near their source, is usually called “astrophysical beam dump”. Photomeson production is an important channel for the transformation of the kinetic energy of protons into high-energy gamma-rays, electrons and neutrinos. However, sources of UHECR are not the only sources of astrophysical neutrinos; while sources of UHECR can pinpoint the sources of high-energy neutrinos, the latter are generated everywhere hadrons are accelerated.

As in Equation 3.1, accelerated protons interact in the surroundings of the CRs emitter with photons, generating pions in the final state but protons will also interact with ambient matter (protons, neutrons and nuclei), giving rise to the production of charged and neutral mesons:

$$p + p \rightarrow \begin{cases} \pi^+ + \text{anything, } 1/3 \text{ of all cases} \\ \pi^0 + \text{anything, } 1/3 \text{ of all cases} \\ \pi^- + \text{anything, } 1/3 \text{ of all cases} \end{cases} \quad (3.3)$$

Neutral pions then decay in photons while charged pions decay in neutrinos:

$$\pi^0 \rightarrow \gamma + \gamma \quad (3.4)$$

$$\begin{aligned} \pi^+ &\rightarrow \mu^+ + \nu_\mu & (3.5) \\ &\hookrightarrow e^+ + \bar{\nu}_\mu + \nu_e \end{aligned}$$

$$\begin{aligned} \pi^- &\rightarrow \mu^- + \bar{\nu}_\mu & (3.6) \\ &\hookrightarrow e^- + \nu_\mu + \bar{\nu}_e \end{aligned}$$

The threshold energy of the $p\gamma$ reaction in the center-of-mass reference frame is roughly $E_p \simeq 300$ MeV and the pion carries about 20% of the proton energy. This energy is statistically equally divided among the final decay chain products so each neutrino carries $\sim 5\%$ of the interacting proton energy. Close to the threshold energy, the process proceeds through single pion production but at higher energies, multi-pion production channels begin to dominate. In the framework of the hadronic model and in the case of transparent sources, the energy escaping from the source is distributed between CRs, gamma-rays and neutrinos. A transparent source is defined as a source of a much larger size than the proton mean free path, but smaller than the meson decay length. For these sources, protons have large probability of interacting once, and most secondary mesons can decay.

The cross-section of these processes is basically well known from particle acceleration experiments. The cross sections of interactions of secondary electrons and gamma-rays with the ambient photons exceed by three orders of magnitude the photomeson cross-sections. Therefore they cannot leave the active region of pion production, but rather initiate electromagnetic cascades in the surrounding photon and magnetic field. The standard spectra of low-energy cascade gamma-rays that eventually escape the source are not sensitive to the initial spectral distributions, and thus only contain information about the total hadronic power of the source. On the other hand the secondary neutrinos freely escape the production region, and thus carry direct information about the energy spectra of accelerated protons.

The presence of dense photon fields in the compact particle accelerators may have an even more fundamental impact. In relativistic flows, the multiple conversions of relativistic particles from charged to neutral state may facilitate a strong energy gain in each cycle; whereas, in the standard relativistic shock acceleration scenario, the energy gain occurs only in the first cycle. This shock acceleration mechanism is only valid for charged particles. Electrically neutral particles, such as photons or neutrinos, are the decay products of accelerated charged particles.

The flavor ratio at the time of the neutrino production in the source is commonly expected to be $\nu_e : \nu_\mu : \nu_\tau = 1 : 2 : 0$, (ν and $\bar{\nu}$ are both counted in the neutrino

3. HIGH-ENERGY NEUTRINO ASTRONOMY

flux as it is labelled here) but due to averaged flavour oscillation of neutrinos during their journey from the astrophysical source to Earth, equipartition between the three leptonic flavors ($\nu_e : \nu_\mu : \nu_\tau = 0.93 : 1.05 : 1.02 \approx 1 : 1 : 1$) is expected at the Earth (38). Although the most commonly considered scenario at the source is 1:2:0, the composition could vary from 0:1:0 to 1:0:0 under a multitude of scenarios including muon energy loss in high matter density or magnetic fields, muon acceleration, and neutron decay. For a composition varying from 0:1:0 to 1:0:0, the composition at Earth varies linearly from 0.6:1.3:1.1 to 1.6:0.6:0.8 . Therefore, observing unequal or energy-dependent flavor contributions would be interesting since the flavor ratio is also sensitive to the assumed production mechanism at the source.

3.2.2 Astrophysical Neutrino Sources

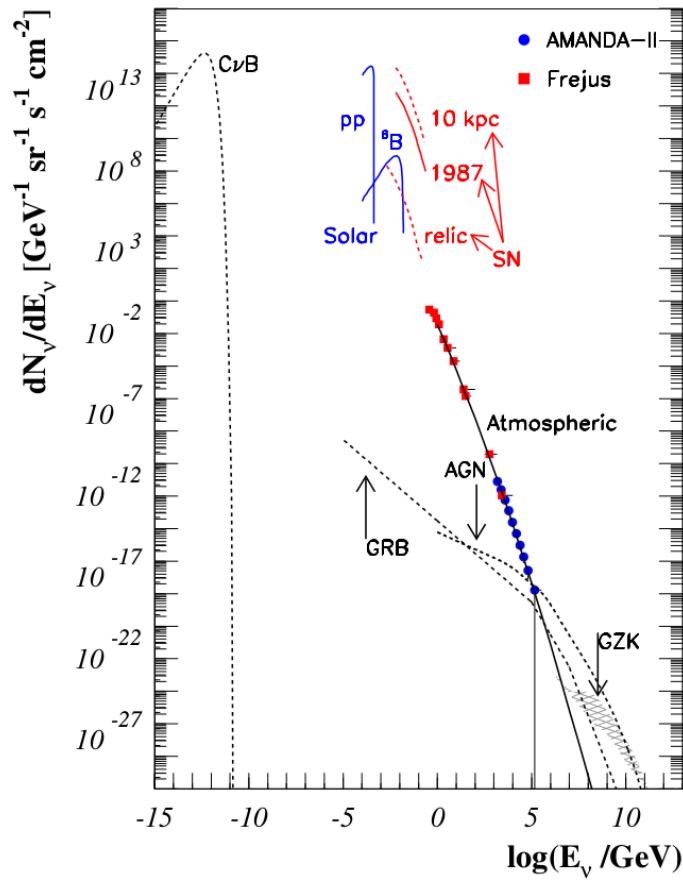


Figure 3.2: The astrophysical neutrino spectrum including different source predictions (39). The fluxes based on mere predictions are shown as dashed lines while the solid lines represent those fluxes already measured. Point source fluxes have been scaled by $1/4\pi$ in order to be comparable to diffuse spectra.

One century after the discovery of cosmic-rays the search for their sources is still ongoing. As mentioned previously, neutrinos are expected to be generated from interactions of cosmic-rays with photon or matter fields in or near the accelerating astrophysical objects. Therefore, the detection of high-energy neutrinos from such objects would provide a unique possibility to identify individual astrophysical objects as cosmic-ray sources. An overview of the measured or expected neutrino spectrum at the Earth is shown in Figure 3.2. From the lowest energies of $E \sim \text{meV}$ to the highest energies of $E \sim \text{EeV}$, the expected intensity of the signal decreases by more than 40 orders of magnitude. The figure is a mixture of observations and theoretical predictions.

3. HIGH-ENERGY NEUTRINO ASTRONOMY

At low energy, the neutrino sky is dominated by the yet unobserved Cosmic Neutrino Background ($C\nu B$), an isotropic neutrino flux having decoupled in the early Universe, already 1 s after the Big Bang and corresponding to the cosmological relic black-body spectrum at a temperature of about 1.9 K. Detection of these neutrinos is an extremely challenging experimental problem which can hardly be solved with the present technologies. Neutrinos with $E \sim \text{MeV}$ energy are produced by the Sun and by supernova explosions. The sun emits neutrinos in different fusion processes. Among the most spectacular events in astrophysics are supernova explosions. In a few seconds, more energy is released in neutrinos from the forming neutron star than all the electromagnetic emission from an entire galaxy over a decade.

At $E > 0.1 \text{ GeV}$, neutrinos produced by cosmic-ray interaction in the atmosphere appear in the spectrum (more details in Chapter 3.4). Atmospheric neutrinos are measured up to energies of 100 TeV and represent the dominant background for extraterrestrial searches. The highest energy neutrinos are those expected from the absorption of protons by the GZK effect. The interaction of the cosmic-rays with the microwave photons of the CMBs limits their mean free path to less than 100 Mpc producing a Δ -resonance that decays in pions and then in neutrinos. This produces a diffuse flux of cosmogenic (or GZK) neutrinos.

A large number of neutrino sources are believed to be located in our Milky Way galaxy and are mainly associated with SuperNova Remnants (SNRs), Pulsar Wind Nebulae (PWN), X-ray binaries and microquasars. On the other hand, Active Galactic Nuclei (AGN) and Gamma Ray Bursts (GRBs) are among the extra-galactic objects that could be producing neutrinos. They are all considered possible sources in which particles are accelerated to high energies through shock acceleration processes, and because of their unique properties, neutrinos could escape even dense regions, be undeflected in galactic or extra-galactic magnetic fields and traverse the photon-filled universe unhindered. Unfortunately, a Galactic component of high-energy neutrinos has yet to be determined. There are only upper limits on this flux, provided by nine years of ANTARES data (40) and seven years of IceCube data (41).

The stellar evolution can end with a phase called “Supernova”, in which the whole star explodes and its envelope is ejected at supersonic velocity producing shock waves that move outwards from the central star and giving rise to SNRs. It is widely be-

lieved that the bulk of CRs up to the knee (about 10^{17} eV) is Galactic, produced and accelerated by the shock waves of SNR expanding shells. The main phenomenological argument in favor of this hypothesis is the CR production rate in the Galaxy, with one supernova releasing about 10^{51} erg every 30 years. This can be supported by SNRs if approximately 10% of the kinetic energy of the galactic SN explosions is released in CRs (42). However, this postulate has not been unambiguously established because of the difficulty in disentangling the electronic component from the π^0 -decay component signing hadronic acceleration. The observation of high-energy neutrinos from these sources would provide an incontrovertible proof of hadronic acceleration.

The second argument has a more theoretical background. It is linked to the potential of the so-called “Diffuse Shock Acceleration” (DSA) mechanism which may convert with a high efficiency the available kinetic energy of the bulk motion to relativistic particles. It is the most promising mechanism for accelerating protons to the energies observed in the cosmic-ray spectrum below the knee; under fairly general conditions this is expected to produce a flux of protons with a power-law spectrum at the source similar to $dN/dE \propto E^{-2}$.

Pulsars, rapidly rotating neutron stars left over after supernova explosions, are sources of high energy gamma-rays. Their rotational energy is converted into the kinetic energy of the pulsar wind, a plasma of relativistic electrons and positrons that terminates in a shock when it encounters the ambient medium. The termination shock is the place where additional particle acceleration can take place.

X-ray binaries are binary systems consisting of compact object, such as a neutron star or a black hole, called “accretor” and a companion star, the “donor”, that feeds the accretor with mass through an accretion disc. The compact object in turn emits the energy gained in form of X-rays. A special case of an X-ray binary is the so-called microquasar, in which the compact object exhibits relativistic radio jets. Such a phenomenon is believed to be caused by instabilities in the accretion disk of the system. A burst is caused every time a particularly large amount of matter is accreted from the accompanying star. Protons, accelerated at energies > 100 TeV by internal shocks within microquasars jets, could produce TeV gamma-rays and neutrinos fluxes through photomeson interaction on ambient X-ray radiation or with cold protons of the donor stellar wind.

3. HIGH-ENERGY NEUTRINO ASTRONOMY

AGN, the most luminous persistent object observed in the sky, are galaxies with a very bright core of emission embedded in their centre. The standard scenario for AGNs assumes the presence of a very massive central black hole ($10^6 - 10^9$ solar masses) swallowing huge quantities of surrounding matter from an accretion disk and two relativistic jets where particles can be accelerated to ultra-high energies via Fermi acceleration in a series of consecutive shock fronts, leading to a very concentrated energy output from a relatively small volume. According to some models (43), the energy rate generated by the brightest AGNs can be greater than 10^{47} erg/sec. Blazars are a subclass of AGNs with the emitting jet pointing into direction of the Earth and are the brightest objects in the gamma-rays sky above 100 GeV. It is thus natural to consider them as a promising sources of high-energy neutrinos but their contribution to the diffuse flux of $\text{HE}\nu$ is not expected to be greater than 25% (44).

GRBs are among the most mysterious and violent phenomena ever observed in the Universe. GRBs are transient sources with emission in hard-X-ray and soft-gamma photons lasting from millisecond to several hundreds of seconds and a late afterglow in IR, radio and optical band. In this short time interval each GRB releases a huge total energy ($\geq 10^{51}$ erg/s). However, in spite of a large numbers of GBRs observed since their discovery, the nature of these objects remains mysterious to a large extent. The bulk of the emission features indicate a non-thermal process, driven by a catastrophic event involving charged particle acceleration and the conversion of huge quantities of matter into energy. The most widely accepted model that describes the actual emission of radiation of the GRB is the fireball model in combination with the internal-external shock model (45, 46). Their contribution to the diffuse flux can be no more than few percents (47).

As discussed previously, the interaction of protons having $E > 10^{19}$ eV with the CMB produces a cut-off in the cosmic ray energy spectrum called GZK cut-off. A natural consequence will be the existence of a diffuse flux of ultra-high energy cosmogenic neutrinos coming from the decay of the Δ -resonance via the channel of charged pion production. The diffuse flux of GZK neutrinos is considered, to some extent, a “guaranteed” neutrino flux with an energy spectrum that can range from approximately $E \sim 10^{16}$ eV up to $E \sim 10^{21}$ eV. The shape and the strength of the neutrino flux depend on several factors such as the primary UHECR flux spectral index and composition.

To date, no astrophysical object has been conclusively identified as a source of high-energy neutrinos. This motivates the complementary search for a diffuse flux of astrophysical neutrinos. While individual neutrino sources might be too weak to be detectable with current instruments, they would still contribute to a collective astrophysical neutrino flux. Therefore a cumulative flux, composed of the integrated flux of all neutrino sources, could be detected even if the individual source fluxes are below the detection threshold, as long as the source population is large. Furthermore, the prediction of the diffuse neutrino flux from unresolved astrophysical sources is based on cosmic ray (CR) and gamma-ray observations. Thus connection between cosmic-rays and astrophysical neutrinos permits an estimation of an upper bound for such a diffuse neutrino flux.

3.3 Models and Limits

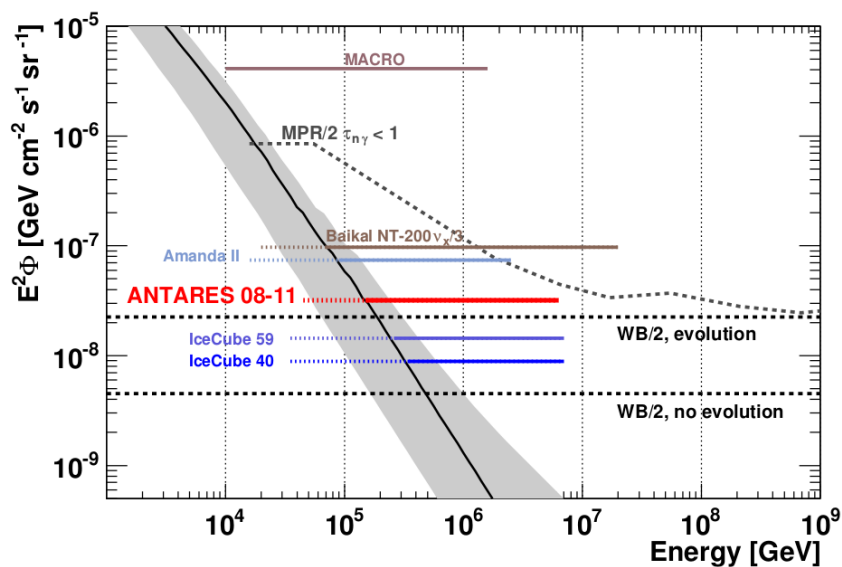


Figure 3.3: Experimental upper limits on an astrophysical ν_μ flux with an E^{-2} spectrum from different experiments. The MACRO limit (48) refers to $\nu_\mu + \bar{\nu}_\mu$ while the Baikal limit (49) refers to neutrinos and anti-neutrinos of all flavors and is divided by 3. For reference the Waxman-Bahcall (50) and the Mannheim-Protheroe-Rachen (51) upper bounds for transparent sources are also shown. They are divided by two, to take into account neutrino oscillations. The grey band represents the expected variation of the atmospheric ν_μ flux.

Both electrons (leptonic models) and protons or nuclei (hadronic models) can be accelerated in astrophysical processes. In the framework of hadronic models the

3. HIGH-ENERGY NEUTRINO ASTRONOMY

energy escaping from the sources is distributed between CRs, gamma-rays and neutrinos. Upper bounds for the neutrino diffuse flux are derived from the observation of the diffuse fluxes of gamma-rays and ultra high-energy CRs, taking into account the production kinematics, the opacity of the source to neutrons and the effect of propagation in the Universe.

3.3.1 Waxman-Bahcall

As mentioned previously, $\Phi \propto E^{-2}$ is a generic spectrum predicted by first order Fermi acceleration. A number of theories have been developed based on this spectral shape. A common benchmark in neutrino astronomy is the Waxman-Bahcall (WB) upper bound (50), which assumes that cosmological sources of protons have a E^{-2} injection spectrum. The upper bound was determined assuming that the energy production rate of protons is

$$E_{CR}^2 \frac{d\dot{N}_{CR}}{dE_{CR}} \approx 10^{44} \text{ erg Mpc}^{-3} \text{ yr}^{-1} \quad (3.7)$$

To derive the maximum value of the neutrino flux, it was assumed that protons do not lose any energy before escaping the source.

The WB upper bound uses the CR observations at $E_{CR} \sim 10^{19}$ eV ($E_{CR}^2 \Phi_{CR} \sim 10^{-8}$ GeV cm⁻² s⁻¹ sr⁻¹) to constrain the diffuse flux per neutrino flavour (here and in the following the symbol ν represents the sum of ν_μ plus $\bar{\nu}_\mu$):

$$E_\nu^2 \Phi_\nu < \frac{4.5}{2} \times 10^{-8} \text{ GeV cm}^{-2} \text{ sr}^{-1} \text{ s}^{-1} \quad (3.8)$$

Approximately half of the muon neutrinos are expected to oscillate into other flavors so the factor 1/2 is added to take that into account. As shown in Figure 3.3, this limit has been discovered and improved by the IceCube experiment.

3.3.2 Mannheim-Protheroe-Rachen

Another relevant prediction is the Mannheim-Protheroe-Rachen (MPR) upper bound (51), which is derived using as constraints the observed CR fluxes over the range from 10^5 to 10^9 GeV and gamma-ray diffuse fluxes. Mannheim, Protheroe and Rachen proposed several models for the astrophysical neutrino flux.

They placed an upper bound on the neutrino flux for optically thick sources in which neutrons cannot escape ($\tau_{n\gamma} \gg 1$). The said neutrons were produced in previous hadronic interactions in the source, such as $p + \gamma \rightarrow \pi^+ + n$. In the case of sources opaque to neutrons, the MPR upper bound follows an E^{-2} spectrum and arrive at a higher flux limit of $2 \times 10^{-6} \text{ GeV cm}^{-2} \text{ sr}^{-1} \text{ s}^{-1}$. The prediction is normalized to measurements of the extragalactic gamma-ray background.

In the case of sources transparent to neutrons, instead of using the E^{-2} spectrum assumed by Waxman and Bahcall, they assumed an extragalactic cosmic ray injection spectrum that is consistent with the observable cosmic ray flux

$$N_{p,obs}(E) = 0.8 \times (E/GeV)^{-2.75} \text{ cm}^{-2} \text{ s}^{-1} \text{ sr}^{-1} \text{ GeV}^{-1} \quad (3.9)$$

Since the cosmic-ray and gamma-ray outputs are correlated, the cosmic-ray normalizations also had to agree with the observed gamma-ray background.

MPR also projected an upper bound on the flux of neutrinos from AGN jets. They followed the same procedure just described to normalize the neutrino spectrum to the observed cosmic-ray flux. For this calculation, they used the same generic cosmic-ray and neutrino production spectra as were used in the determination of the thin sources upper bound.

3.3.3 IceCube Results and Flux Assumptions

IceCube, the first cubic-kilometer neutrino detector ever built, is also the first telescope to observe a flux of cosmic neutrinos. Before the IceCube detector commenced full operation of the completed array in 2011, constraints were placed for an upper limit on the astrophysical neutrino diffuse flux (52, 53, 54, 55). In the summer of 2013, the two first neutrino-induced PeV events were recorded (56). These fully contained particle showers were discovered using data collected between May 2010 and May 2012, and were rejected to be part of an atmospheric background-only hypothesis with a 2.8σ probability.

In December 2013, the IceCube Collaboration had reported the observation of an additional 26 neutrino events with energies above 30 TeV and predominantly originating from the Southern hemisphere (57). These events had flavors, directions

3. HIGH-ENERGY NEUTRINO ASTRONOMY

and energies inconsistent with those expected from the atmospheric muon and neutrino backgrounds and instead had properties consistent with generic predictions for an additional component of extraterrestrial origin. Thus these 28 events rejected to emerge from a purely atmospheric background as they corresponded to a 4.1σ excess.

In this analysis, for the search to have approximately equal sensitivity to neutrinos of all flavors and from all directions, neutrinos with interaction vertices well contained within the detector volume were selected in the two-year dataset (May 2010 to May 2012). Of these 28 events, only 7 events show a clearly identifiable track-like signature, the other 21 events have the typical spherical shape of shower-like events. A neutrino flux produced in extraterrestrial sources would be heavily biased towards shower-like events because neutrino oscillations over astronomical baselines tend to equalize neutrino flavors and an equal-flavor E^{-2} neutrino flux would be expected to produce only 1/5 track-like events.

A search for spatial clustering, indicating possible neutrino sources, was performed but the poor angular resolution for shower-like events and wide distribution of the events did not allow the identification of any sources. In addition to the clustering of events in space, a search for clustering of events in time was performed, as many sources are expected to produce neutrinos in bursts. When using all events, neither of these analyses yielded significant results.

In early 2014, the IceCube Collaboration reported on a search for a diffuse astrophysical neutrino signal, looking at high-energy neutrino-induced upward-going muon tracks within the detector (58). The data was taken between May 2009 and May 2010, when the detector was running in its 59-string configuration. A global likelihood fit was performed on the reconstructed energies and directions of observed events. The search found a high-energy neutrino excess of 1.8σ compared to the background scenario of a pure conventional atmospheric model. Figure 3.4 compares the upper limit of that analysis with theoretical flux predictions and limits from other experiments.

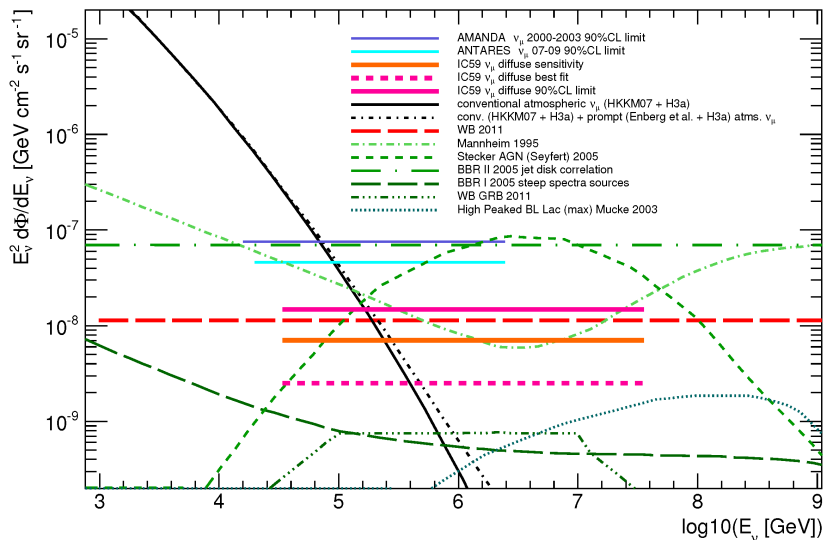


Figure 3.4: Limit of a $(\nu_\mu + \bar{\nu}_\mu)$ astrophysical E^{-2} flux from (58) in comparison to theoretical flux predictions and limits from other experiments. The black line shows the expected atmospheric neutrino flux with and without a prompt component (both without the modification of the knee feature). The red dashed line marks the Waxman-Bahcall upper bound (50, 59). The green dashed lines represent various model predictions for astrophysical neutrino fluxes. Horizontal lines show limits and sensitivities from different experiments (54, 60, 61). The pink solid line is the 90% CL upper limit of (58), the orange solid line shows its sensitivity.

Later in 2014, another analysis was performed using a third year (2012-2013) of data (62). The data are consistent with expectations for equal fluxes of all three neutrino flavors and with isotropic arrival directions. The combined 3-year dataset contained a total of 36 neutrino events and rejected a purely atmospheric explanation at 5.7σ . Once more, a search for neutrino source clustering or correlations was performed, yielding no statistically significant results. As in the previous analysis, the strongest clustering was near the galactic center but no other observations of this location gave any evidence for a source and no events were strongly correlated with this region. Later observations were carried out in order to search for neutrino source clustering with more years of data (63, 64, 65), but found no evidence of spatial clustering (see Figure 3.5). The latest results (65) included 103 events (with 60 events with energies above 60 TeV), updates to calibration and ice optical properties, and changes to the right ascension, declination and energy. Leading to a significant improvement to the systematics and angular resolution.

3. HIGH-ENERGY NEUTRINO ASTRONOMY

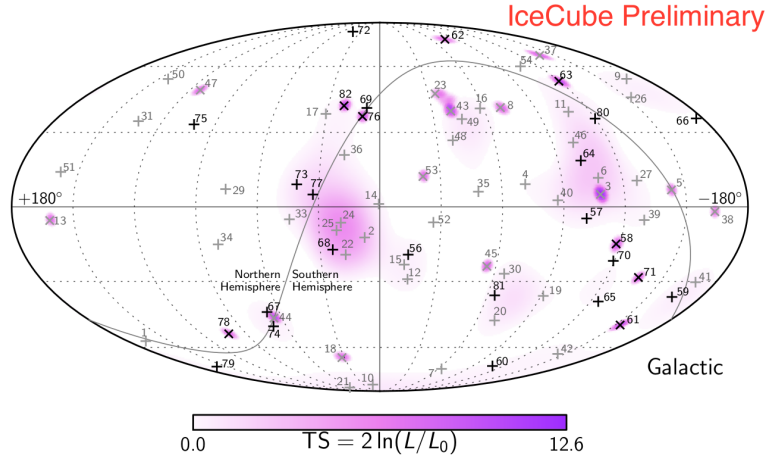


Figure 3.5: Arrival directions of the events in galactic coordinates. Shower-like events are marked with a + and those containing track-like events with a \times . The new events from (64) are shown in black while the grey events come from previous studies (62, 63). Colors show the test statistics (TS) for the point-source test at each location. No significant clustering was observed.

In 2015, a study presented the results of a search for neutrino interactions inside the IceCube’s instrumented volume with two years of data (taken from 2010 to 2012), lowering the energy threshold for neutrinos from the Southern sky below 10 TeV for the first time (66). From these data, containing 283 shower-like events and 105 track-like events, an $E^{-2.46}$ spectrum was derived. Of those 388 events, 106 deposited more than 10 TeV at the shower vertex and only 9 deposited more than 100 TeV, therefore this new constraint on the spectral index was needed to explain the low energy data. Under this softer $E^{-2.46}$ spectral index, the E^{-2} hypothesis was rejected with 99% confidence. But if the E^{-2} spectral index was forced, the astrophysical signal flux obtained was consistent with the previously mentioned studies.

That same year, another study was carried out to analyze the flavor composition of an astrophysical flux down to 35 TeV, by classifying events as showers or tracks (67). Shower-like events contain less atmospheric background events and thus a shower-biased sample was obtained, containing 129 shower-like events and 8 track-like events collected from three years of data (May 2010 to May 2013). Results consistent with the $\nu_e : \nu_\mu : \nu_\tau = 1 : 1 : 1$ flavor ratio at Earth (expected for a 1:2:0 source composition) were obtained. At the same time, a track-like composition of 0:1:0 at Earth was excluded at 3.3σ and a shower-like composition of 1:0:0 at Earth was also excluded at 2.3σ .

Furthermore, in 2015, a combined analysis was performed using the maximum-likelihood method and six years worth of IceCube data (68). The results from six different searches were combined with event samples of shower-like, track-like and hybrid events. The data was fit in up to three observables, which were the energy, the zenith angle and the event topology. New data was later added to the this work (69). Both these analyses disfavored an unbroken power law with a spectral index of -2.

Since the IceCube collaboration's major discovery in 2013, more than 10 astrophysical neutrino events are observed yearly on the energy range from a few tens of TeV to PeV scale and from different complementary detection channels. Many studies based on an enlarged statistics and improved analysis methods have been presented, unambiguously proving that the cosmic neutrino flux has been observed. The underlying data characteristics in these studies are shown in Table 3.1 and the consequent astrophysical neutrino diffuse fluxes are summarized in Table 3.2. Typically, studies based on only ν_μ -induced events access energies above 100 TeV because of more abundant atmospheric background while analyses including ν_e and ν_τ interactions have lower energy threshold.

Assuming an astrophysical flux arriving isotropically from all directions and that can be described by a simple power law of the form

$$\Phi_\nu = \phi \times 10^{-18} \left(\frac{E}{10^5 \text{ GeV}} \right)^{-\gamma} \quad (3.10)$$

Φ_ν denotes the diffuse neutrino flux, ϕ its value at 100 TeV (10^5 GeV), and γ its spectral index. Both Φ_ν and ϕ are in units of $\text{GeV}^{-1} \text{ cm}^{-2} \text{ sr}^{-1} \text{ s}^{-1}$.

In addition to the baseline astrophysical flux model, a test hypothesis can implement a spectral cutoff as an exponential factor in the flux model

$$\Phi_\nu = \phi \times 10^{-18} \left(\frac{E}{10^5 \text{ GeV}} \right)^{-\gamma} \times \exp \left(-\frac{E}{E_{cut}} \right) \quad (3.11)$$

This cutoff is typically used in the case of an E^{-2} spectrum and will be in units of PeV.

3. HIGH-ENERGY NEUTRINO ASTRONOMY

Reference	Detector Configuration	Days of Data	Selected Events	Energy Range
(52)	IC-22	242.1	0	30 PeV to 3 EeV
(53)	IC-40	333.5	0	2 PeV to 6.3 EeV
(54)	IC-40	375.5	0	35 TeV to 7 PeV
(56, 70)	IC-79 + IC-86	615.9	2	1.04 ± 0.16 PeV and 1.14 ± 0.17 PeV
(57)	IC-79 + IC-86	662	28	30 TeV to 1.2 PeV
(58)	IC-59	348.1	—	—
(55)	IC-40	367.1	—	25 TeV to 5 PeV
(62)	IC-79 + IC-86	988	36	30 TeV to 2 PeV
(66)	IC-79 + IC-86	641	388	25 TeV to 1.4 PeV
(67)	IC-79 + IC-86	974	137	35 TeV to 1.9 PeV
(71)	IC-79 + IC-86	659.5	—	330 TeV to 1.4 PeV
(68)	IC-40 + IC-59 + IC-79 + IC-86	2008 to 2013	—	25 TeV to 2.8 PeV
(72)	IC-59 + IC-79 + IC-86	2060	—	194 TeV to 7.8 PeV
(73)	IC-59 + IC-79 + IC-86	May 2009 to May 2015	—	170 TeV to 3.8 PeV
(74)	IC-59 + IC-79 + IC-86	May 2009 to May 2017	—	119 TeV to 4.8 PeV

Table 3.1

3.3 Models and Limits

Reference	E^{-2} Best-Fit ϕ	E^{-2} Cutoff	Best-Fit Spectral Index	Best-Fit ϕ	Topology
(52)	140 [upper-limit]	None	—	—	
(53)	3.6 [upper-limit]	~ 2	—	—	
(54)	0.89 [upper-limit]	None	—	—	
(56, 70)	2.5 [upper-limit]	~ 2	—	—	Showers
(57)	1.2 ± 0.4	~ 2	2.2 ± 0.4	—	Tracks and Showers
(58)	0.25 [best-fit] and 1.44 [upper-limit]	None	—	—	Tracks
(55)	7.46 [upper-limit]	None	—	—	Showers
(62)	0.95 ± 0.3	None	—	—	Tracks and Showers
(66)	1.22 ± 0.5	None	2.46 ± 0.12	$2.06^{+0.35}_{-0.26}$	Tracks and Showers
(67)	—	—	2.6 ± 0.15	2.3 ± 0.4	Tracks and Showers
(71)	$0.99^{+0.39}_{-0.34}$	None	2.2 ± 0.2	$1.7^{+0.6}_{-0.8}$	Tracks
(68)	$5.2^{+1.9}_{-1.5}$	$1.6^{+1.5}_{-0.7}$	2.5 ± 0.09	$6.7^{+1.1}_{-1.2}$	Tracks and Showers
(72)	—	—	2.13 ± 0.13	$0.9^{+0.30}_{-0.27}$	Tracks
(73)	—	—	1.91 ± 0.2	$0.66^{+0.4}_{-0.3}$	Tracks
(74)	—	—	2.19 ± 0.10	$1.1^{+0.26}_{-0.23}$	Tracks

Table 3.2

Going back to the analysis presented in (57), the data were well described by a E^{-2} spectrum with a cutoff at 3 PeV. This cutoff was indicated by a lack of sufficient IceCube events in the PeV range, as a flux at that level would have been expected to generate an additional 3-6 events in the 2-10 PeV range. The per-flavor flux is then

$$\Phi_{\text{IC2}}(E_\nu) = 1.2 \times 10^{-8} \left(\frac{E_\nu}{\text{GeV}} \right)^{-2} \cdot \exp \left(-\frac{E_\nu}{3\text{PeV}} \right) [\text{GeV}^{-1}\text{cm}^{-2}\text{s}^{-1}\text{sr}^{-1}] \quad (3.12)$$

From the IceCube analysis (66), a diffuse flux with an $\sim E^{-2.46}$ spectrum and without any cutoff is considered. For this steeper spectrum a cutoff is not required, as there was no evidence indicating that a high-energy cutoff was necessary to describe

3. HIGH-ENERGY NEUTRINO ASTRONOMY

the IceCube data; nevertheless it is still used in some references. The following flux is used to check the robustness of our results with respect to the various parametrisations that have been proposed

$$\Phi_{\text{IC}2.46 \text{ w/o CO}}(E_\nu) = 4.11 \times 10^{-6} \left(\frac{E_\nu}{\text{GeV}} \right)^{-2.46} [\text{GeV}^{-1} \text{cm}^{-2} \text{s}^{-1} \text{sr}^{-1}] \quad (3.13)$$

For the benchmark model, a cutoff is slightly preferred. When fixing the spectral index for an unbroken power law (typically with a harder spectrum), the slight preference for an exponential cutoff disappears. Nevertheless, for later comparison, the shape of the $\sim E^{-2.46}$ spectra with cutoff (w/ CO) will straightforwardly implement the same cutoff as that of the E^{-2} spectra

$$\Phi_{\text{IC}2.46 \text{ w/ CO}}(E_\nu) = 4.11 \times 10^{-6} \left(\frac{E_\nu}{\text{GeV}} \right)^{-2.46} \cdot \exp\left(-\frac{E_\nu}{3\text{PeV}}\right) [\text{GeV}^{-1} \text{cm}^{-2} \text{s}^{-1} \text{sr}^{-1}] \quad (3.14)$$

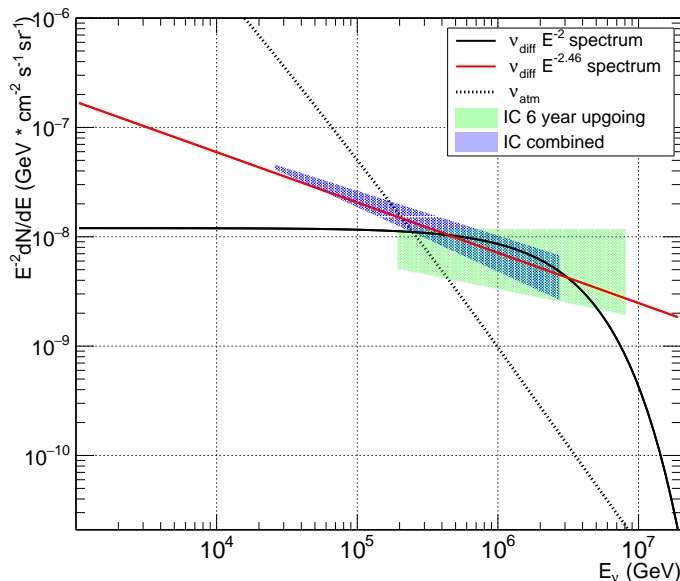


Figure 3.6: Diffuse neutrino spectra adopted in this work: the black line describes Equation 3.12 and the red line describes Equation 3.13. The blue and green shaded areas correspond to the reported uncertainties for the best-fit single power law models of papers (68) and (72) respectively.

These fluxes were also used in the KM3NeT Letter of Intent (17). Despite these choices having been made before the recent IceCube analyses, the spectra are well in agreement with IceCube fluxes within the reported uncertainties. In fact, in Figure

3.6 the recent results from papers (68, 72) and their uncertainties are displayed and compared to the chosen neutrino diffuse fluxes in Equations 3.12 and 3.13.

In this work, the search strategy is to identify upward-going muons, which unambiguously indicates neutrino reactions since only neutrinos can traverse the Earth without being absorbed. A neutrino telescope in the Mediterranean Sea is ideal for this purpose, since most of the potential Galactic sources are in the Southern sky. Yet the detection of high-energy cosmic neutrinos is not background free; showers induced by interactions of CRs with the Earth's atmosphere give rise to atmospheric muons and atmospheric neutrinos. Atmospheric neutrinos that have traversed the Earth and have been detected in the neutrino telescope, are an irreducible background for the study of cosmic neutrinos. As the spectrum of cosmic neutrinos is expected to be harder ($\propto E_\nu^{-2}$) than that of atmospheric neutrinos, a way to distinguish the ν_μ cosmic diffuse flux is to search for an excess of high-energy events in the measured energy spectrum.

3.4 Atmospheric Neutrinos

Neutrinos are abundantly produced in the Earth's atmosphere by hadronic and muonic decays following the interaction of cosmic rays with the atomic nuclei. In fact, hadronic interactions produce large numbers of mesons, primarily pions and kaons, and neutrinos are created in the decay of these charged mesons. Neutrinos also originate from the subsequent decay of muons (as previously mentioned in Equations 3.5 and 3.6). The decay chain from mesons is thus:

$$p/n + N \rightarrow \pi^\pm / K^\pm + \dots \quad (3.15)$$

$$\hookrightarrow \mu^\pm + \nu_\mu(\bar{\nu}_\mu) \quad (3.16)$$

$$\hookrightarrow e^\pm + \bar{\nu}_\mu + \nu_e$$

Studying the final products of these reactions one expects that there are about twice as many muon neutrinos as there are electron neutrinos produced in the atmosphere:

$$\frac{\nu_\mu + \bar{\nu}_\mu}{\nu_e + \bar{\nu}_e} \sim 2 \quad (3.17)$$

This expectation holds at low energies but additional effects have to be taken into account at higher energies.

3. HIGH-ENERGY NEUTRINO ASTRONOMY

Although high-energy cosmic rays arrive almost isotropically, the zenith angle dependence of high-energy atmospheric neutrino production is complicated by the direction of the shower through the atmosphere. Muons with energy of several GeV and above reach the ground before decaying, so the ν_e/ν_μ ratio decreases with increasing energy. The resulting steepening of the ν_e spectrum occurs at lower energy near the vertical direction and at higher energy near the horizon because of the longer decay path for the parent muons with large zenith angle. The component of the ν_μ flux from muon decay behaves the same way. These features of the neutrino flux are illustrated in Figure 3.7. The left panel shows the neutrino fluxes calculated in the artificial case of no geomagnetic cutoff and shown as a function of cosine of the zenith angle. The right panel shows the key ratio of electron neutrinos to muon neutrinos from several calculations averaged over all directions for the specific location of Super-Kamiokande.

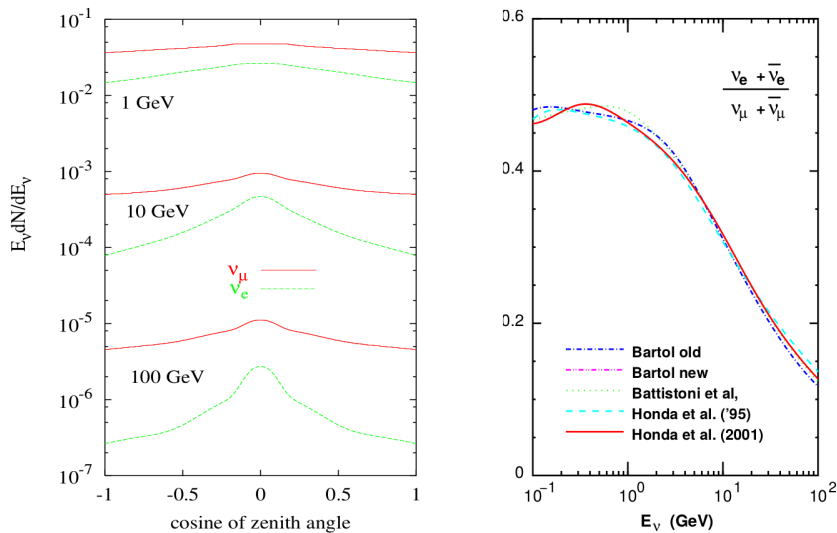


Figure 3.7: Left panel: Zenith-angle dependence of $\nu + \bar{\nu}$ calculated in the absence of a geomagnetic field. Right panel: Ratio of $(\nu_e + \bar{\nu}_e)/(\nu_\mu + \bar{\nu}_\mu)$ as calculated in several papers including the geomagnetic field for the location of Super-Kamiokande (75).

Neutrinos directly from muon decay are important up to a few GeV, a broad peak can be observed around 0.1 GeV ($\sim 1 \text{ cm}^{-2} \text{ s}^{-1}$). Pions and kaons that decay in-flight are the primary source of atmospheric muon neutrinos from a few GeV up to about 100 TeV. With rest-frame lifetimes on the order of 10^{-8} s, these mesons often lose some of their energy in collisions prior to decaying, leading to lower energy neutrinos among the decay products. Therefore, at energies higher than 1 TeV, the spectral slope of

this “conventional” atmospheric neutrino flux (76, 77, 78) asymptotically becomes one power steeper than the spectrum of the parent cosmic-ray, hence adopting a power law with a spectral index of typically $E^{-3.7}$. The intensity of the conventional atmospheric neutrinos is well-measured up to 6 TeV for ν_e and up to 400 TeV for ν_μ (79, 80), since at higher energies the poor knowledge of the composition of the cosmic-ray flux causes significant uncertainties on the intensity.

Assuming γ_p as the spectral index of the cosmic ray spectrum, the conventional atmospheric neutrino flux can be expressed as

$$\frac{d\Phi_\nu}{dE_\nu d\Omega}(E_\nu, \theta) = A_\nu E_\nu^{-\gamma_p} \left(\frac{1}{1 + \frac{aE_\nu}{\epsilon_\pi} \cos \theta} + \frac{B}{1 + \frac{bE_\nu}{\epsilon_K} \cos \theta} \right) [\text{cm}^{-2}\text{s}^{-1}\text{sr}^{-1}\text{GeV}^{-1}] \quad (3.18)$$

Here, the scale factor A_ν , the balance factor B (which depends on the ratio of muons produced by kaons and pions) and the a, b coefficients are parameters which can be derived from Monte Carlo computer simulations, numerical approximations or from experimental data. The quantity ϵ_i (the characteristic decay constant) corresponds to the energy at which the hadron interaction and decay lengths are equal. For pions and kaons, $\epsilon_\pi = 115$ GeV and $\epsilon_K = 850$ GeV respectively.

Theoretical uncertainties in predictions for the conventional flux are dominated by uncertainties in the normalization and spectral distribution of the cosmic-ray flux. Additional uncertainties include the ratio of pions to kaons produced by cosmic-ray interactions, which affects the zenith angle distribution, particularly near the horizon. The energy spectrum of nearly horizontal conventional atmospheric neutrinos is flatter than that of almost vertical neutrinos because pions and kaons in inclined showers spend more time in the tenuous atmosphere where they are more likely to decay before losing energy in collisions. In the left panel of Figure 3.8 the atmospheric neutrino spectra calculated by different groups are shown (Bartol (76, 77), Fluka (81) and Honda (78)).

3. HIGH-ENERGY NEUTRINO ASTRONOMY

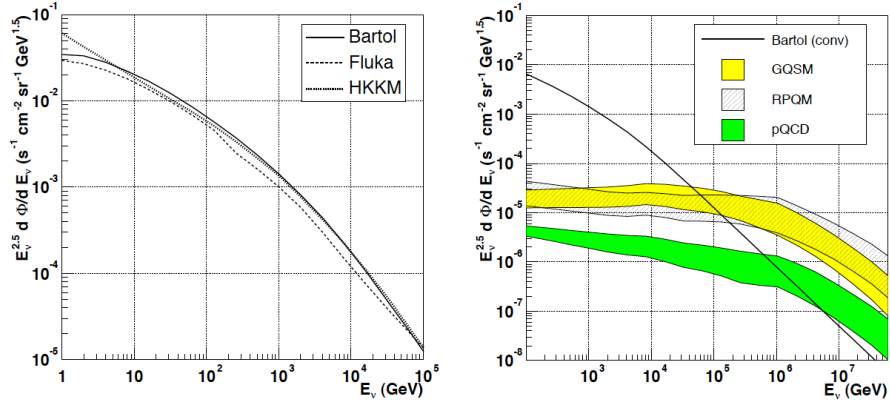


Figure 3.8: Models of atmospheric neutrino fluxes. Left panel: three models for the conventional atmospheric neutrino flux. Right panel: The Bartol model and three models for prompt neutrino fluxes taken from (82). The results have been integrated over all directions.

At sufficiently high energies, another production mechanism for atmospheric neutrinos will be through the decay of heavier charmed mesons and baryons. These hadrons have such short rest-frame lifetimes ($\sim 10^{-12}$ s) that they decay almost immediately, before interacting and losing energy in collisions. Hence, the spectrum of the so-called “prompt” atmospheric neutrino flux (82) follows more closely the parent cosmic-ray spectrum and is about one power softer than the conventional atmospheric neutrino flux at high energy. The calculation of the prompt atmospheric neutrino flux requires the knowledge of the differential cross-sections for $gg \rightarrow c\bar{c}$ and $q\bar{q}$ -fusion. The cross-sections for their production are small and therefore their contribution is only relevant at higher energies.

Although it has yet to be detected, the prompt flux is expected to be important above about 100 TeV. The neutrinos from decay of charmed hadrons continue with the same spectral index as the primary cosmic-ray spectrum up to this energy, while the neutrinos from decay of pions and kaons become steeper at much lower energy. Moreover, the prompt atmospheric neutrino contribution is isotropic up to $\sim 10^7$ GeV, which is close to the critical energy for charm decay, while the contribution from pions and kaons is proportional to $\sec \theta$ for $E_\nu \gg 1$ TeV, and reaches a maximum at the horizon. In Figure 3.9, the prompt and conventional $\nu_\mu + \bar{\nu}_\mu$ fluxes in the vertical and horizontal direction are shown, deducing that the vertical direction is the optimal direction for studying the prompt fluxes. In the horizontal direction

the prompt flux does not become larger than the conventional flux until very large energies 10^7 GeV, where the actual number of neutrinos is quite low.

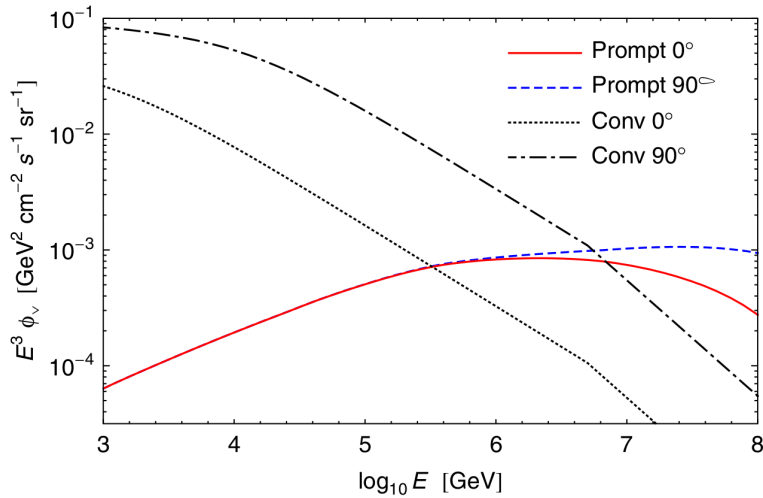


Figure 3.9: Dependence on zenith angle of prompt and conventional $\nu_\mu + \bar{\nu}_\mu$ fluxes. The solid and dashed lines are the Enberg (83) prompt fluxes with fragmentation in the vertical and horizontal directions, respectively. The dotted and dash-dotted lines are the Gaisser-Honda (75) conventional fluxes in the vertical and horizontal directions.

Just like the conventional flux, the uncertainties in the normalization and spectral distribution of the cosmic-ray flux impact the predictions for the prompt flux. Additional sources of uncertainty for the prompt flux include charm production cross-sections and fragmentation functions. In the right panel of 3.8, the range of allowed prompt neutrino fluxes is shown for each of the charm production models. For each model, the parametrization used to represent the flux of primary cosmic-rays are varied, yielding a range of fluxes. In contrast to the models for the conventional neutrino flux, the uncertainty on the prompt flux can be very large. In this work, a more recent model for the prompt atmospheric neutrino is used: the Enberg model (83), as well the the Honda model in order to describe the conventional atmospheric neutrinos.

3. HIGH-ENERGY NEUTRINO ASTRONOMY

Chapter 4

SIMULATION AND RECONSTRUCTION TOOLS

Monte Carlo simulations are necessary to understand the detector response and to interpret the data recorded by a detector. Especially during the early phases of KM3NeT, Monte Carlo simulations were the only way to evaluate the detector's physics potential and to properly assess its performance. Some of the simulation tools used in this thesis have been produced by the ANTARES Collaboration and adapted to the KM3NeT geometry and DOM structure. Other simulation tools were recently developed to suit the needs of the km³-scale detector.

The software provides a complete simulation of the detector geometry, the incident particles, and the detector's response. Two packages generate the primary particles, whether they are neutrinos or atmospheric muons. Intermediate packages replicate the light generation and propagation in water; and when dealing with neutrinos, they must also simulate beforehand their interaction in the medium and the propagation of the resulting secondary particles. The depth and the optical water properties measured at the Sicilian Capo Passero site have been used (9). Background light due to the presence of ⁴⁰K in salt water and bioluminescence has been simulated by adding an uncorrelated hit rate in each PMT and a time-correlated hit rate between PMTs of the same DOM due to the genuine coincidences from ⁴⁰K decays.

Afterward, a track reconstruction algorithm is used to estimate muon (and consequently neutrino) directions using the information recorded by the detector. The reconstruction data is supplied by the PMT spatial positions and the Cherenkov photon arrival times, thus emphasizing the importance of their accurate measurement.

4. SIMULATION AND RECONSTRUCTION TOOLS

This, together with precise knowledge in real time of the positions and orientations of the PMTs, are mandatory to reconstruct the direction of the neutrinos with a small angular resolution.

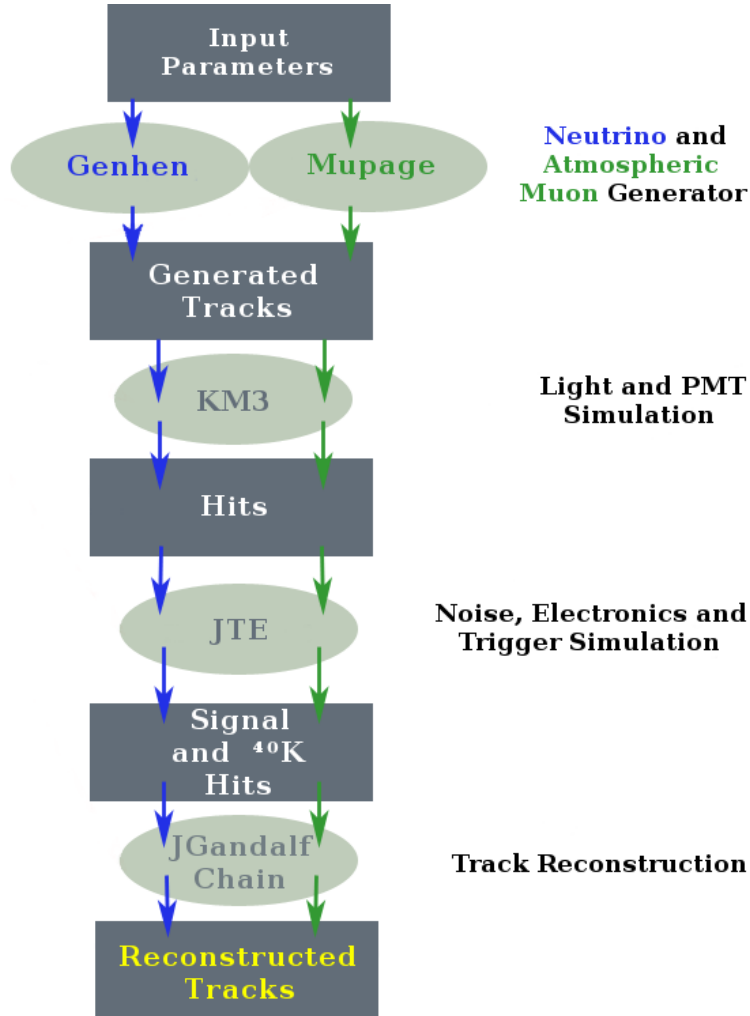


Figure 4.1: Scheme of the codes used to simulate and reconstruct events in KM3NeT.

The codes are written in C++ and FORTRAN. The atmospheric and cosmic neutrinos are generated through GENHEN (GENERATOR of High Energy Neutrinos) while atmospheric muons are generated with MUPAGE. The muon propagation through the detector and the generation of the hits due to Cherenkov photon is provided by KM3. The other secondary particles generated at the interaction vertex and the consequent generation of hits is also performed by KM3. The noise hits due to ⁴⁰K and bioluminescent background are added using JTriggerEfficiency (JTE), which also carries out PMT simulation and triggering. Finally, the track is reconstructed using JGandalf. All these steps are illustrated in the scheme of Figure 4.1.

4.1 Simulation Tools

4.1.1 Detector Geometry

An ASCII file with complete information of the detector geometry is created. In this file, the absolute position of the detector are reported in UTM (Universal Transverse Mercator) coordinates, together with the PMTs' position and orientation. The detector used to simulate Phase-1 is composed of 24 strings, each string is about 700 meters in height and hosts 18 DOMs. There are about 95 meters between each string and the DOMs are 36 meters apart in the vertical direction, starting about 80 meters from the sea floor. Each DOM contains 31 PMTs making a total of 13392 PMTs. The detector is located about 100 km offshore Capo Passero ($36^{\circ} 16' N$ $16^{\circ} 06' E$) at a depth of 3500 m. In Figure 4.3, the origin of the detector is its barycenter.

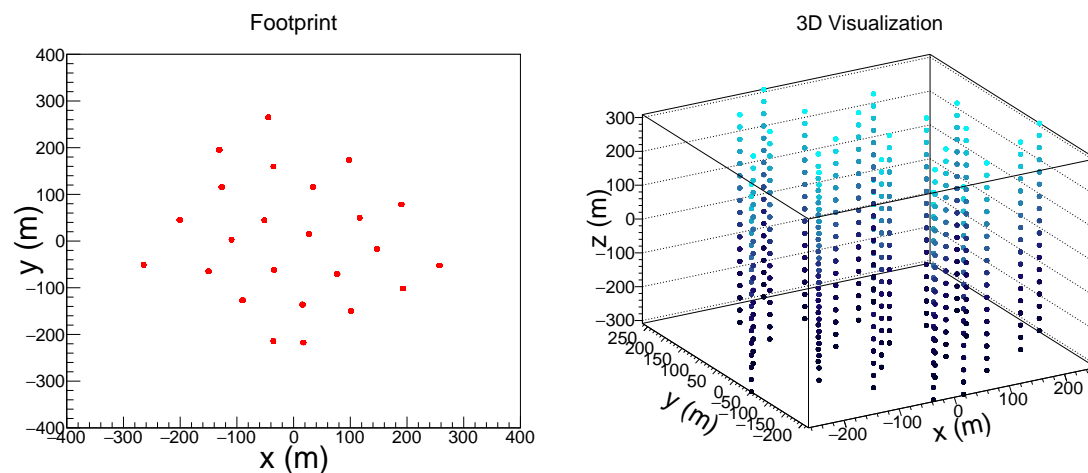


Figure 4.2: The KM3NeT/ARCA Phase-1 detector with 24 strings. Left panel: Footprint. Right panel: 3-dimensional visualization.

4.1.2 Generation of Neutrino Events

GENHEN

The GENHEN code (84) is the first step of the simulation chain for Monte Carlo production of events. It is written in FORTRAN and is used to generate and propagate neutrinos of all three flavors in the proximity of the detector. This program includes a complete simulation of incident neutrinos, their propagation through the Earth, their interactions in the medium and the resulting secondary particles. The

4. SIMULATION AND RECONSTRUCTION TOOLS

particles resulting from the incident neutrino interactions are propagated to the detector and their energy loss is calculated in the process. This package is suitable for VHE and UHE generation of neutrinos up to an energy of 10^9 GeV. In this thesis, the generated neutrino energie will range from 10^2 GeV to 10^8 GeV.

This package also includes neutrino oscillations, which modify the flavor content of astrophysical neutrino beams in the path from sources to the Earth. Moreover, the Glashow resonance (85) (a resonant W production from the reaction of $\bar{\nu}_e$ with electrons in the atmosphere) and the propagation through the Earth were implemented. Secondary τ leptons, which have a life time of 2.9×10^{-13} s and thus typically travel only very short distances before decaying, can also be propagated and their decay is simulated using TAUOLA (86). Hence, the complete regeneration chain of $\nu_\tau \rightarrow \tau \rightarrow \nu_\tau \dots$ including τ energy losses, can be simulated.

Since the neutrino interaction cross-section is very small, simulating all the neutrino events would be disadvantageous in terms in CPU-time. Therefore, the code generates only neutrinos that interact inside or near the detector and are able to produce detectable secondary particles. A cylindrical volume, fixed in size and position, containing the instrumented volume of the detector is defined as the so-called can. The can represents the Cherenkov-sensitive volume, it is a “safety zone” around the detector such that photons produced beyond it have neglectable probability to reach a PMT and produce signals. Here the light absorption length measured at the Capo Passero site $\lambda_{abs} = 70$ m is applied and the scaling factor extends the instrumentation volume by three times λ_{abs} .

GENHEN does not perform a full simulation of neutrino fluxes, instead it generates interacting neutrinos inside a generation volume. The generation volume (V_{gen}) depends on the maximum neutrino energy (E_{max}) of the generated spectrum (and on neutrino flavour and interaction type), on the corresponding maximum muon range in water R_w and in rock R_r and on the angular range of the simulation. For a 360° simulation, the generation volume will be a cylinder surpassing the can by R_r in height for up-going events or $R_w \cos \theta_{max}$ for down-going events, and having R_w as radius.

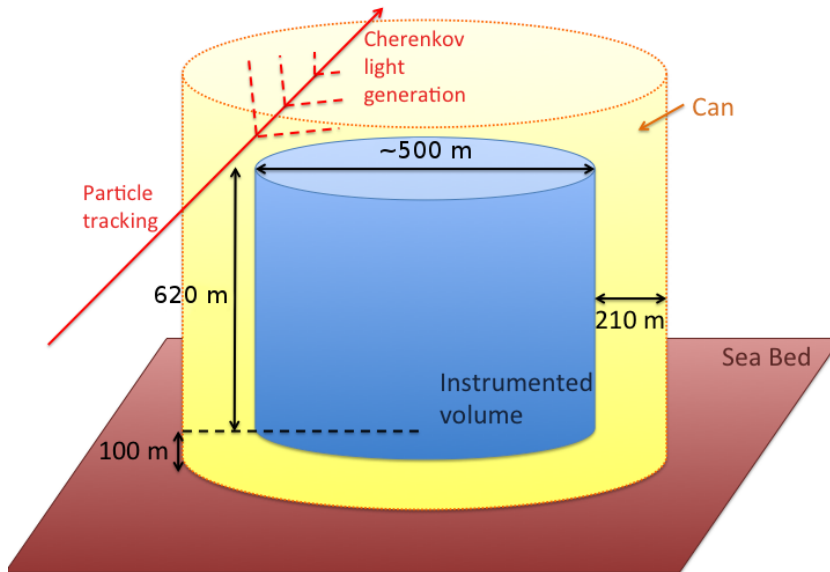


Figure 4.3: Overview of the detector geometry for the event simulation used in GENHEN. Neutrino interactions are generated in a larger volume and the resulting muons are propagated to the can (yellow); only inside it the Cherenkov light and the detector response are simulated.

Neutrinos with energies according to a user defined power law spectrum ($E^{-\gamma}$) are generated within this volume and their interactions are simulated, taking into account the different media, rock and water, around the detector. The neutrino direction is sampled isotropically in a user defined zenith angle range, or can be produced according to a point source with a given declination. The neutrino interactions are then simulated using LEPTO (87) (for deep inelastic lepton-nucleon scattering) and RSQ (88) (for resonant and quasi-elastic events). If interaction vertex is outside the can, the shortest distance from the neutrino vertex position to the can is calculated. If this distance is greater than the maximum muon range at that neutrino energy, no muon produced by this neutrino will ever reach the can and the event is rejected with no further processing. If the muon reaches the detector, the coordinates at can level are stored. For the remaining events with the interaction vertex inside the can, all the particles produced in the interaction are recorded (position, direction, energy, etc.) for further processing.

4. SIMULATION AND RECONSTRUCTION TOOLS

Neutrino fluxes and events weights

As mentioned above, the events are generated starting from a defined energy spectrum $E^{-\gamma}$. Furthermore, for each interacting neutrino, a generation weight is calculated. This is used to statistically treat the events for the analysis as it is then possible to reweight the flux with another spectrum. To do so, the following parameters are defined (89):

- $V_{gen}[\text{m}^3]$: the total generation volume.
- $I_\theta[\text{sr}]$: the angular phase space factor $2\pi \cdot [\cos \theta_{max} - \cos \theta_{min}]$ where θ_{max} and θ_{min} are the maximum and the minimum angles of generation.
- I_E : the energy space factor, equal to $(E_{max}^{1-\gamma} - E_{min}^{1-\gamma})/(1 - \gamma)$ (where E_{max} and E_{min} are the maximum and minimum energies of generation) and to $\ln(E_{max}/E_{min})$ for $\gamma = 1$.
- $\sigma(E)[\text{m}^2]$: the total neutrino cross section for energy E .
- $\rho \cdot N_A$: the number of target nucleon per m^3 ($N_A = 6.022 \times 10^{23} \text{mol}^{-1}$ is the Avogadro's constant). The code works in units of "water equivalent", fixing to one the density of all material and dividing the physical distances for the effective density.
- P_{Earth} : the probability for the neutrino to penetrate the Earth and vary from 0 to 1. It is defined as $P_{Earth}(E_\nu, \theta_\nu) = e^{-N_A \sigma(E_\nu) \rho_L(\theta_\nu)}$ where $\rho_L(\theta_\nu)$ is the amount of matter the neutrino encounters.
- t_{gen} : the generation time (arbitrary).
- N_{tot} : the total number of generated events.

In order to obtain the rate of events corresponding to the differential flux of a specific model

$$\Phi^{mod}(E_\nu, \theta_\nu) = \frac{d\phi_\nu^{mod}}{dE_\nu d\Omega_\nu dS dt} \quad (4.1)$$

the events generated with E_ν and θ_ν have to be reweighted with the ratio between the model flux and the generated flux through

$$W_{event} = \frac{\Phi^{mod}(E_\nu, \theta_\nu)}{\Phi^{gen}(E_\nu, \theta_\nu)} = W_{gen}(E_\nu, \theta_\nu) \times \Phi^{mod}(E_\nu, \theta_\nu) \quad (4.2)$$

W_{gen} is independent from the particular flux choice and is calculated in the generation phase. The flux of generated interacting neutrinos arriving at the detector is

$$\Phi^{gen}(E_\nu, \theta_\nu) = \frac{d\phi_\nu^{gen}}{dE_\nu d\Omega dS dt} = \frac{1}{W_{gen}} \quad (4.3)$$

$$= \frac{N_{total}}{V_{gen} \cdot I_\theta \cdot I_E \cdot E^\gamma \cdot \sigma(E_\nu) \cdot (\rho N_A) \cdot t_{gen} \cdot P_{Earth}} \quad (4.4)$$

Subsequently, to obtain a distribution of events corresponding to Φ^{mod} the user has to multiply the generation weight of each event to Φ^{mod} . This is convenient as it makes it possible for a range of different fluxes to be applied without recalculating all the individual elements of the weight.

Atmospheric neutrino flux

There are several calculations of the atmospheric neutrino flux depending on measurements of the primary cosmic-ray flux and different interaction models in the atmosphere (see Chapter 3.4). In this work, the events have been reweighted to consider the Honda model (78) (conventional atmospheric flux) and the Enberg model (83) (prompt atmospheric flux). Both have been corrected for the presence of the knee in the cosmic-ray spectrum.

For atmospheric neutrinos, the weight is implemented slightly differently in the files. As mentioned previously, the generation of atmospheric events is done using the Bartol model (which was then substituted with the Honda and Enberg models), thus the generation weight was multiplied by Φ^{Bartol} , resulting in the global weight. As the generation time t_{gen} is usually set to be one year, the generation weight is in [GeV m² sr s year⁻¹] and the global weight has a unit that can be understood as a “rate per year”. The number of reconstructed atmospheric neutrino events per year can be seen in Figure 4.4, including the number of reconstructed cosmic neutrino events from the IceCube diffuse models mentioned in Chapter 3.3.3.

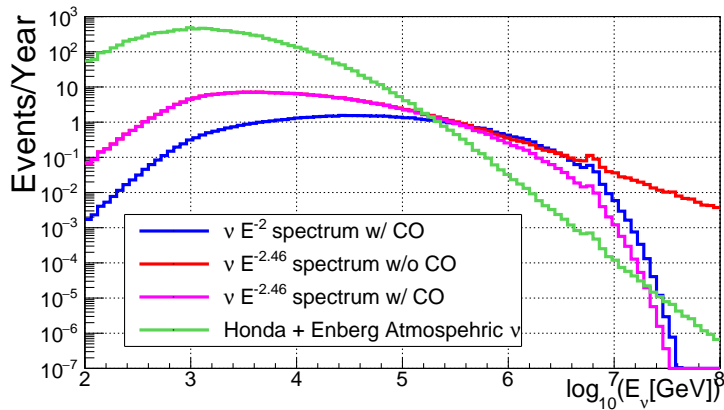


Figure 4.4: Number of expected neutrino events per year with respect to the neutrino energy for various fluxes (both cosmic and atmospheric).

Neutrino absorption in the Earth

The probability of a neutrino being absorbed as it passes through the Earth depends on the density of matter along its path and the neutrino interaction cross-section. The integrated column density of the Earth $\rho_L(\theta_\nu) = \int_L \rho_{Earth}(r) dL$ along the neutrino path L corresponding to a given zenith angle θ is seen on the left plots of Figure 4.5 and the Preliminary Reference Earth Model (PREM) (90) is used for the Earth's density profile $\rho_{Earth}(r)$. The column density seen by upgoing neutrinos is enhanced due to the increased density of the Earth's core.

The probability of transmission through the Earth is given by

$$P_{Earth}(E_\nu, \theta_\nu) = e^{-N_A \sigma(E_\nu) \rho_L(\theta_\nu)} \quad (4.5)$$

and is shown in the right plot of Figure 4.5 as a function of neutrino energy and zenith angle.

For neutrino directions close to vertically upwards, absorption in the Earth starts to be significant for neutrino energies above 10 TeV. Indeed, Figure 4.5 shows that the attenuation of the neutrino flux in the Earth is important, and affects the zenith and energy dependence of the flux at the detector. Above 1 PeV, only neutrinos close to the horizon remain unattenuated, which strongly suppresses the neutrino flux above this energy. Showing that the Earth is opaque to very high energy neutrinos.

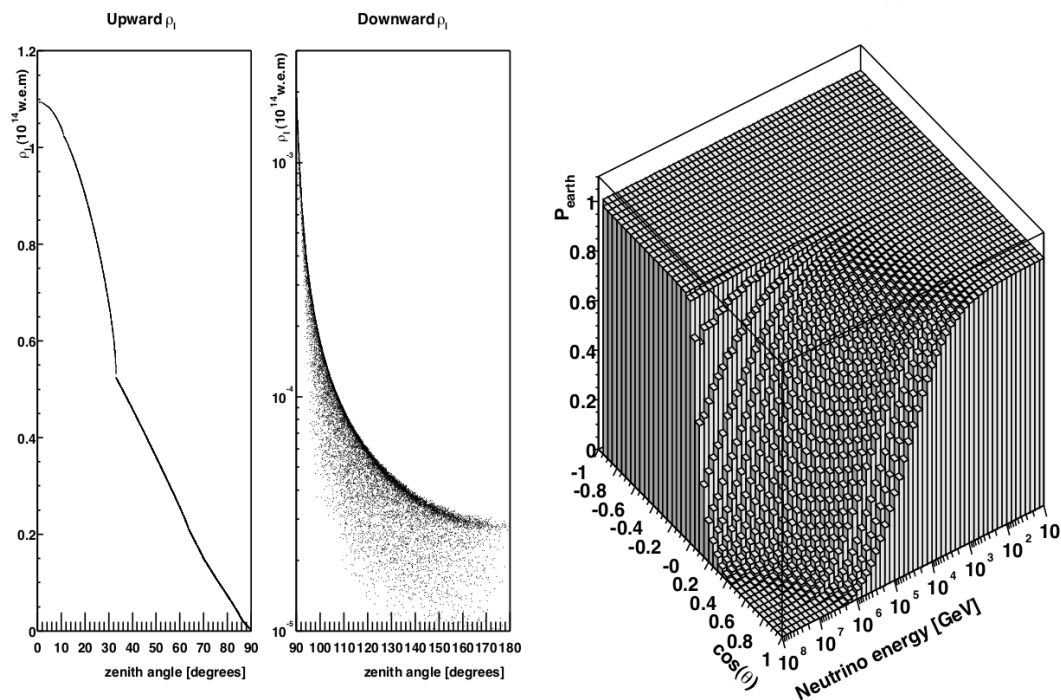


Figure 4.5: Left panel: Line integrated column density of the Earth as a function of the zenith angle. Right panel: Transmission probability as a function of energy and zenith angle of the neutrino (with $\cos(\theta) = 1$ being vertically upwards, i.e. from a path down through the Earth). (91)

4.1.3 Generation of Atmospheric Muons

The generation of atmospheric muons can be carried out by two programs, CORSIKA (92) and MUPAGE (93, 94). CORSIKA provides a more detailed simulation of extensive air showers initiated by high energy cosmic rays particles. Nevertheless a fast MC generator is essential to reduce computing time and as a result, in this thesis, the MUPAGE package will be used instead. The program is developed from parametric formulas derived in (93), that describe the flux, the angular distribution and the energy spectrum of underwater muon bundles with maximum depth from 1.5 to 5 km w.e. and with zenith angles from 0° to 85° . The parametrization of the interaction of cosmic rays and the propagation in the atmosphere up to the sea level is based the on HEMAS code (95, 96) and on MACRO data (97, 98), while the propagation of muons until 5 km under the level of the sea was performed by MUSIC (99). MUPAGE generates muons directly on the can surface with a height and radius defined by the user (but usually it uses the same can surface defined in GENHEN). It's assumed that all the muon bundles are parallel to the axis of the

4. SIMULATION AND RECONSTRUCTION TOOLS

shower and that they arrive at the same time into a plane perpendicular at the axis. For every N simulated events a “lifetime” is estimated. The lifetime is the time that one would have to run the real experiment to obtain the same N muons as in the simulated dataset.

Two sets of atmospheric muon bundles were generated, one with an energy threshold E_{th} of 10 TeV and one with an energy threshold of 50 TeV. On the one hand, $23.75 \cdot 10^6$ events were created for $E_{th} > 10$ TeV. In each file, $2.5 \cdot 10^4$ events were generated corresponding to a lifetime of about four months. On the other hand, $3.5 \cdot 10^6$ events were created for $E_{th} > 50$ TeV. In this case, the total lifetime corresponds to more than 2 years worth of events.

The definition of the weight is quite straightforward in the case of atmospheric muons. It's simply the number of seconds in a year divided by the lifetime of each file in seconds. In Figure 4.6, the number of reconstructed event per year for the 10 TeV and the 50 TeV atmospheric muons are shown, as a function of the muon bundle energy.

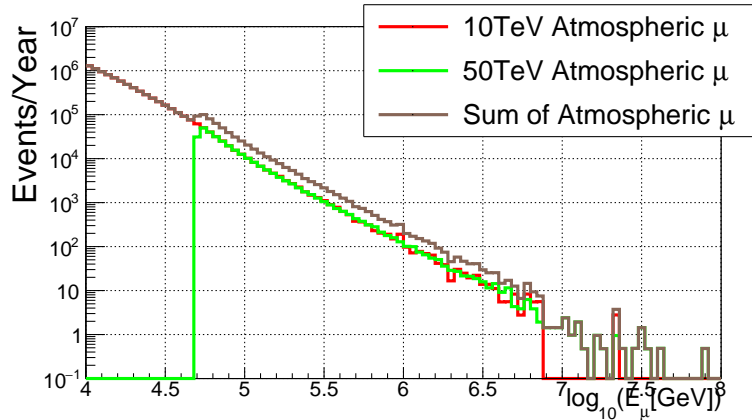


Figure 4.6: Number of expected atmospheric muon events per year with respect to the muon bundle energy.

4.1.4 Propagation of Particles and Light Production

Once the particles are generated they must be propagated through the volume. In order to take into account the light produced in water, there are three types of particles inside the can:

- Muons that are characterized by long, approximately straight tracks continuously losing energy and emitting Cherenkov photons. They also suffer stochastic losses which produce independent electromagnetic (EM) showers.
- EM showers that are either produced by bremsstrahlung photons from muons or by electrons at the neutrino interaction vertex. All their energy is deposited in a short distance (on the scale of the detector) and can generally be considered point-like. They contain a large number of electrons and hence, statistically, showers of a similar energy all have similar properties.
- Hadrons at the neutrino interaction vertex, that have complex decay chains and the amount of light they produce depends on the primary particle and its particular set of decays. In addition, they may produce muons in the final state which may travel a significant distance. Hence, they are not amenable to parametrization in the same way electrons and muons are.

KM3 - light propagation and detection

KM3 (100) is a full photon tracking simulation used to generate the light produced by muons. The code takes into account all the muon interaction mechanisms with matter (multiple scattering, ionization, bremsstrahlung, couple production, inelastic scattering,...), its energy loss and Cherenkov photon emissions, with all the related absorption and diffusion processes in the sea water. The resulting photons are then propagated to the DOMs. A full simulation where every single photon would be generated and propagated individually would not be possible as they would take a huge CPU time. This is avoided by generating absorption and diffusion photon tables with different photon energies and then using interpolations on these pre-made tables. These tables store the distributions of the arrival times and numbers of PMT hits at different distances, positions and orientations with respect to a given muon track or electromagnetic shower. They also contain the DOM properties and have to be recalculated for each type of DOM considered. The light from the hadronic showers is taken into account in KM3 assuming the “one particle approximation” basis, where the wide range of secondary particles which get produced in neutrino interactions (other than muons) must be made to “look like” electron and muon events. This means approximating all the hadronic and electromagnetic cascades produced by

4. SIMULATION AND RECONSTRUCTION TOOLS

the secondary particles with a single electron cascade, such that the total number of Cherenkov photons produced remains the same. The KM3 package is divided into three subpackages: GEN, HIT and KM3MC.

GEN - photon table generation

GEN simulates the generation of Cherenkov light by a particle in a given medium (in this case water), including light from any secondary particles. A complete GEANT3.21 (101) simulation is used at this step. The first stage in the generation of photon tables is to perform simulations of either short segments of muon tracks or electromagnetic showers; then to track the Cherenkov photons through space, taking into account the wavelength-dependent water absorption and scattering (see Figure 1.10), while recording the distributions (position, direction and arrival time) of photons as they cross spherical shells surrounding the simulated particles. Its output consist of a table containing all the photons recorded in each spherical shell and an ASCII file containing the information relevant to the simulation (particle type, energy, number of processed events, track length, medium type, number of events stored in each shell, water model used,...). As such, a key part of its input is the water properties, such as those seen in Figure 1.10 (in Chapter 1.1.4).

HIT - DOM hit generation

HIT transform the photon fields from GEN into DOM hit probability distributions for muon track segments and EM showers. The hit number, position, direction, energy and arriving time are read shell by shell and stored. Since a large number of hits is recorded for each shell, these shells are divided in bins of $\cos \theta$ (see Figure 4.7). For each bin in $\cos \theta$ the flux of photons is weighted by the PMT effective area as a function of wavelength and orientation to give the final photon tables. The PMT effective area is thus given by

$$A_{eff}^{DOM} = A_{geom}(\theta_{DOM}) \times QE(\lambda) \times CE \times P_{trans}^{glass}(\lambda, \theta_{DOM}) \times P_{trans}^{gel}(\lambda, \theta_{DOM}) \quad (4.6)$$

where λ is the photon wavelength, $QE(\lambda)$ is the quantum efficiency (the probability that a photon generates a photoelectron inside the PMT), CE is the collection efficiency (the probability that an electron into the PMT be accelerated until the first

photocathode) and finally P_{trans}^{glass} and P_{trans}^{gel} are the transmission probabilities for the glass and the gel that constitutes the DOM. Thus it is important to input the PMT characteristics, such as those seen in Figure 2.6 (in Chapter 2.3).

For each case (muon or showers of given energy) four DOM hit distributions are produced:

- Probability of a direct hit (no scattering).
- The inverse cumulative time distribution of direct hits.
- Probability of a scattered hit.
- The inverse cumulative time distribution of scattered hits.

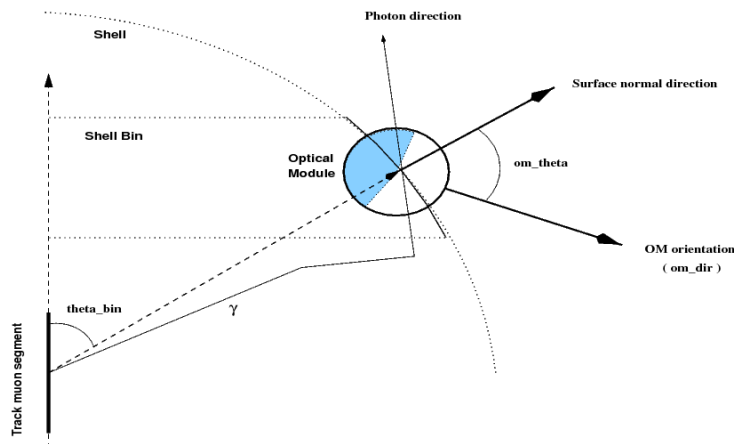


Figure 4.7: Schematic diagram of the geometry used to generate the photon tables.
(2)

The inclusion of scattering in the simulation of the Cherenkov light produced by high energy muons is essential as this parameter is quite significant at higher energies where the quality of the reconstruction dominates the angular resolution.

KM3MC - detector response simulation

Finally, KM3MC is a detector simulation program which is fed users inputs and the hit probability distributions generated in HIT to simulate the detector response to the passage of high energy muons. Muons are then propagated in short steps through

4. SIMULATION AND RECONSTRUCTION TOOLS

the can volume with the MUSIC package (99), generating segment of track (of the same dimension of those used by GEN) until the muon stops or leave the detector. If the energy loss is greater than a threshold value, an EM shower is generated in a random position of the segment track.

The numbers and, for muons with close to minimum ionizing energy losses, arrival times of PMT hits are drawn from the muon table created above. For sections of muon tracks with an energy loss above some threshold an electromagnetic shower is defined and the PMT hits are drawn from the electron tables. Every signal hit, obtained from track and shower parameters and from photon tables, is characterized by the identification of the PMT involved, by the number of deposited photoelectrons (p.e.) and by the photon arrival time.

4.1.5 Generation of Optical Background and Triggering

JTriggerEfficiency (JTE) is provided by Jpp which is a Java inspired set of C++ interfaces, classes and methods. Jpp was developed by Maarten de Jong (NIKHEF) and provides for 2D and 3D geometry packages, multi-dimensional interpolation methods, numerical integration, PDFs of the arrival time of Cherenkov light, muon energy loss methods, neutrino interaction cross sections and so on.

JTE makes it possible to generate random hits with a frequency that can be defined by the user, thus allowing to simulate the ^{40}K decays and the bioluminescent background in the sea water. Hits from background photons are simulated by adding random noise hits with a rate of 5 kHz per PMT. Correlated hits over multiple PMTs on the same DOM from single ^{40}K decays are also included, with {2,3,4,5}-fold coincidences at rates of {500,50,5,0.5} Hz per DOM.

Futhermore, JTE can suppress the influence of background hits and speed up the triggering process by performing a hit selection which is then passed to the trigger algorithms. An L1 hit is a hit that has a time difference of 20 ns with another hit in the same DOM. The goal of triggering is to register neutrino events with a high efficiency while maintaining the rate of background events to acceptable levels. For that purpose, there are many trigger parameters which can be enforced, including the option of combining multiple single hits within a limited time window (typically 20 ns); this provides a lower trigger efficiency but retains a higher purity. In particular,

the hit selection proceeds by first selecting all the local coincidences, i.e. coincidences of hits within the same DOM, in a time window of 10 ns (L1 hit) and for which the PMTs involved are less than 90° apart (L2 hit). Among them, a cluster is selected such that any hit in the cluster is causally related to all the remaining ones, according to the following causality relation

$$|\Delta t| < \frac{d}{c_{water}} + 20 \text{ ns} \quad (4.7)$$

where $|\Delta t|$ is the time difference between the two hits, d is the distance between the two PMTs concerned and c_{water} is the group velocity of light in water.

Another hit selection is based on the maximum time during which correlated light can be observed on any DOM in the the detector (called “3DShowerTrigger”) and on any PMT within the detector under a track assumption (called “3DMuonTrigger”). This means that if there are more than five correlated L1 hits in a selected time window, the event is triggered. Furthermore, in the case of a 3DMuonTrigger, the maximum time in which correlated light can be observed also depends on the distance of PMTs that are hit along the track and the distance of these PMTs perpendicular to the track.

4.2 Reconstruction Tool

Two broad event classes can be identified in a high energy neutrino telescope, track-like events and cascade-like events:

- The track-like events are generated by muons that are produced in the matter inside or surrounding the detector through CC interactions of muon and tau neutrinos.
- The cascade-like events are produced in the matter near or inside the detector volume through CC interactions of electron and tau neutrinos and in NC interactions of neutrinos of all flavours.

These two events classes (mentioned in Chapter 1.1.1) produce very different time-space hit patterns in the detector. The cascade-like events are characterized by a very dense hit pattern close to the neutrino interaction point. A significant fraction of the

4. SIMULATION AND RECONSTRUCTION TOOLS

neutrino energy is released in a hadronic shower and, in the case of electron neutrino CC interactions, also in an electromagnetic cascade, thus providing a good estimate of the neutrino energy. A track-like event is characterized by the Cherenkov light from the emerging muon that can travel large distances through Earth and seawater. As the spatial hit pattern is closely related to the muon direction, this allows for a precise measurement of the latter.

The objective of track-like event reconstruction algorithm is to estimate the trajectory of relativistic muons (and consequently neutrinos) using the combined information of the PMT spatial positions and the Cherenkov photon arrival times.

The task of a reconstruction algorithm is to provide an estimate of the parameters which define the muon trajectory and to establish track-fit quality parameters which can be used to reject badly reconstructed events.

The muon tracks are defined by five independent parameters: the position of the muon $\mathbf{P} \equiv (p_x, p_y, p_z)$ at a given time t_0 along the trajectory and its normalized direction $\vec{d} \equiv (d_x, d_y, d_z)$ which can also be parametrized in terms of the azimuthal and zentral angles ϕ and θ : $\vec{d} \equiv (\sin \theta \cos \phi, \sin \theta \sin \phi, \cos \theta)$. Figure 4.8 shows a sketch of the track description employed in the reconstruction. Defining $\vec{v} = \mathbf{Q}_i - \mathbf{P}$ as the vector that goes from the point \mathbf{P} to the hit position \mathbf{Q}_i the expected arrival time of the photon on the PMT can be written as a function of the components of \vec{v} , parallel and perpendicular to the muon direction, that are respectively $l = \vec{v} \cdot \vec{d}$ and $k = \sqrt{|\vec{v}|^2 - l^2}$. The distance from \mathbf{P} to the point \mathbf{P}_i where the Cherenkov light is emitted is therefore

$$\overrightarrow{\mathbf{P}\mathbf{P}_i} = l - (k/\tan \theta_C)$$

while the path travelled by the photon to reach the PMT is

$$b = k/\sin \theta_C$$

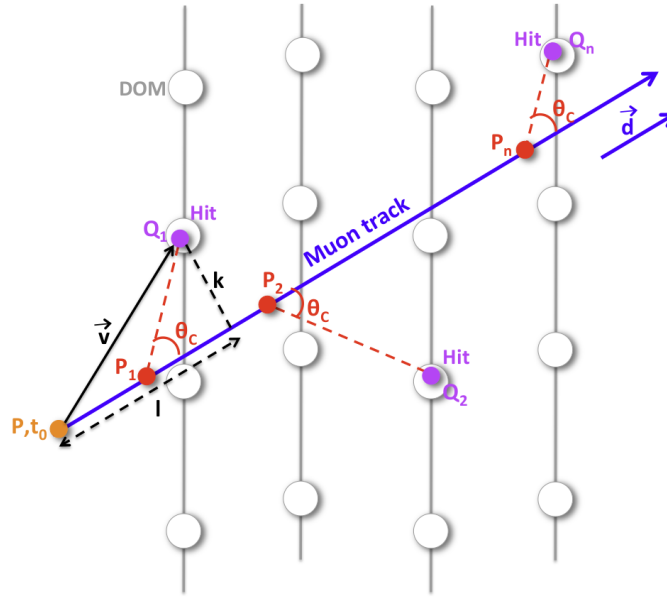


Figure 4.8: Description of the geometry for the detection of the Cherenkov light emitted by a muon (blue line) that goes through the point \mathbf{P} (orange point) in direction \vec{d} . The Cherenkov light (red dashed lines) reaches the PMTs located in points \mathbf{Q}_i (lilac points). (2)

Thus the expected arrival time of the light in \mathbf{Q}_i is given by (102)

$$\hat{t} = t_0 + \frac{1}{c} \left(l - \frac{k}{\tan \theta_C} \right) + \frac{1}{c/n} \left(\frac{k}{\sin \theta_C} \right) \quad (4.8)$$

One of the most important quantities needed in event reconstruction is the so called “time residual” $r_i = t_i - \hat{t}_i$, defined as the difference between the expected arrival time \hat{t}_i of the Cherenkov photon on the i -th PMT and the recorded hit time t_i (in the absence of scattering and dispersion of light).

The time residual is calculated according to the track hypothesis, meaning under the assumptions that the event starts at a time t_0 , the muon travels on a straight line with speed c and the Cherenkov light is emitted at a Cherenkov angle $\theta_C \sim 42.2^\circ$ with respect to the muon direction with a speed c/n , where n is the refractive index in the medium ($n \sim 1.35$). Note that, knowing the time t_i and the position of each hit \mathbf{Q}_i , the time residual depends only on the parameters \mathbf{P} and \vec{d} .

4. SIMULATION AND RECONSTRUCTION TOOLS

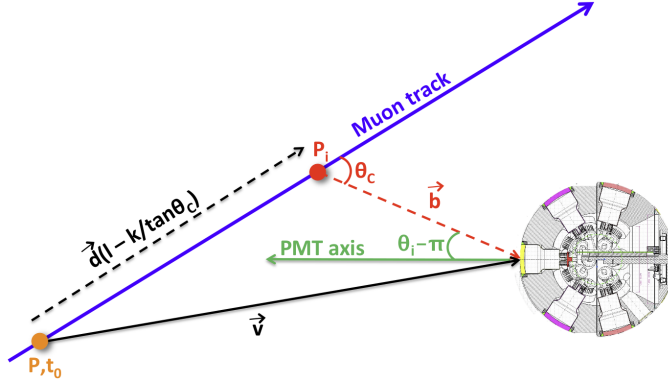


Figure 4.9: Scheme showing the expected angle of incidence θ_i of the photon on the PMT. (2)

The selected hits serve as input of the first step of the track reconstruction procedure, referred to as “linear prefit”, which is a linear fit through the positions of the hits. Once a first estimate of the track parameters is obtained, the evaluation for each hit of the expected angle of incidence θ_i of the photon on the PMT is possible. Figure 4.9 shows this angle between the direction of the photon and the pointing direction of the PMT. Thus an “angular selection” can be performed and the prefit is repeated with the new hit set. The angular selection helps exploit the PMT directionality.

Additional starting tracks are obtained by rotating the prefit track around the original point. For each starting track, two fits called M-estimator fit and PDF fit are performed. These fits are based on the maximum likelihood method and use multi-dimensional Probability Density Function (PDF) that depend on the time residuals. The input track for the PDF fit is the track resulting from the M-estimator fit. The hit set used in each fit procedure is accurately selected on the basis of the time-space correlation with the starting track. Therefore, using time residuals, some of these tracks are discarded because the number of hits remaining after the hit selection is not sufficient to proceed. The M-estimator and the PDF fit are performed for all the remaining tracks and the best one is kept for further processing. Once the fitting procedures are performed for each starting direction, the likelihood is used to choose the best track.

4.2.1 JGandalf Chain

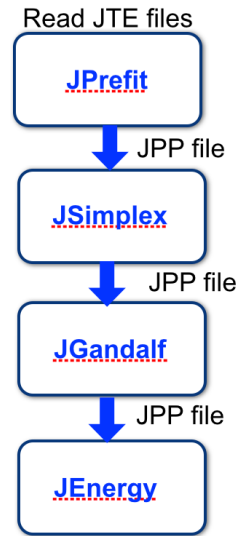


Figure 4.10: Scheme of the routines used to reconstruct events in the JGandalf Chain.

This relatively new reconstruction algorithm incorporates a list of processes included in JFit, a subdirectory to the Jpp library. This “à la carte” event reconstruction algorithm makes it possible to choose which series of routines to carry out depending on the user’s needs. As shown in Figure 4.10, the programs which will be used in this work are JPrefit, JSimplex, JGandalf and JEnergy, and they will be briefly explained.

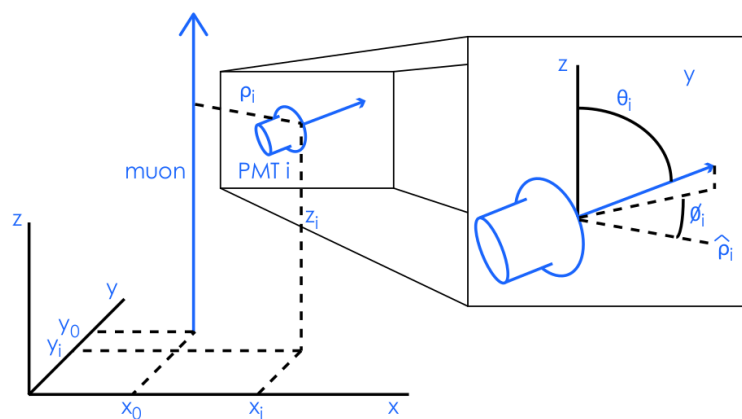


Figure 4.11: Coordinate system used in the muon trajectory fit. (103)

The main difficulty in the reconstruction of the muon trajectory is the non-linearity of the problem. This is overcome by using a prefit (through **JPrefit**), which despite

4. SIMULATION AND RECONSTRUCTION TOOLS

not being very accurate, provide a suitable set of start values for the final trajectory fit. Assuming that the muon direction is known, and defining the coordinate system as that in which the muon travels along the z -axis, crossing the $z = 0$ plane at coordinates x_0, y_0 at time t_0 (Figure 4.11) the determination of the track parameter can be reduced to a linear problem. The expected arrival time of the Cherenkov photons on the i -th PMT in this coordinate system (103)

$$\hat{t}_i = t_0 + \frac{z_i}{c} + \tan \theta_C \frac{\rho_i}{c} \quad (4.9)$$

$$\text{where } \rho_i = \sqrt{(x_i - x_0)^2 + (y_i - y_0)^2} \quad (4.10)$$

where ρ_i is the minimum distance of approach of the muon to the PMT and z_i is the distance from the PMT to the $z = 0$ plane. The linear fit can thus be performed on three parameters $\{x, y, t\}$ using the χ^2 method.

Nevertheless, the linear fit is sensitive to outliers from optical background hits (^{40}K decays and bioluminescence) and strongly scattered photons and this leads to a not accurate determination of the track direction. A scan of the solid angle in the sky is also performed and the best N tracks are selected.

From the best N tracks selected by JPreFit, the **JSimplex** code excludes optical background hits and strongly scattered photons by selecting a cluster of causally related hits from the data. In particular it selects the first L1 and L0 hits within an established travel distance and time window. Taking into account only the hits selected using Powell's method, this program performs a five parameter M-estimator fit of $\{x, y, t, dx, dy\}$. This procedure is repeated for a scan of assumed track directions with a typical grid angle of one degree. Here the fit quality Q is quantified as

$$Q = N_{dof} - 0.25 \times (\chi^2/N_{dof}) \quad (4.11)$$

where N_{dof} is the number of degree of freedom. With N_{hit} the number of hits used in the final fit, $N_{dof} = N_{hits} - 5$ since there are 5 parameters to consider: the 3 coordinates of \mathbf{P} , and the ϕ and θ angles.

JGandalf on the other hand, uses the N best starting values from JSimplex to perform the PDF fit of the muon trajectory. A likelihood search is carried out, using the Levenberg-Marquardt method, in which all five independent trajectory

parameters are fitted simultaneously. In the likelihood function, the PMT response is described by a set of PDFs

$$\mathcal{L} = \prod_i \frac{\partial P}{\partial t}(\rho_i, \theta_i, \phi_i, r_i) \quad (4.12)$$

where θ_i and ϕ_i describe the orientation of the PMT (Figure 4.11) and r_i is the time residual. The set of PDFs are calculated semi-analytically for unscattered and single-scattered light from Cherenkov radiation and from energy losses of the muon and include the effects of dispersion as well as the optical background rate and the quantum efficiency, angular acceptance and transit time spread of the PMTs. To provide partial derivatives and to limit computational time, the PDFs are evaluated using interpolating functions in 4D.

JEnergy uses the N best starting values from JGandalf to perform a fit of the muon energy. With the muon trajectory determined, the energy of the muon is fitted using the spatial distribution of hit and non-hit PMTs. The probability of a PMT being hit is obtained from the same PDFs mentioned previously

$$\mu(\rho, \theta, \phi) \equiv \int_{T_{min}}^{T_{max}} dt \frac{\partial P(\rho, \theta, \phi, r)}{\partial t} \quad (4.13)$$

where $\mu(\rho, \theta, \phi)$ is the number of photo-electrons. For lower energy muons, the energy is proportional to the path length (see Figure 1.2). This approach works if the muon is contained within the detector, and the starting and stopping points can be determined. At energies above a few TeV, the dE/dx can be measured and the average muon energy is deduced from that value. Thus the energy estimation is based on the relation:

$$-\frac{dE}{dx} = a(E) + b(E)E \quad (4.14)$$

where the contribution to the light yield comes not only from the Cherenkov and Bremsstrahlung radiation but also from the random background. All PMTs within a predefined distance (200 m by default) around the muon trajectory are used and the calculated hit probability is compared to the actual occurrence of a hit.

The reconstruction efficiency - the number of reconstructed event divided by the number of triggered events - with respect to the neutrino energy is shown in Figure 4.12. At neutrino energies below 1 TeV, event reconstruction drops in efficiency as the resulting muon track length shortens and less the events are triggered as they do not pass the reconstruction requirements.

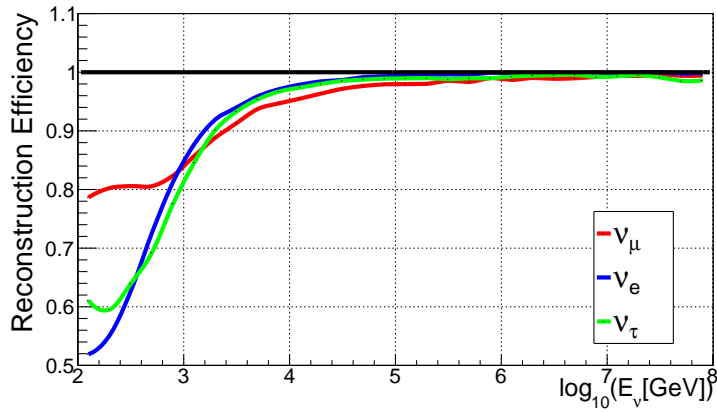


Figure 4.12: Reconstruction efficiency with respect to the neutrino energy.

4.2.2 Reconstruction Parameters

The reasoning adopted in the reconstruction algorithm is to reconstruct as many events as possible without applying specific selection criteria. Instead, selection criteria can be applied afterward, depending on the demands of the particular physics analysis. Some quantities provided by the JGandalf Chain are somewhat straightforward, as they are estimations of common physical quantities: the reconstructed energy (E_{rec}), the reconstructed nadir angle (θ_{rec}) and the number of hits involved in the track reconstruction (N_{hit}). Their distributions are shown in Figure 4.13. N_{hit} can play the role of an energy estimator, although less precise. But even if N_{hit} is not an exact energy estimator, it is possible to select events with energy greater than a given value using a cut on N_{hit} , as seen in Figure 4.14.

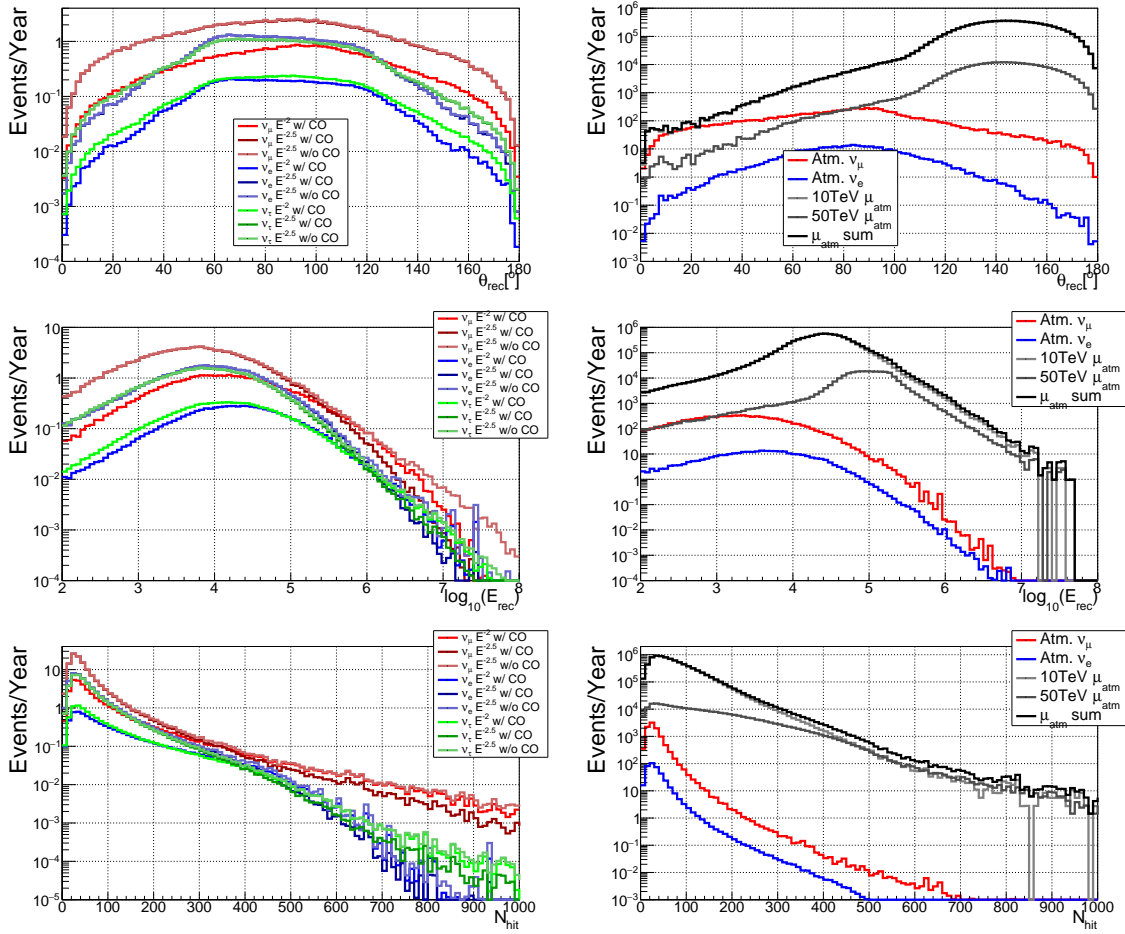


Figure 4.13: Distribution of the track reconstruction parameters with the cosmic events in the left panels and the atmospheric events in the right panels. The black line represents the sum of both the 10 TeV and 50 TeV atmospheric muons.

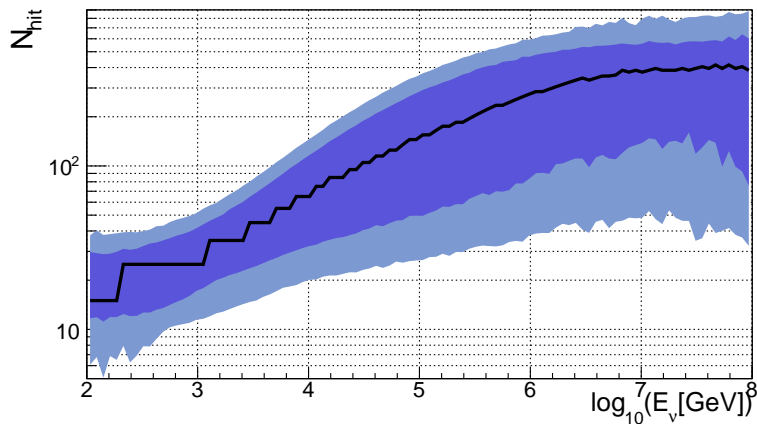


Figure 4.14: Median number of N_{hit} (black line) as a function of the generated neutrino energy. The colored bands represent the 68% and 90% quantiles.

4. SIMULATION AND RECONSTRUCTION TOOLS

Some others are results of the statistical method used in the reconstruction chain, such as the likelihood (defined by Equation 4.12 in Chapter 4.2.1). Finally, β is the angular error estimation on the direction of the reconstructed muon track. It is defined as $\beta = \sqrt{\sigma_\theta^2 + \sin^2 \theta \times \sigma_\phi^2}$ where σ_θ and σ_ϕ are the error estimates of a track's zenith and azimuth angles. The distributions for both are shown in Figure 4.15. Thus the likelihood and β parameters are essentially estimators of the track reconstruction quality, assisting with the rejection of badly reconstructed events (as shown in Figure 4.16).

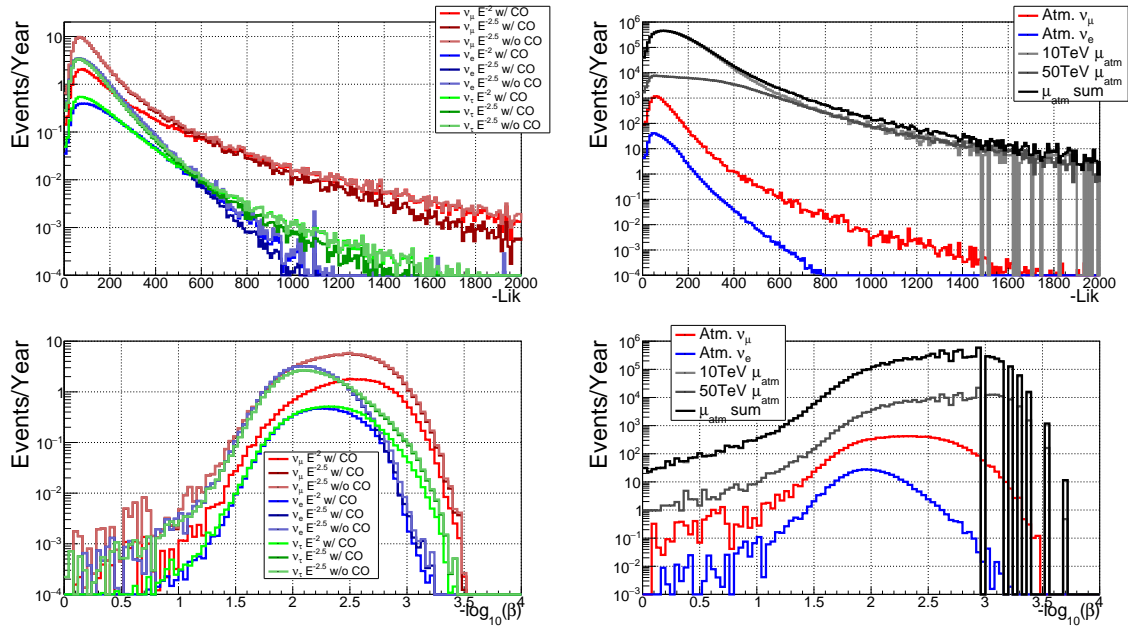


Figure 4.15: Distribution of the track reconstruction quality parameters with the cosmic events in the left panels and the atmospheric events in the right panels. The black line represents the sum of both the 10 TeV and 50 TeV atmospheric muons.

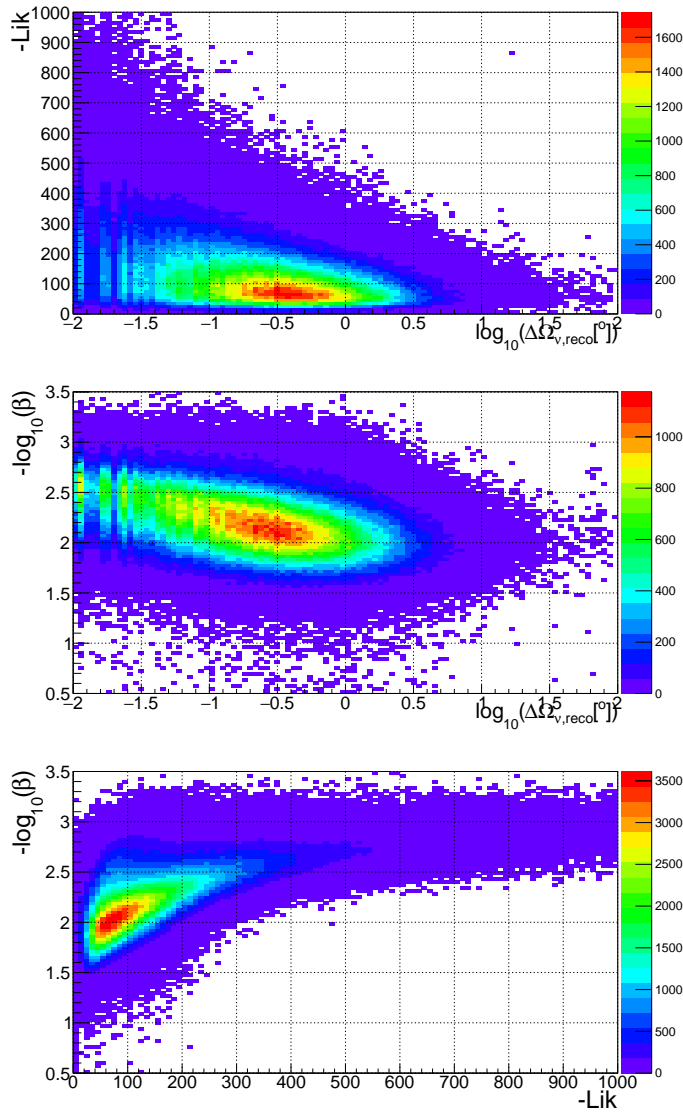


Figure 4.16: Upper panel: Likelihood versus the angular distance $\Delta\Omega_{\nu, reco}$. Center panel: β versus the angular distance $\Delta\Omega_{\nu, reco}$. Lower panel: Likelihood versus β .

Although this analysis, and consequently this reconstruction algorithm, has been optimized for relativistic muon tracks, some ν_e and ν_τ events are expected to produce track-like topologies and thus to be reconstructed as well. Fortunately, the use of Monte Carlo simulations allows for some unique insight into the distributions of all these events. As this is solely for visualization purposes, the distinction will often not be necessary in the remainder of this work.

4. SIMULATION AND RECONSTRUCTION TOOLS

Chapter 5

PERFORMANCE ANALYSIS

This chapter ties together the previous descriptive chapters and describes the analysis to evaluate the performance expected from the first phase of the KM3NeT/ARCA detector to diffuse neutrino fluxes. To do so, a few key notions will be introduced, including that of “neutrino effective area”. The concept of angular resolution and energy resolution will also be ushered in. The neutrino effective area, and the energy and angular resolution are quantities independent of the neutrino flux model considered and are evaluated by means of Monte Carlo (MC) simulations.

Two main methods are exploited to evaluate the detector performance and will be presented, together with the results obtained for the three assumed diffuse neutrino fluxes (see Chapter 3.3.3).

5.1 Neutrino Effective Areas

For a given neutrino flux $d\Phi/dE_\nu d\Omega_\nu$, the expected event rate dN_ν/dt measured by the detector is (91)

$$\frac{dN_\nu}{dt} = \iint A_{eff}^\nu(E_\nu, \theta_\nu) \frac{d\Phi}{dE_\nu d\Omega_\nu} dE_\nu d\Omega_\nu$$

where $A_{eff}^\nu(E_\nu, \theta_\nu) = V_{eff}(E_\nu, \theta_\nu) \times (\rho N_A) \times \sigma(E_\nu) \times P_{Earth}(E_\nu, \theta_\nu)$

is the effective area, $V_{eff}(E_\nu, \theta_\nu)$ is the effective volume, ρN_A is the target nucleon density (m^{-3}), $\sigma(E_\nu)$ is the neutrino cross-section (m^2) and $P_{Earth}(E_\nu, \theta_\nu) = e^{-N_A \times \sigma(E_\nu) \times \int_L \rho_{Earth}(r) dL}$ is the probability of neutrino transmission through the Earth.

5. PERFORMANCE ANALYSIS

5.1.1 Neutrino Effective Volume

Before the direct calculation of the effective area, the effective volume must be introduced. The effective volume is the volume of a 100% efficient detector for observing neutrinos that interact within that volume with the same event rate as the KM3NeT/ARCA Phase-1 detector for a given neutrino interaction rate. This quantity includes the efficiency of the detector i.e. the fraction of the neutrino that the detector can observe

$$V_{eff}^{\nu}(E_{\nu}, \theta_{\nu}) = \frac{N_{sel}(E_{\nu}, \theta_{\nu})}{N_{gen}(E_{\nu}, \theta_{\nu})} \times V_{gen} \quad (5.1)$$

The neutrino effective volume is obtained by using the generation volume V_{gen} (introduced in Chapter 4.1.2), the number of selected events N_{sel} and the number of generated events N_{gen} in the same bin. Also mentioned in Chapter 4.1.2, the generation spectrum is a power law $E^{-\gamma}$, therefore the number of generated events N_{gen} in the angular bin θ_1 to θ_2 and the energy bin E_1 to E_2 is

$$\begin{aligned} N_{gen} & (E_1 < E_{\nu} < E_2, \cos \theta_1 < \cos \theta_{\nu} < \cos \theta_2) \\ &= \frac{\cos \theta_2 - \cos \theta_1}{\cos \theta_{max} - \cos \theta_{min}} \times \frac{\int_{E_1}^{E_2} E^{-\gamma} dE}{\int_{E_{min}}^{E_{max}} E^{-\gamma} dE} \times N_{total} \end{aligned} \quad (5.2)$$

with E_{min} , E_{max} , $\cos \theta_{min}$, $\cos \theta_{max}$ are the minimum and maximum values of the generated energy and zenith angle, and N_{total} is the total number of simulated events. The neutrino effective volume for the $\nu_{\mu} + \bar{\nu}_{\mu}$ triggered events (for both NC and CC) is reported in Figure 5.1.

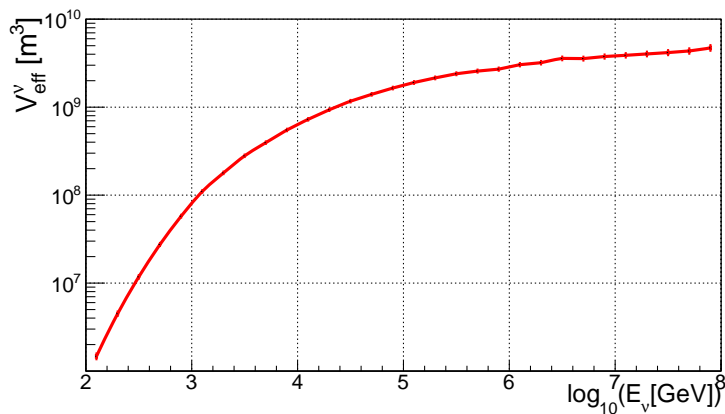


Figure 5.1: The ν_{μ} effective volume at trigger level.

5.1.2 Neutrino Effective Area

The effective area is the surface needed to observe the same event rate as seen by the KM3NeT/ARCA Phase-1 detector, assuming that the said surface is 100% efficient at detecting throughgoing neutrinos.

To calculate the neutrino effective area, a weight is calculated for each generated event, the generation weight w_2 . As previously mentioned in Chapter 4.1.2, the weight w_2 is defined as (89)

$$w_2 = V_{gen} \times I_\theta \times I_E \times E_\nu^\gamma \times \sigma(E_\nu) \times (\rho N_A) \times t_{gen} \times P_{Earth} [\text{GeV m}^2 \text{ sr s year}^{-1}]$$

where $\gamma = 1.4$ is the generation energy spectrum slope, t_{gen} is the number of seconds per year, $I_\theta(\text{sr})$ is the angular phase space factor $2\pi \cdot (\cos \theta_{max} - \cos \theta_{min})$ as θ is the zenith angle. Putting everything together, the effective area A_{eff}^ν for the full sky is

$$\begin{aligned} A_{eff}^\nu(E_\nu) &= \frac{N_{sel}(E_\nu)}{N_{gen}(E_\nu)} \times w_2 \times I_\theta^{-1} \times I_E^{-1} \times E_\nu^{-\gamma} \times t_{gen}^{-1} \times N_{total} \\ &= \frac{N_{sel}(E_\nu) \times w_2}{N_{total} \times 4\pi \times E_\nu^\gamma \times t_{gen}} \times \frac{1 - \gamma}{E_2^{1-\gamma} - E_1^{1-\gamma}} \times N_{total} \end{aligned} \quad (5.3)$$

The effective area is shown in Figure 5.2 for the events selected after the trigger (see Chapter 4.1.5) for the 24 strings configuration and for the 1 block (115 strings) configuration. The peak at 6.3 PeV is due to the Glashow resonance (85), a resonant W production on atomic electrons which increases the sensitivity to $\bar{\nu}_e$.

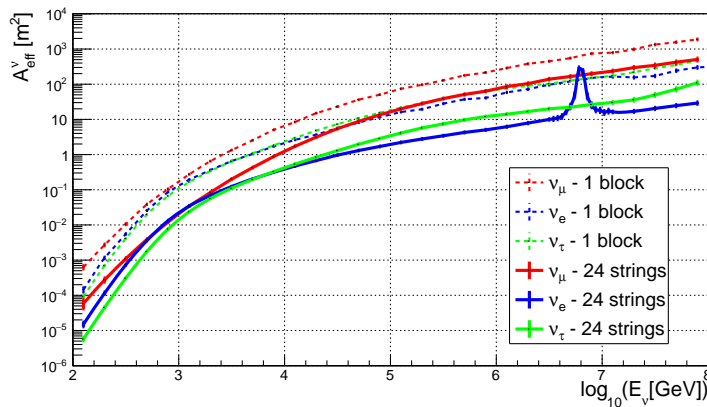


Figure 5.2: Neutrino effective areas at trigger level, for 1 block and 24 string configurations.

5. PERFORMANCE ANALYSIS

From this point on, the analysis will be carried out considering the detector's first construction phase (24 string configuration) and will rely on events that have been reconstructed using the JGandalf Chain.

5.2 Energy and Angular Resolution

5.2.1 Energy Resolution

Without any kind of external veto, it is not obvious to determine the muon energy. Indeed, only in this case, the selection of full or partially contained events can be done. High-energy muons can travel long distances (see Chapter 1.1.1) and the energy released in the detector volume can be only a fraction of the total muon energy. Nevertheless, the JEnergy code described in Chapter 4.2.1 estimates the muon energy using the photon hit Probability Density Functions (PDFs).

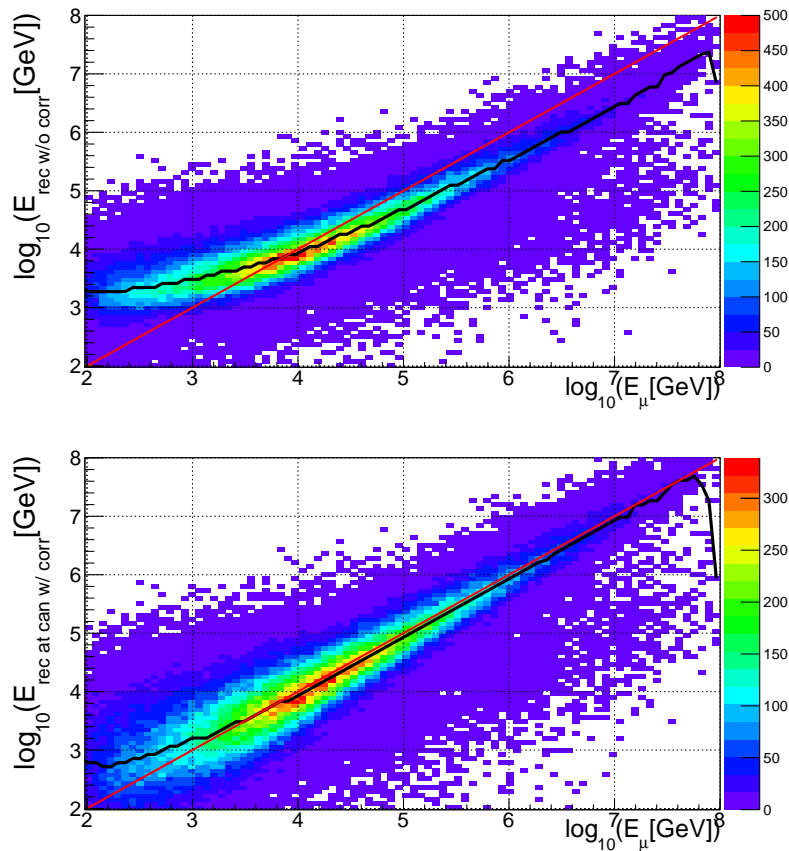


Figure 5.3: Upper panel: Reconstructed energy at the hit barycenter. Lower panel: Corrected reconstructed energy at the can.

The upper panel of Figure 5.3 shows the reconstructed muon energy E_{rec} as a function of the MC muon energy E_{μ} at the can level. The black solid line represents the median of the distribution whereas the red solid line shows the “best case” where $E_{\text{rec}} = E_{\mu}$. The reconstructed energy obtained by JEnergy was “corrected” in another work by performing a linear fit of the median of the distribution of the MC muon energy with respect to the reconstructed energy. The resulting corrected reconstructed energy distribution is shown on the lower panel of Figure 5.3, where the median of the distribution follows closely the $E_{\text{rec}} = E_{\mu}$ function at energies higher than 1 TeV.

A more detailed study is displayed in Figures 5.4, showing the distributions of $\log_{10}(E_{\text{rec}}/E_{\mu})$, with and without the energy correction. In both cases, the energy resolution obtained is about 0.3 units in $\log_{10}(E_{\mu})$ for $10 \text{ TeV} \leq E_{\mu} \leq 100 \text{ PeV}$. In the case where the energy correction was performed, the reconstructed energy E_{rec} is closer to the MC muon energy E_{μ} .

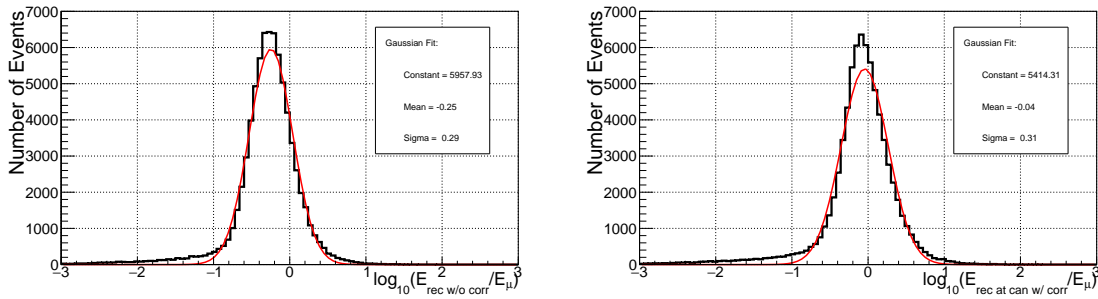


Figure 5.4: Distribution of $\log_{10}(E_{\text{rec}}/E_{\mu})$ with $10 \text{ TeV} \leq E_{\mu} \leq 100 \text{ PeV}$. The red line represents a Gaussian fit. Left panel: Reconstructed energy at the hit barycenter. Right panel: Corrected reconstructed energy at the can.

5.2.2 Angular Resolution

To point back to the neutrino source, a precise estimation of the neutrino direction is needed. For that purpose, the angular resolution is defined as the median of the angular deviation between the direction of reconstructed muon track and the true neutrino direction obtained from the MC.

As mentioned in Chapter 4.2, a cascade-like event exhibits a very dense hit pattern close to the neutrino interaction point, allowing for a good estimate of the neutrino energy but resulting in a poor spatial resolution. For the directional reconstruction

5. PERFORMANCE ANALYSIS

of high-energy neutrinos, the best angular resolution is expected for track-like events. In fact with neutrino energies higher than 100 TeV, an angular resolution of about 0.3° can be achieved (Figure 5.5). Note that, the distribution presented is without any cuts on the reconstruction parameters.

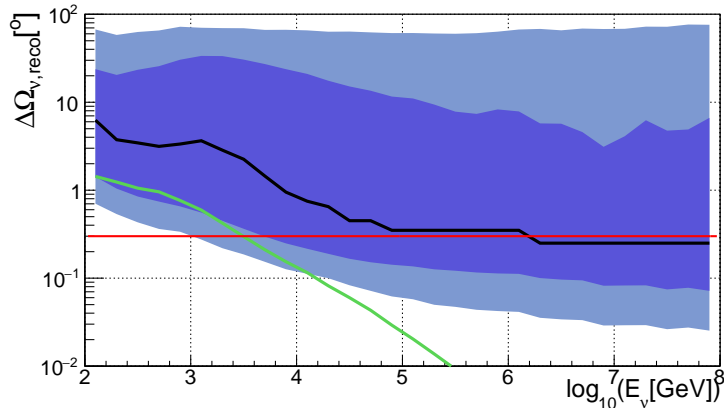


Figure 5.5: Neutrino angular resolution estimated for CC muon neutrinos. The black line represents the median of the distributions and the colored bands represent the 68% and 90% quantiles. The red line represents 0.3° and the green line gives the median angle between the neutrino and true muon direction.

5.3 Search Methods

The primary task of a neutrino telescope is to observe and measure cosmic neutrino events. To foresee the detector sensitivity to a diffuse flux from neutrino cosmic sources, Monte Carlo events have been generated. The MC simulations include both background events and signal events and the goal of the following statistical methods is to search for signal events among the background noise.

The signal and background event distributions are governed by their Probability Density Functions (PDFs). Any difference between the signal and background PDFs provides an opportunity to differentiate events produced by astrophysical sources from background events. The analysis proceeds in the following steps:

1. A pre-selection of the events in order to reject most of the atmospheric background. This step will be performed by setting a cut on the directional parameter provided by the reconstruction algorithm, in this case the reconstructed nadir angle θ_{rec} .

2. A “cut-and-count” analysis method for a fast evaluation of the discovery potential and a rough estimate of the number of signal and background events. This method relies on the maximization of the Model Discovery Potential (MDP) by placing cuts on simulated observables to obtain clean event samples.
3. A maximum likelihood method called the “likelihood ratio test”. The aim of this method is to calculate the discovery potential at different significance levels by using the PDFs of the signal and background events after applying cuts on reconstruction parameters. An optimization process, involving pseudo-experiments and the maximum likelihood ratio for each pseudo-experiment, seeks the selection values for which the discovery flux is best.

5.3.1 Discovery Potential with the Cut-and-Count Method

The cut-and-count method is based on the idea of cutting the number of events and background and searching for an excess of signal events over the background. A poissonian distribution of the events is assumed. The optimization of the signal to background ratio is performed by imposing selection cuts on the reconstruction parameters.

Assuming that a number of events are detected from the cosmic flux, this number is compared to the expected average background using Poisson or binomial statistics. If an excess of events over the background level is observed, it is important to calculate the significance (3σ or 5σ) of this discovery. If no excess is observed (i.e. the null hypothesis), the sensitivity within 90% CL with which this given source flux is excluded can be estimated. The average number of signal events necessary to reject the null hypothesis in a given fraction of trials is the discovery potential. The cuts leading to optimal values for discovery potential and sensitivity will usually be different and have to be found using an optimisation process. Although the cut-and-count method is easy to implement and computationally fast, some criticisms of the methods refer to the fact that all of the event information is reduced to a binary classification, either the event passes the cut and is counted or it is not.

The discovery potential is determined from the number of detected events (n_α) in a given period of time which has a probability α to be background fluctuation. Here the probability α will either be equal to $1.35 \cdot 10^{-3}$ (3σ) or equal to $2.87 \cdot 10^{-7}$ (5σ).

5. PERFORMANCE ANALYSIS

To calculate n_α , the average number of background events $\langle n_b \rangle$ is extracted from the simulation. When $\langle n_b \rangle > 20$, a square root function is sufficient to compute n_α . In Figure 5.6, $\langle n_b \rangle$ and the corresponding n_α are shown. Considering diffuse neutrino fluxes, the number of background events will easily be higher than 20.

By introducing $n_{crit} = \langle n_b \rangle + \langle n_s \rangle$ as the smallest number of events needed to claim a detection with a p-value less than α in a fraction $1 - \beta$ of the experiments, then the signal strength n_α is the value that fulfils

$$\begin{aligned} P(\geq n_{crit} | \langle n_b \rangle + n_s) &= \sum_{n_{obs}=n_{crit}}^{\infty} P(n_{obs} | \langle n_b \rangle + n_\alpha) \\ &= 1 - \sum_{n_{obs}=0}^{n_{crit}-1} P(n_{obs} | \langle n_b \rangle + n_\alpha) \\ &= 1 - \beta \end{aligned}$$

Thus given a source spectrum Φ_s predicting $\langle n_s \rangle$ signal events in a set observation time, the minimum flux Φ_α needed for a discovery with significance α is

$$\Phi_\alpha = \Phi_s \times \frac{n_\alpha(\langle n_b \rangle)}{\langle n_s \rangle} \quad (5.4)$$

where the second term is called the Model Discovery Factor (MDF).

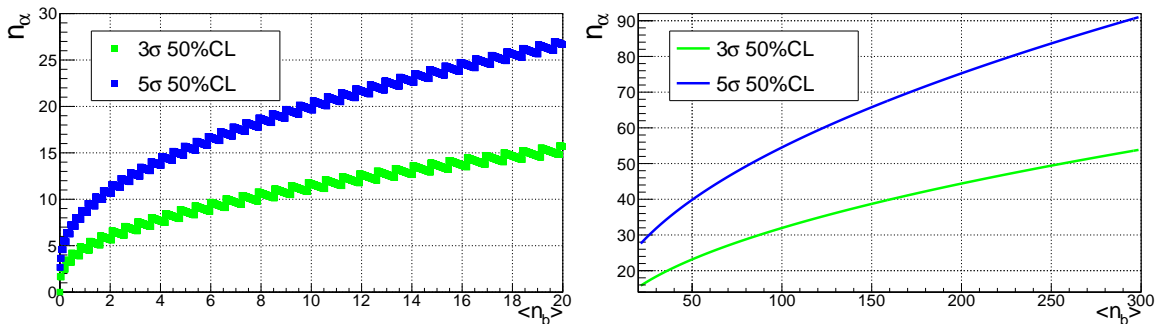


Figure 5.6: The number of events required for a 3σ or a 5σ discovery as a function of the average number of background events.

5.3.2 Sensitivity with the Cut-and-Count Method

In a search to quantify the sensitivity of an experiment, independently of experimental data (104), Feldman and Cousins (105) have proposed the following method. The

average upper limit at 90% confidence level (CL) is computed by using the number of events observed (n_{obs}) and the average number of background events expected ($\langle n_b \rangle$).

$$\bar{\mu}_{90}(\langle n_b \rangle) = \sum_{n_{obs}}^{\infty} \mu_{90}(n_{obs}, n_b) \frac{(n_b)^{n_{obs}}}{n_{obs}!} e^{-n_b} \quad (5.5)$$

where μ_{90} is the Feldman-Cousins upper limit and the second term is the weight of the Poisson probability of occurrence. $\bar{\mu}_{90}$ is reported as a function of the average number of background events $\langle n_b \rangle$ in Figure 5.7.

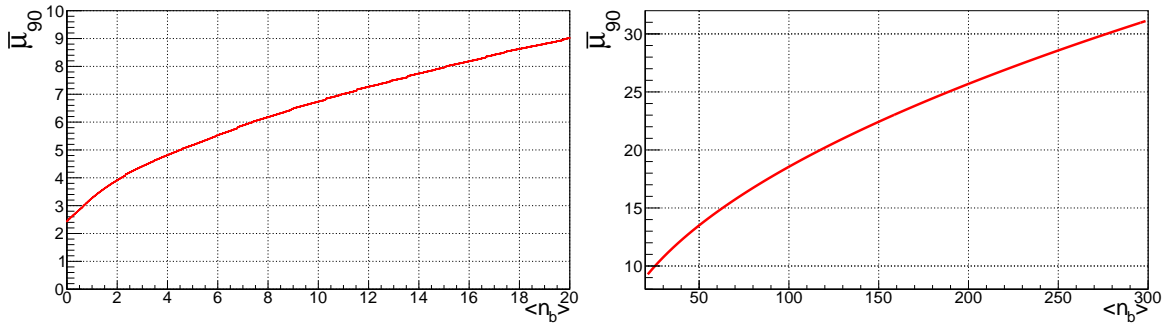


Figure 5.7: $\bar{\mu}_{90}$ as a function of the average number of background events.

If a source model Φ_s predicts a mean number of signal events $\langle n_s \rangle$, the average flux limit Φ_{90} is found by scaling the normalisation of the flux model such that the number of expected events equals the average upper limit

$$\Phi_{90} = \Phi_s \times \frac{\bar{\mu}_{90}(\langle n_b \rangle)}{\langle n_s \rangle} \quad (5.6)$$

where the second term is the Model Rejection Factor (MRF). So in order to place the best upper limit on the signal from the assumed theoretical model, selection criteria must be optimized.

5.3.3 Likelihood Ratio Test

The likelihood ratio test relies on the maximization of the likelihood derived from the PDFs assigned to the signal and background events. When the set of events is compatible with two different hypotheses (H_0 and H_1), a test statistic needs to be performed. Assuming that $H_0 = H_b$ is the condition that the data set consist only of background events and $H_1 = H_{s+b}$ is the case that signal events are also present

5. PERFORMANCE ANALYSIS

to the background, the Likelihood Ratio (LR) test is the ratio of the probabilities such that H_{s+b} is the correct hypothesis over H_b

$$LR = \log \frac{\prod_{i=1}^n P(x_i|H_{s+b})}{\prod_{i=1}^n P(x_i|H_b)} = \sum_{i=1}^n \log \frac{P(x_i|H_{s+b})}{P(x_i|H_b)} \quad (5.7)$$

The probabilities for each event x_i are defined as

$$\begin{aligned} P(x_i|H_{s+b}) &= \frac{n_s}{n} \times P_s(X_i) + \left(1 - \frac{n_s}{n}\right) \times P_b(X_i) \\ P(x_i|H_b) &= P_b(X_i) \end{aligned} \quad (5.8)$$

where n_s is the number of signal events in the sample of $n = n_s + n_b$ events, $P_s(X_i)$ and $P_b(X_i)$ are the PDFs for the signal and the background respectively; they are functions of one or more parameters X_i . The resulting LR function is then

$$LR = \sum_{i=1}^n \log \frac{\frac{n_s}{n} \times P_s(X_i) + \left(1 - \frac{n_s}{n}\right) \times P_b(X_i)}{P_b(X_i)} \quad (5.9)$$

The output of the algorithm is then the maximized LR value and the corresponding fitted n_s value. The logarithm of this likelihood ratio can be used to compute a p-value to decide whether to reject the null model H_b in favor of H_{s+b} . To do so, this procedure is applied to many samples (or pseudo-experiments) of background only events obtained by MC simulations of atmospheric backgrounds. For each sample, the maximum value of LR is recorded. The distribution of LR_{bkgd}^{max} is equivalent to $P(\lambda|H_0)$ in Figure 5.8. Therefore setting the required significance (e.g 3σ or 5σ), the critical value is calculated such that:

$$\int_{LR_{3\sigma}}^{+\infty} LR_{bkgd}^{max} = 1.35 \times 10^{-3} \quad \text{and} \quad \int_{LR_{5\sigma}}^{+\infty} LR_{bkgd}^{max} = 2.87 \times 10^{-7} \quad (5.10)$$

This procedure is then repeated, gradually adding a number of simulated signal events to the sample of background events. Here the values of LR_{signal}^{max} give the $P(\lambda|H_1)$ in Figure 5.8. The green area is the probability of rejecting H_b , also called the significance level; whereas the yellow area represents the ‘‘power’’ region, also called the confidence level that H_{s+b} is true.

$$\int_{LR_{3\sigma,5\sigma}}^{+\infty} LR_{signal}^{max} = power \quad (5.11)$$

If $n_{3\sigma,5\sigma}$ is the number of simulated signal events such that the power reaches 50%, then $n_{3\sigma,5\sigma}$ represents the number of events that lead to an observation with a p-value less than 3σ or 5σ respectively with a 50% Confidence Level (CL).

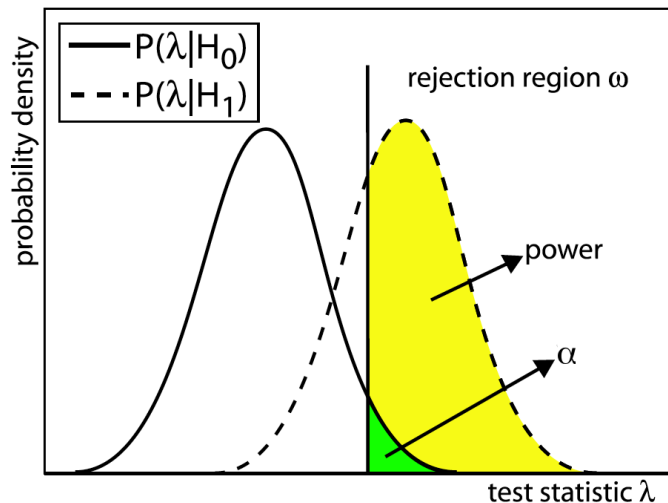


Figure 5.8: Illustration of hypothesis testing. The PDFs of the test statistic for H_0 and H_1 are shown. The rejection region ω is the region to the right of the vertical line. The green area is the significance level α for H_0 and the yellow area is the confidence level for H_1 .

If the analysis has been performed with a model for the source that predicts a flux Φ_s and a mean number of signal events $\langle n_s \rangle$, the discovery flux is

$$\Phi_\alpha = \Phi_s \times \frac{n_\alpha(\langle n_b \rangle)}{\langle n_s \rangle} \quad (5.12)$$

where α is the required significance level.

5.4 Results

5.4.1 Event Generation

In this analysis, two full sky spectra are chosen for astrophysical origin. These spectra are applied as a result of the IceCube results for an isotropic, flavor-symmetric neutrino flux. The neutrino diffuse fluxes have been generated with energies between 10^2 and 10^8 GeV and the assumed IceCube neutrino one-flavor fluxes are described in Equations 3.12 and 3.13 (in Chapter 3.3.3). The cosmic fluxes are assumed isotropic and the atmospheric neutrino background is also simulated in the energy range of 10^2 to 10^8 GeV and over the whole sky. As mentioned in Chapter 4.1.2, they follow the Honda model (78) for the conventional atmospheric flux and the Enberg model (83) for prompt atmospheric flux, with the cosmic-ray knee correction. The atmospheric

5. PERFORMANCE ANALYSIS

muon background implemented come from two sets of atmospheric muon bundles (see Chapter 4.1.3). One set with an energy threshold $E_{th} > 10$ TeV and making up about four months worth of events. The other set with an energy threshold $E_{th} > 50$ TeV and accumulating more than 2 years worth of events.

5.4.2 Pre-Selection Cut

In order to reduce the large amount of misreconstructed downgoing muons and atmospheric neutrinos, and to select the cosmic neutrino events in the data samples, some parameter cuts have to be applied to reconstructed events. The calculated sensitivity and discovery potential are optimized with cuts on the reconstructed nadir angle (θ_{rec}), the reconstructed energy (E_{rec}), the number of hits (N_{hit}), the likelihood (Lik) and the error on the track's angular parameters (β).

A small number of neutrino events need to be isolated from a large background of atmospheric muons. Already by selecting the events reconstructed as upgoing, most of the atmospheric muon background will be rejected and only the badly reconstructed events will survive the cut on the nadir angle. The likelihood and β are related to the quality of the reconstruction (see Chapter 4.2.2), therefore putting cuts on these parameters will reduce the badly reconstructed atmospheric muons. N_{hit} and E_{rec} are related to the energy of the reconstructed event and thus help to reject atmospheric neutrinos, which are expected to have a softer spectrum than that of cosmic events.

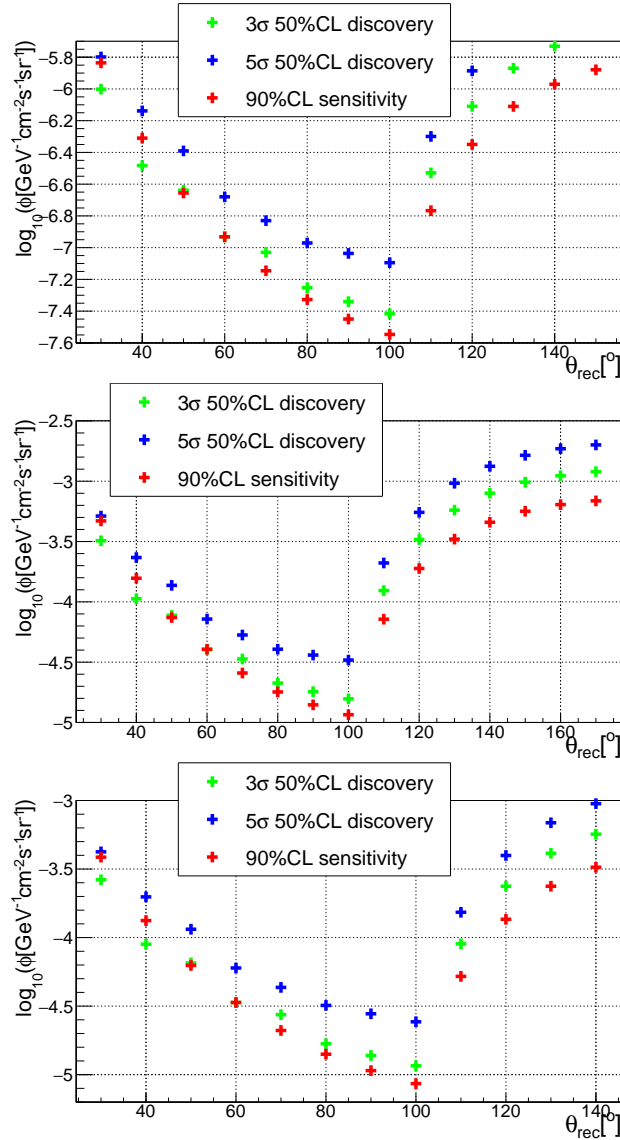


Figure 5.9: Flux normalization factor (explained afterward) expected for various θ_{rec} and evaluated for 1 year. Upper panel: E^{-2} spectrum with a 3 PeV cutoff. Center panel: $E^{-2.5}$ spectrum with a 3 PeV cutoff. Lower panel: $E^{-2.5}$ spectrum without any cutoff.

It was first chosen to put a preliminary cut on θ_{rec} and to simultaneously change the cuts on E_{rec} , N_{hit} , Lik and β in order to optimize the MDF and MRF. Simply by using the Earth as a filter, it is possible to remove most cosmic-ray induced muons while retaining as many neutrino-induced events as possible. Therefore, by rejecting events coming from above the horizon (downgoing events) most of the atmospheric muons will be removed. As can be seen in Figure 5.9, using the cut-and-count method, the flux normalization factor, which will be explained in Chapter 5.4.3, reaches its

5. PERFORMANCE ANALYSIS

minimum when the reconstructed nadir angle θ_{rec} is less than 100° . Applying this cut means that the events which have been properly reconstructed with a nadir angle higher than 100° will be rejected (red area in Figure 5.10). The number of remaining events are reported in Table 5.1. This pre-selection cut on the reconstructed nadir angle ($\theta_{\text{rec}} \leq 100^\circ$) will be applied throughout the rest of this analysis.

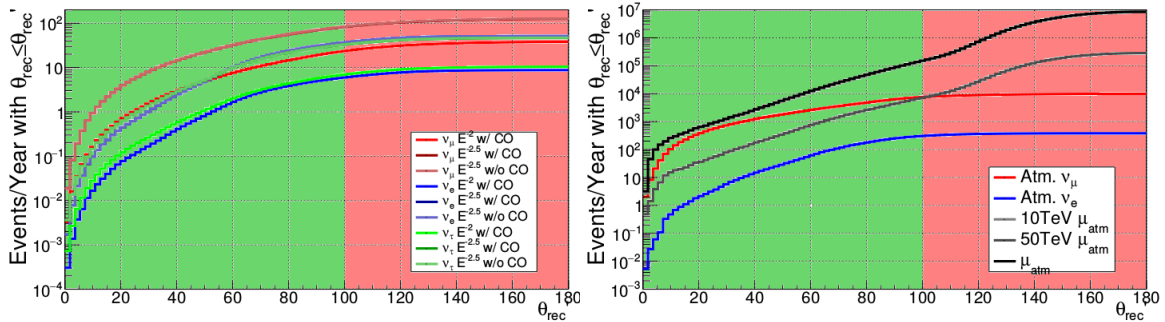


Figure 5.10: Cumulative distributions of θ_{rec} with the cosmic events in the left panel and the atmospheric events in the right panel. The black line represents the sum of both the 10 TeV and 50 TeV atmospheric muons.

			Reconstruction level	Pre-selection cut
Atm.	Muons	10 TeV	$8.28 \cdot 10^6$	$1.39 \cdot 10^5$
		50 TeV	$2.83 \cdot 10^5$	$6.84 \cdot 10^3$
	Neutrinos	ν_μ	$9.93 \cdot 10^3$	$7.50 \cdot 10^3$
		ν_e	380.75	301.60
Cosm.	E^{-2} spectrum	ν_μ	37.85	23.20
		ν_e	8.76	5.89
		ν_τ	10.43	6.85
	$E^{-2.46}$ w/ CO	ν_μ	124.70	81.23
		ν_e	51.13	36.24
		ν_τ	46.54	32.35
	$E^{-2.46}$ w/o CO	ν_μ	127.80	82.98
		ν_e	51.55	36.39
		ν_τ	47.14	32.71

Table 5.1: Number of events expected for 1 year of observation time with and without the reconstructed nadir angle selection. The cosmic events are derived from the IceCube fluxes in Equations 3.12, 3.13 and 3.14 .

5.4.3 Results from the Cut-and-Count Method

The discovery flux $\Phi_\alpha(E_\nu)$ and the sensitivity flux $\Phi_{90}(E_\nu)$ have the same functional dependence on the energy as the source flux, but contain different normalization factors ϕ_α and ϕ_{90} respectively. Therefore

$$\Phi_{90/\alpha}(E_\nu) = \phi_{90/\alpha} \left(\frac{E_\nu}{\text{GeV}} \right)^{-2} \cdot \exp \left(-\frac{E_\nu}{3\text{PeV}} \right) \quad (5.13)$$

where $\phi_{90/\alpha}$ is the flux normalization factor. Although this equation was incentivized by the IceCube E^{-2} spectrum with a 3 PeV cutoff from Equation 3.12 (see Chapter 3.3.3), it will also be applied assuming the IceCube $E_\nu^{-2.46}$ spectra, with or without a cutoff, in Equations 3.13 and 3.14. Considering Equations 5.4 and 5.6, here $\phi_{90/\alpha}$ is directly linked to the MDF and MRF. The goal here is to minimize the latter by applying the appropriate selection cuts on some of the reconstruction parameters.

After the pre-selection cut discussed in 5.4.2, the minimization process was performed on four reconstruction parameters: E_{rec} , N_{hit} , Lik and β . This procedure was carried out for an observation time of 20 years. The resulting normalization flux $\phi_{90/\alpha}$ as a function of the observation time have been reported in Figure 5.11. These results are compared to the previously mentioned IceCube neutrino diffuse fluxes (dashed black lines) and to the $\phi_{5\sigma}$ discovery potential of the second construction phase of the ARCA detector (2 blocks of 115 DUs each) expected after 1 year of observation time (17). They are also compared to the $\phi_{90\%CL}$ upper-limit obtained with ANTARES using 2450 days worth of data (106), imposing a zenith cut at 90° and a cut on an energy estimator based on Artificial Neural Networks (107).

Thus from Figure 5.11, it is possible to establish that the IceCube diffuse neutrino flux with a E^{-2} spectrum can be attained within 6 years at 3σ 50%CL and about 15 years at 5σ 50%CL. Instead, with a $E^{-2.46}$ spectrum without cutoff, the IceCube diffuse neutrino flux can be attained within 5 years at 3σ 50%CL and 13 years at 5σ 50%CL. Finally, with a $E^{-2.46}$ spectrum with cutoff, the IceCube diffuse neutrino flux can be expected within 7 years at 3σ 50%CL and about 18 years at 5σ 50%CL.

5. PERFORMANCE ANALYSIS

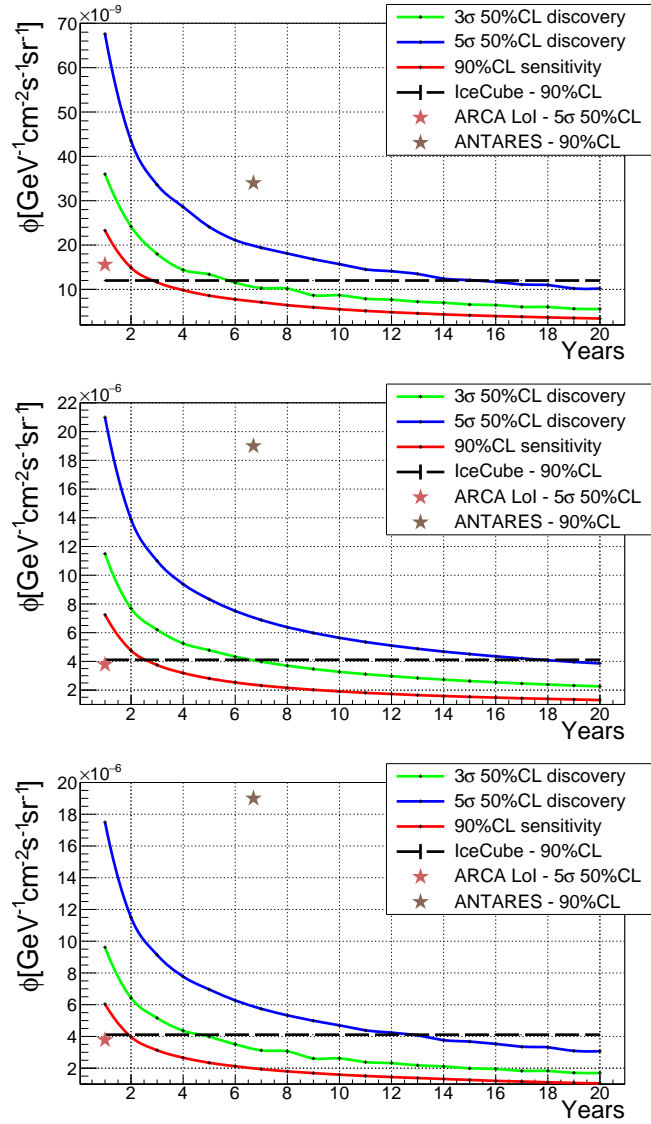


Figure 5.11: Flux normalization factors over an observation time of 20 years. The dashed black line represents each of the respective IceCube diffuse fluxes. The pink star represents the $\phi_{5\sigma}$ discovery potential expected from the ARCA Phase-2 detector within 1 year and the brown star represents the $\phi_{90\%CL}$ upper limit obtained with ANTARES using 6.7 years worth of data. Upper panel: considering an E^{-2} spectrum with a 3 PeV cutoff. Center panel: considering an $E^{-2.46}$ spectrum with a 3 PeV cutoff. Lower panel: considering an $E^{-2.46}$ spectrum without any cutoff.

Furthermore a quick analysis is performed regarding the choice of the $E^{-2.46}$ spectrum to confirm the initial statement (see Chapter 3.3.3) that the $E^{-2.46}$ spectrum is preferable without the 3 PeV cutoff. In Figure 5.12, the ratios between the normalization flux with and without the cutoff are shown, with $\phi_{\alpha}^{\text{w/CO}} \simeq 2.195 \cdot \phi_{\alpha}^{\text{w/oCO}}$ and $\phi_{90}^{\text{w/CO}} \simeq 2.193 \cdot \phi_{90}^{\text{w/oCO}}$. From these results, is it possible to concur that a better

normalization flux is expected for the $E^{-2.46}$ spectrum without the 3 PeV cutoff.

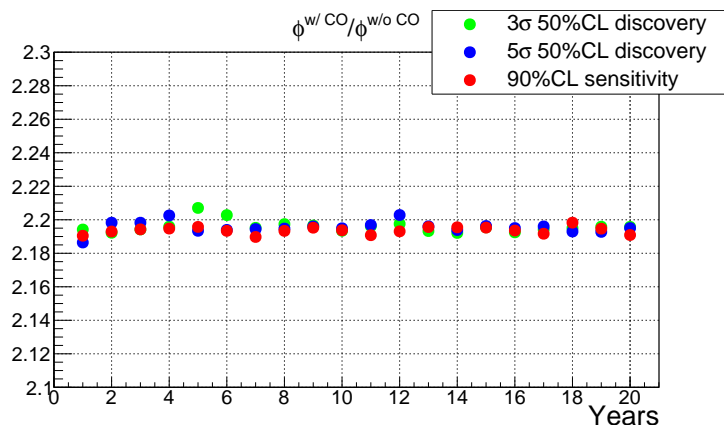


Figure 5.12: Ratio between the a $E^{-2.5}$ spectrum with cutoff (w/ CO) flux normalization factor and a $E^{-2.5}$ spectrum without (w/o CO) cutoff flux normalization factor.

In spite of the limitation of the cut-and-count method, by optimizing the cuts on the reconstruction parameters, a decent discovery flux can already be expected for this first construction phase of the ARCA detector. It can be assumed that by applying a more performant statistical method, even better results can be anticipated.

5.4.4 Results from the Likelihood Ratio test

The Likelihood Ratio (LR) test is now performed on the data set. The key ingredient for this method are the Probability Density Functions (PDFs) for the signal and the background as a function of our selection of quality parameters.

In addition, another important step in this procedure is to prepare the background event samples to be analyzed. To obtain an accurate result many samples are needed, this ramps up the time required to process the analysis. Nevertheless, 10000 samples have been used. Each sample contains a number of events corresponding to the number of atmospheric background expected in a given period of time. Unlike in the cut-and-count method, which is based on a “cut and count” approach, in this method the cuts were first applied on the data set and then the LR test is performed on the resulting PDF, as the aim is to find the cuts that minimize the discovery flux. As mentioned before, this statistical method is quite performant when it comes to discriminating between signal and background events. The main downside is the

5. PERFORMANCE ANALYSIS

CPU run time required to perform the LR test on the collection of PDFs, obtained by enforcing various reconstruction parameter cuts (after having already applied the pre-selection cut on the nadir angle).

Over a two year period, for both the E^{-2} spectrum with the 3 PeV cutoff and the $E^{-2.46}$ spectrum without any cutoff, the best cut was found for $\beta \leq 10^{-2.4}$ degrees and $E_{\text{rec}} \geq 10^{3.5}$ GeV. The normalized distribution of the likelihood parameter for the selected events has been chosen as PDF. These distributions are shown in Figure 5.13, for both the cosmic events and the atmospheric background events.

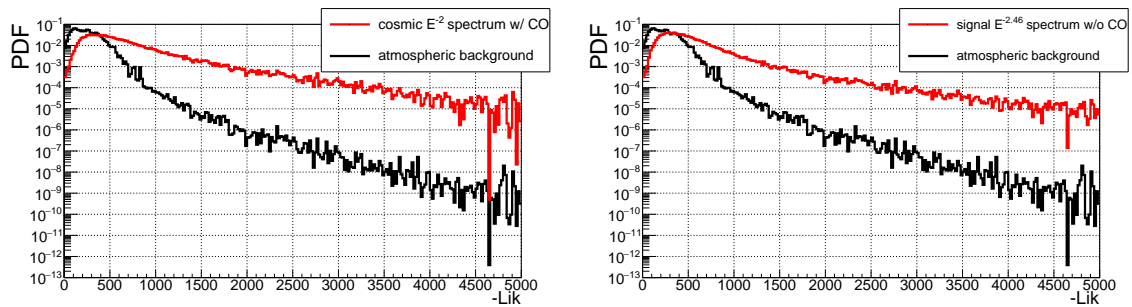


Figure 5.13: Likelihood PDF for the cosmic events (red line) and for the atmospheric events (black line) for events that passed the pre-selection cut ($\theta_{\text{rec}} \leq 100^\circ$), the β cut and the E_{rec} cut. Left panel: based on the E^{-2} spectrum with cutoff. Right panel: based on the $E^{-2.46}$ spectrum without cutoff. The distribution presented are with the best cuts on the β track quality parameter and the reconstructed energy E_{rec} simultaneously.

Each background sample contains the sum of the atmospheric background events (184.48 atmospheric neutrinos and 2423.36 atmospheric muons for the E^{-2} spectrum, and 636.66 atmospheric neutrinos and 3807.19 atmospheric muons for the $E^{-2.46}$ spectrum) provided after pre-selection cut and the reconstruction parameter cuts have been enforced. After executing the previously defined LR test on the PDFs, the maximum value of LR (LR^{max}) is stored for each sample and the integral of the cumulative distribution of LR^{max} is shown in Figure 5.14. This plot shows for each value of LR_i^{max} the integral of the normalized LR^{max} distribution for $LR^{\text{max}} > LR_i^{\text{max}}$. This distribution is fitted to an exponential function (red line) and the values of LR^{max} corresponding to a 5σ and a 3σ significance of the test statistic are indicated. The value of $LR_{3\sigma}$ can be extracted directly from the histogram while $LR_{5\sigma}$ is extrapolated from the exponential fitting.

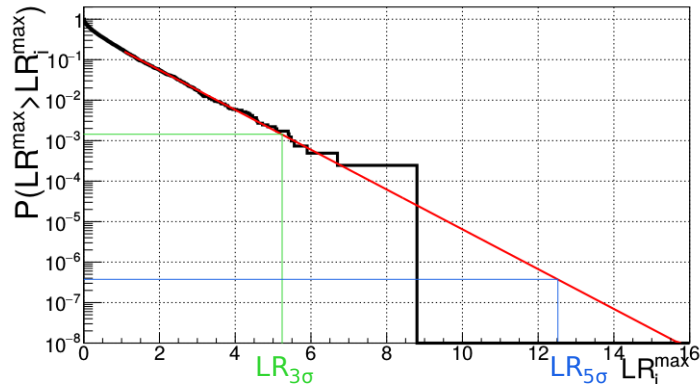


Figure 5.14: Cumulative distribution of the LR^{max} value extracted during the analysis. The red line is the exponential function which fits the histogram. The values corresponding to the 3σ and the 5σ significance of the test statistic are shown.

The procedure is then repeated adding to the sample of background events a number N_{signal} of simulated signal events. The distribution of LR^{max} and n_{sig} obtained after maximisation of Equation 5.9 are shown in Figure 5.15 for different values of N_{signal} . The integrals for $LR^{max} > LR_{3\sigma}$ and for $LR^{max} > LR_{5\sigma}$ give the probabilities, $P_{3\sigma}$ and $P_{5\sigma}$, of making a discovery at the 3σ and 5σ significance level. $P_{3\sigma}$ and $P_{5\sigma}$ are shown in Figure 5.16 as a function of N_{signal} during a 2 year period.

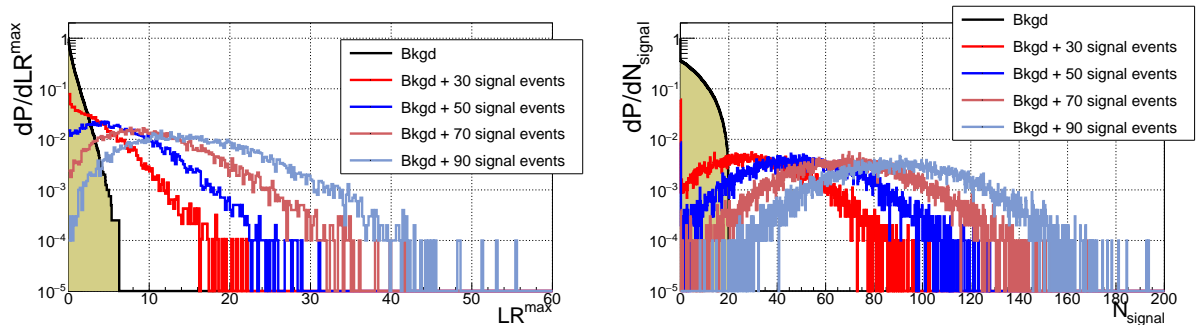


Figure 5.15: Left panel: LR^{max} distribution. Right panel: Fitted number of signal events.

Requiring that $P_{3\sigma} = P_{5\sigma} = 50\%$, the corresponding values $n_{3\sigma} = 44.77$ and $n_{5\sigma} = 76.60$ represent the number of events that lead to an observation with a p-value less than 3σ and 5σ , respectively, in 50% of the experiments. The corresponding

5. PERFORMANCE ANALYSIS

discovery fluxes are thus

$$\phi_{3\sigma} = 1.2 \times 10^{-8} \frac{44.77}{2 \times 14.60} = 1.84 \times 10^{-8} \text{ GeV}^{-1} \text{ s}^{-1} \text{ cm}^{-2} \quad (5.14)$$

$$\phi_{5\sigma} = 1.2 \times 10^{-8} \frac{76.60}{2 \times 14.60} = 3.15 \times 10^{-8} \text{ GeV}^{-1} \text{ s}^{-1} \text{ cm}^{-2} \quad (5.15)$$

where 14.60 represents the number of signal events (per year) remaining after the previously mentioned parameter cut ($\theta_{\text{rec}} \leq 100^\circ$, $\beta \leq 10^{-2.4}$ degrees and $E_{\text{rec}} \geq 10^{3.5}$ GeV).

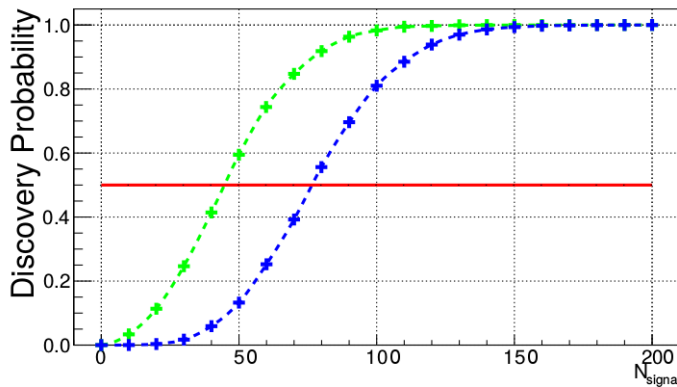


Figure 5.16: Probability for a 3σ and 5σ discovery as a function of the number of signal events added to each background sample. The horizontal red line corresponds to the probability to make a discovery in 50% of the pseudo-experiments.

These procedures are repeated using different values of the reconstruction parameter cuts until the smallest ϕ is obtained. For both the E^{-2} spectrum with the 3 PeV cutoff and the $E^{-2.46}$ spectrum without any cutoff, the best results were found for $\beta \leq 10^{-2.4}$ degrees and $E_{\text{rec}} \geq 10^{3.5}$ GeV. Other p-values were also investigated (from 2σ to 6σ) up to 20 observation years for the E^{-2} spectrum and 15 observation years for the $E^{-2.46}$ spectrum. The results are shown in Figure 5.17.

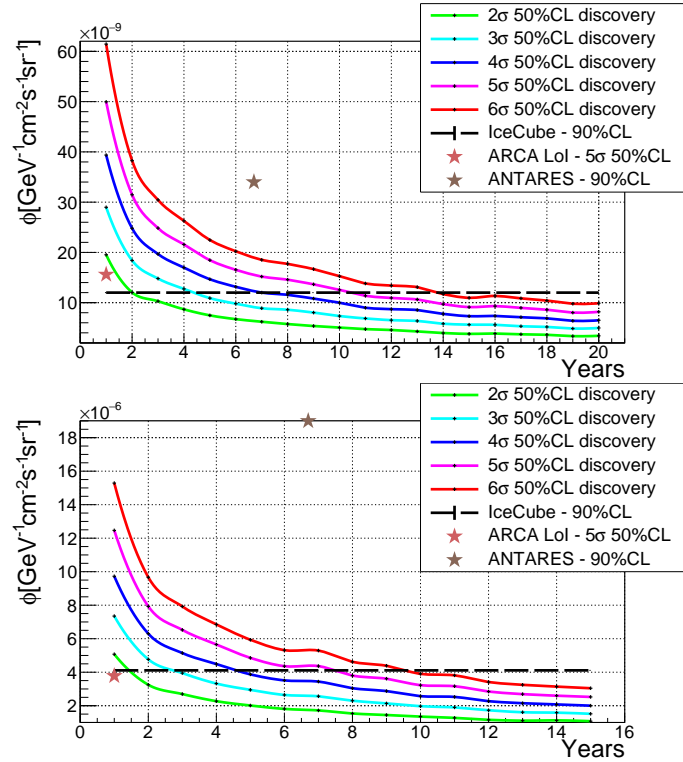


Figure 5.17: Flux normalization factors expected with $\beta \leq 10^{-2.4}$ degrees and $E_{\text{rec}} \geq 10^{3.5}$ GeV. They are shown while considering many p-values. Upper panel: for a E^{-2} spectrum over an observation period of 20 year. Lower panel: for a $E^{-2.46}$ spectrum over an observation period of 15 year. The dashed black line represents each of the respective IceCube diffuse fluxes. The pink star represents $\phi_{5\sigma}$ discovery potential expected from the ARCA Phase-2 detector within 1 year and the brown star represents the $\phi_{90\%CL}$ upper limit obtained with ANTARES with 6.7 years worth of data.

Figure 5.18 undeniably shows that the results using this LR method yields better results compared to the cut-and-count method. Indeed, with this method, the normalization flux factor ϕ_α can be 10% to 20% better for the E^{-2} spectrum and 20% to 30% better for the $E^{-2.46}$ spectrum, depending on the year. Consequently, the IceCube diffuse neutrino flux with a E^{-2} spectrum can be attained within about 4 years at 3σ 50%CL and about 10 years at 5σ 50%CL, and the IceCube diffuse neutrino flux with a $E^{-2.46}$ spectrum can be attained within 3 years at 3σ 50%CL and about 7 years at 5σ 50%CL.

5. PERFORMANCE ANALYSIS

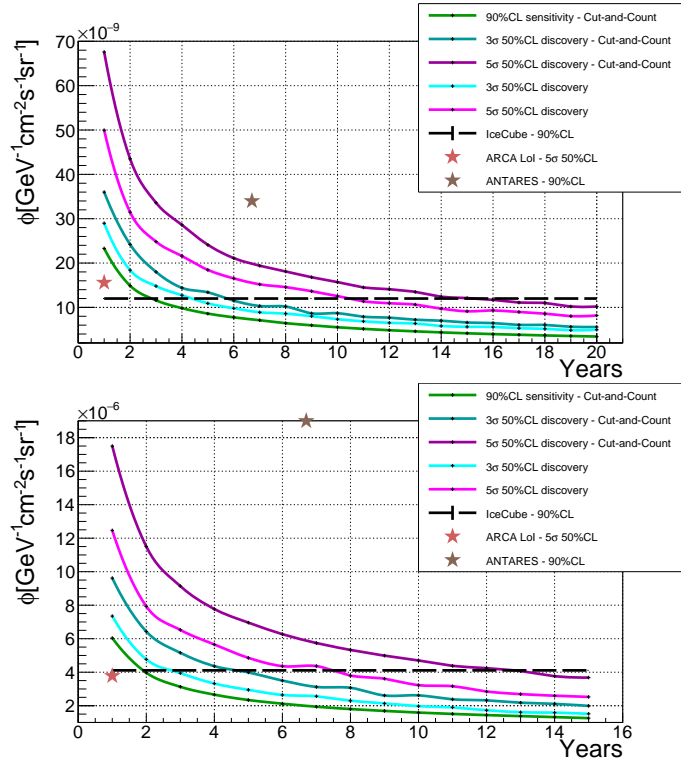


Figure 5.18: Flux normalization factors expected with $\beta \leq 10^{-2.4}$ degrees and $E_{\text{rec}} \geq 10^{3.5}$ GeV. They are compared to the previous cut-and-count results. Upper panel: for a E^{-2} spectrum over an observation period of 20 year. Lower panel: for a $E^{-2.46}$ spectrum over an observation period of 15 year. The dashed black line represents each of the respective IceCube diffuse fluxes. The pink star represents $\phi_{5\sigma}$ discovery potential expected from the ARCA Phase-2 detector within 1 year and the brown star represents the $\phi_{90\%CL}$ upper limit obtained with ANTARES with 6.7 years worth of data.

5.4.5 Resulting Energy and Angular Resolution

Enforcing the cuts previously obtained, the angular and energy resolution can be re-evaluate. Figure 5.19 shows a net improvement on these two detector performance estimators. Applying the pre-selection cut ($\theta_{\text{rec}} \leq 100^\circ$) and some of the resulting cuts from the cut-and-count method ($\text{Lik} \leq -425$ and $\beta \leq 10^{-2.3}$ degrees), an angular resolution of 0.15° is attained and the energy resolution obtained is about 0.24 units in $\log_{10}(E_\mu)$ for events with $E_\mu \geq 10$ TeV.

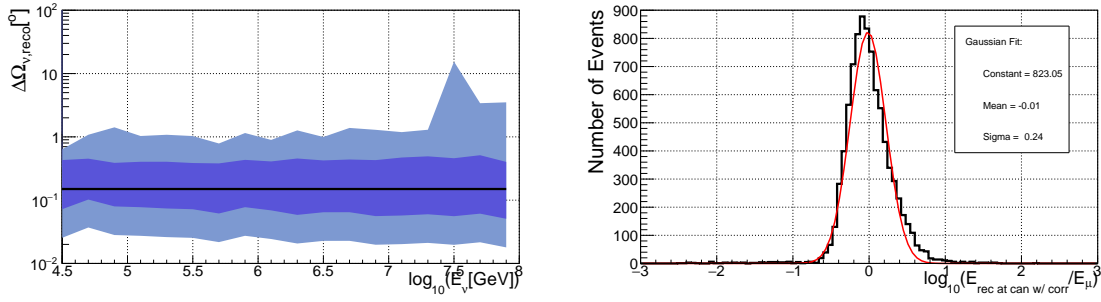


Figure 5.19: Left panel: Neutrino angular resolution estimated for CC muon neutrinos and for $\text{Lik} \leq -425$ and $\beta \leq 10^{-2.3}$ degrees. The black line represents the median of the distributions and the colored bands represent the 68% and 90% quantiles. Right panel: Distribution of $\log_{10}(E_{\text{reco}}/E_\mu)$ for events with $E_\mu \geq 10$ TeV, considering the corrected reconstructed energy. The red line represents a Gaussian fit.

The angular resolution with the cuts from the LR method yield worse results (0.25°) as a likelihood cut is not applied, making it more probable for the selected events to include misreconstructed events. Furthermore the results are quite biased by the cut on the reconstructed energy. When considering the energy resolution, the bias becomes undeniable. Although the resolution obtained is only slightly worsen (0.26 units in $\log_{10}(E_\mu)$), the reconstructed energy E_{rec} is clearly diverging from the MC muon energy E_μ . This is visible in Figure 5.20.

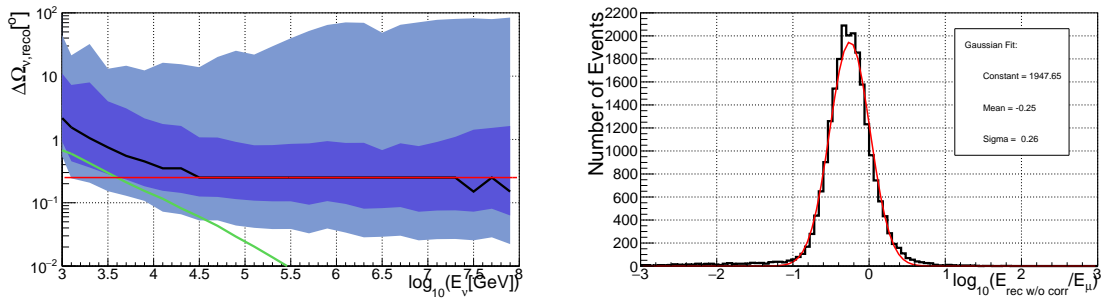


Figure 5.20: Left panel: Neutrino angular resolution estimated for CC muon neutrinos and for $\beta \leq 10^{-2.4}$ degrees and $E_{\text{rec}} \geq 10^{3.5}$ GeV. The black line represents the median of the distributions and the colored bands represent the 68% and 90% quantiles. The red line represents 0.25° and the green line gives the median angle between the neutrino and true muon direction. Right panel: Distribution of $\log_{10}(E_{\text{reco}}/E_\mu)$ for events with $E_\mu \geq 10$ TeV, considering the corrected reconstructed energy. The red line represents a Gaussian fit.

5. PERFORMANCE ANALYSIS

The number of events expected for one year of observation with the cuts from both previous method, including those chosen for the energy and angular resolution, are enclosed in Table 5.2. A choice was made out of a range of minimizing cuts in 5.4.3, corresponding to $\text{Lik} \leq -425$, $\beta \leq 10^{-2.3}$ degrees, $E_{\text{rec}} \geq 10^{4.8}$ GeV and $N_{\text{hit}} \geq 125$.

			Cuts from 5.4.3	Cuts from 5.4.4	Resolution cuts	Cuts from (17)
Atm.	Muons	10 TeV	0	3208.47	0	44.48
		50 TeV	0	598.71	0	3.35
	Neutrinos	ν_{μ}	2.83	629.68	6.42	498.54
		ν_e	0.06	6.98	0.13	0.26
Cosm.	E^{-2} spectrum	ν_{μ}	1.73	10.59	2.19	3.75
		ν_e	0.21	1.79	0.28	0.10
		ν_{τ}	0.25	2.22	0.33	0.38
	$E^{-2.46}$ w/o CO	ν_{μ}	2.07	24.44	2.91	10.09
		ν_e	0.3	4.77	0.44	0.16
		ν_{τ}	0.3	5.02	0.44	0.85

Table 5.2: Number of events expected for 1 year of observation time with the cuts obtained from the cut-and-cout method and the LR method, and those used for the energy and angular resolution presented in this Chapter 5.4.5. The cosmic events are derived from the IceCube fluxes in Equations 3.12 and 3.13.

Even if the detector is smaller and the event selection is different, the energy resolution for the first phase of ARCA is comparable with ARCA 115 DUs (1 block) (17). Furthermore, the same cuts applied in (17) ($\text{Lik} \leq -60$ and $\beta \leq 10^{-2.8}$ degrees) were applied to the data set used in this work. The resulting angular and energy resolutions are shown in Figure 5.21, in which the angular resolution above 50 TeV is also 0.15° and the energy resolution is slightly worse, at about 0.25 units in $\log_{10}(E_{\mu})$ for events with $E_{\mu} \geq 10$ TeV. Furthermore, the number of events expected for one year of observation with these cuts are also included in Table 5.2.

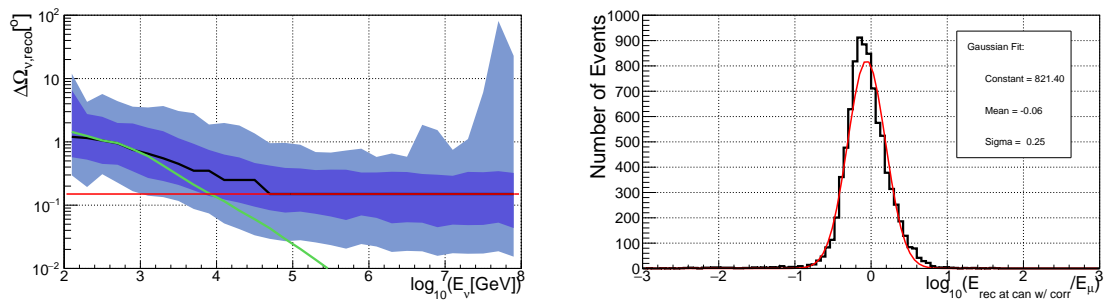


Figure 5.21: Left panel: Neutrino angular resolution estimated for CC muon neutrinos and for $\text{Lik} \leq -60$ and $\beta \leq 10^{-2.8}$ degrees. The black line represents the median of the distributions and the colored bands represent the 68% and 90% quantiles. The red line represents 0.15° and the green line gives the median angle between the neutrino and true muon direction. Right panel: Distribution of $\log_{10}(E_{reco}/E_{\mu})$ for events with $E_{\mu} \geq 10$ TeV, considering the corrected reconstructed energy. The red line represents a Gaussian fit.

5. PERFORMANCE ANALYSIS

CONCLUSION

The ARCA detector of KM3NeT will be the next generation km³-scale neutrino detector to be installed in the Mediterranean Sea. One of the main aims is to explore the IceCube signal from a different field of view, with an improved angular resolution and different systematic uncertainties, by making use of its grid of thousands of sensitive multi-PMT optical sensors. The collected photon arrival times and the spatial positions of its digital optical modules are used to reconstruct the direction of the neutrinos and to associate them with potential distant cosmic sources.

The complete ARCA detector will consist of two building blocks with 115 strings each, adding up to an instrumented volume of about 1 km³. The first construction phase of ARCA will consist of 24 strings, which instead amounts to an instrumented volume of about 0.1 km³. The aim of this work was to evaluate the detector performances of the first construction phase of ARCA through a complete Monte Carlo simulation and a track-like reconstruction algorithm. The work focuses on the search for neutrino signal events from a diffuse neutrino flux by selecting the upgoing muon tracks which cross the detector volume.

Using two different approaches, the detector sensitivity (flux which can be excluded at 90% CL) and discovery potential (flux which can be detected at 3σ or 5σ above the background noise) for two isotropic diffuse neutrino fluxes were evaluated. One assuming a E^{-2} spectrum with a 3 PeV cutoff and the other assuming a $E^{-2.46}$ spectrum, without any cutoff. The observation time required for the discovery of the benchmark E^{-2} spectrum from a diffuse neutrino flux at 3σ 50%CL is about 4 years and about 10 years at 5σ 50%CL. On the other hand, with an observation time of 3 years, a $E^{-2.46}$ spectrum could be obtained at 3σ 50%CL and about 7 years at 5σ 50%CL.

The reconstruction of the muon tracks with respect to the direction of the incident

5. PERFORMANCE ANALYSIS

muon neutrinos is performant enough to achieve an angular resolution better than 0.15° at high energies (above 10 TeV) and the energy resolution obtained is about 0.24 units in $\log_{10}(E_\mu)$ for events with $E_\mu \geq 10$ TeV.

This work concludes that, in spite of the detector size at this first construction phase, interesting scientific findings can be expected from the ARCA installation with reasonable sensitivity. Improved results can be obtain by performing a multivariate analysis to better identify background events and also by taking into account cascade-like events.

References

- [1] M. A. MARKOV AND I. M. ZHELEZNYKH. **On high energy neutrino physics in cosmic rays.** *Nuclear Physics*, **27**(3):385–394, 1961. 5
- [2] AGATA TROVATO. *Development of reconstruction algorithms for large volume neutrino telescopes and their application to the KM3NeT detector.* PhD thesis, Università degli Studi di Catania, 2013. 7, 12, 14, 91, 95, 96
- [3] FRANCK BERNARD. *Caractérisation des performances d’un télescope sous-marin à neutrinos pour la détection de cascades contenues dans le cadre du projet ANTARES.* PhD thesis, Université de la Méditerranée Aix-Marseille II, 2000. 7
- [4] J. A. FORMAGGIO AND G. P. ZELLER. **From eV to EeV: Neutrino cross sections across energy scales.** *Rev. Mod. Phys.*, **84**:1307–1341, 2012. 8, 9
- [5] M. G. AARTSEN ET AL. **Measurement of the multi-TeV neutrino cross section with IceCube using Earth absorption.** *Nature*, 2017. 8, 9
- [6] RAJ GANDHI, CHRIS QUIGG, MARY HALL RENO, AND INA SARCEVIC. **Ultra high-energy neutrino interactions.** *Astroparticle Physics*, **5**(2):81–110, 1996. 10
- [7] RAJ GANDHI, CHRIS QUIGG, MARY HALL RENO, AND INA SARCEVIC. **Neutrino interactions at ultrahigh-energies.** *Physical Review D*, **58**:093009, 1998. 11
- [8] C. CARLOGEANU. **Muon interactions at high energies, ANTARES-Physics.** (1998-003), 1998. 13

REFERENCES

- [9] GIORGIO RICCOBENE AND ANTONIO CAPONE. **Deep seawater inherent optical properties in the Southern Ionian Sea.** *Astroparticle Physics*, **27**:1–9, 2007. 16, 31, 79
- [10] CURTIS D. MOBLEY. *Light and Water: Radiative Transfer in Natural Waters.* Academic Press, 1994. 16
- [11] S. ADRIAN-MARTINEZ ET AL. **Long term monitoring of the optical background in the Capo Passero deep-sea site with the NEMO tower prototype.** *Eur. Phys. J.*, **C76(2)**:68, 2016. 19, 20, 24
- [12] S. AIELLO ET AL. **Measurement of the atmospheric muon depth intensity relation with the NEMO Phase-2 tower.** *Astroparticle Physics*, **66**:1–7, 2015. 22
- [13] S. AIELLO ET AL. **The optical modules of the phase-2 of the NEMO project.** *Journal of Instrumentation*, **8(07)**:P07001, 2013. 25
- [14] S. VIOLA ET AL. **Underwater acoustic positioning system for the SMO and KM3NeT - Italia projects.** *AIP Conference Proceedings*, **1630(1)**, 2014. 25
- [15] **IceCube website** <https://icecube.wisc.edu>. 26
- [16] **KM3NeT website** <http://www.km3net.org>. 29, 34, 38
- [17] KM3NET COLLABORATION. **Letter of Intent for KM3NeT 2.0.** *Journal of Physics G: Nuclear and Particle Physics*, **43(8)**:084001, 2016. 33, 34, 36, 38, 72, 119, 128
- [18] S. ADRIAN-MARTINEZ ET AL. **Deep sea tests of a prototype of the KM3NeT digital optical module.** *Eur. Phys. J.*, **C74(9)**:3056, 2014. 35, 48
- [19] S. ADRIAN-MARTINEZ ET AL. **The prototype detection unit of the KM3NeT detector.** *Eur. Phys. J.*, **C76(2)**:54, 2016. 35, 43, 44, 47, 48
- [20] THE KM3NET COLLABORATION. **Expansion cone for the 3-inch PMTs of the KM3NeT optical modules.** *Journal of Instrumentation*, **8(03)**:T03006, 2013. 38, 40

-
- [21] KAREL MELIS. **In-Situ Calibration of KM3NeT.** *Proceedings of Science for the 35th International Cosmic Ray Conference*, 2017. 42, 46
- [22] MARTIJN JONGEN. **Measurement of the depth dependence of coincidence rates induced by atmospheric muons with the first two KM3NeT Detection Units.** *Proceedings of Science for the 35th International Cosmic Ray Conference*, 2017. 49, 50
- [23] **Website** <http://http://www.physics.utah.edu/whanlon/spectrum.html>. 52
- [24] T. STANEV. *High Energy Cosmic Rays*. Springer Praxis Books, 2004. 53
- [25] T. K. GAISSER. *Cosmic Rays and Particle Physics*. Cambridge University Press, 1990. 53
- [26] M. NAGANO AND A. A. WATSON. **Observations and implications of the ultrahigh-energy cosmic rays.** *Reviews of Modern Physics*, **72**:689–732, 2000. 53
- [27] JORG R. HORANDEL. **The origin of galactic cosmic rays.** *Nuclear Instruments and Methods in Physics Research Section A: Accelerators, Spectrometers, Detectors and Associated Equipment*, **588**(1):181–188, 2008. Proceedings of the First International Conference on Astroparticle Physics. 53
- [28] V. F. HESS. *Phys. Zeits.*, **14**:1153, 1912. 53
- [29] **AUGER website** <http://www.auger.org>. 53
- [30] **Telescope Array website** <http://www.telescopearray.org>. 53
- [31] P. O. LAGAGE AND C. J. CESARSKY. **The maximum energy of cosmic rays accelerated by supernova shocks.** *Astronomy and Astrophysics*, **125**:249–257, 1983. 53
- [32] KARL-HEINZ KAMPERT AND MICHAEL UNGER. **Measurements of the cosmic ray composition with air shower experiments.** *Astroparticle Physics*, **35**(10):660–678, 2012. 54

REFERENCES

- [33] KENNETH GREISEN. **End to the Cosmic-Ray Spectrum?** *Physical Review Letters*, **16**:748–750, 1966. 54
- [34] G. T. ZATSEPIN AND V. A. KUZMIN. **Upper Limit of the Spectrum of Cosmic Rays.** *Soviet Journal of Experimental and Theoretical Physics Letters*, **4**:78, 1966. 54
- [35] R. ABBASI ET AL. **Measurement of the Flux of Ultrahigh Energy Cosmic Rays from Monocular Observations by the High Resolution Fly’s Eye Experiment.** *Physical Review Letters*, **92**:151101, 2004. 55
- [36] J. ABRAHAM ET AL. *Physics Letters B*, **685**:239, 2010. 55
- [37] T. ABU-ZAYYAD ET AL. **The Cosmic-Ray Energy Spectrum Observed with the Surface Detector of the Telescope Array Experiment.** *The Astrophysical Journal Letters*, **768**(1):L1, 2013. 55
- [38] H. ATHAR, M. JEZABEK, AND O. YASUDA. **Effects of neutrino mixing on high-energy cosmic neutrino flux.** *Physical Review*, **D62**:103007, 2000. 58
- [39] JULIA K. BECKER. **High-energy neutrinos in the context of multimessenger physics.** *Phys. Rept.*, **458**:173–246, 2008. 59
- [40] A. ALBERT ET AL. **New constraints on all flavor Galactic diffuse neutrino emission with the ANTARES telescope.** *Phys. Rev. D*, **96**(6):062001, 2017. 60
- [41] CHRISTIAN HAACK AND JON DUMM. **Constraints on diffuse neutrino emission from the Galactic Plane with 7 years of IceCube data.** *Proceedings of Science for the 35th International Cosmic Ray Conference*, 2017. 60
- [42] CHARLES D. DERMER AND KURT E. MITMAN. **Short-Timescale Variability in the External Shock Model of Gamma-Ray Bursts.** *The Astrophysical Journal Letters*, **513**(1):L5, 1999. 61
- [43] R. V. E. LOVELACE. **Dynamo model of double radio sources.** *Nature*, **262**:649, 1976. 62

-
- [44] M. G. AARTSEN ET AL. **The Contribution of Fermi-2LAC Blazars to Diffuse TeV–PeV Neutrino Flux.** *The Astrophysical Journal*, **835**(1):45, 2017. 62
- [45] T. PIRAN. **Gamma-ray bursts and the fireball model.** *Physics Reports*, **314**:575–667, 1999. 62
- [46] ELI WAXMAN. **Gamma-Ray-Burst Afterglow: Supporting the Cosmological Fireball Model, Constraining Parameters, and Making Predictions.** *The Astrophysical Journal Letters*, **485**(1):L5, 1997. 62
- [47] M. G. AARTSEN ET AL. **An All-sky Search for Three Flavors of Neutrinos from Gamma-ray Bursts with the IceCube Neutrino Observatory.** *The Astrophysical Journal*, **824**(2):115, 2016. 62
- [48] M. AMBROSIO ET AL. **Search for diffuse neutrino flux from astrophysical sources with MACRO.** *Astropart. Phys.*, **19**:1–13, 2003. 63
- [49] A. V. AVRORIN ET AL. **Search for high-energy neutrinos in the Baikal neutrino experiment.** *Astron. Lett.*, **35**:651, 2009. 63
- [50] ELI WAXMAN AND JOHN N. BAHCALL. **High-energy neutrinos from astrophysical sources: An Upper bound.** *Physical Review D*, **59**:023002, 1999. 63, 64, 67
- [51] KARL MANNHEIM, R. J. PROTHEROE, AND JORG P. RACHEN. **On the cosmic ray bound for models of extragalactic neutrino production.** *Physical Review D*, **63**:023003, 2001. 63, 64
- [52] R. ABBASI ET AL. **First search for extremely high energy cosmogenic neutrinos with the IceCube Neutrino Observatory.** *Physical Review D*, **82**:072003, 2010. 65, 70, 71
- [53] R. ABBASI ET AL. **Constraints on the Extremely-high Energy Cosmic Neutrino Flux with the IceCube 2008-2009 Data.** *Physical Review D*, **83**:092003, 2011. [Erratum: Phys. Rev.D84,079902(2011)]. 65, 70, 71
- [54] R. ABBASI ET AL. **A Search for a Diffuse Flux of Astrophysical Muon Neutrinos with the IceCube 40-String Detector.** *Physical Review D*, **84**:082001, 2011. 65, 67, 70, 71

REFERENCES

- [55] M. G. AARTSEN ET AL. **Search for neutrino-induced particle showers with IceCube-40.** *Physical Review D*, **89**:102001, 2014. 65, 70, 71
- [56] M. G. AARTSEN ET AL. **First observation of PeV-energy neutrinos with IceCube.** *Phys. Rev. Lett.*, **111**:021103, 2013. 65, 70, 71
- [57] M. G. AARTSEN ET AL. **Evidence for High-Energy Extraterrestrial Neutrinos at the IceCube Detector.** *Science*, **342**:1242856, 2013. 65, 70, 71
- [58] M. G. AARTSEN ET AL. **Search for a diffuse flux of astrophysical muon neutrinos with the IceCube 59-string configuration.** *Physical Review D*, **89**:062007, 2014. 66, 67, 70, 71
- [59] ELI WAXMAN. **High energy cosmic ray and neutrino astronomy.** 2011. 67
- [60] A. ACHTERBERG ET AL. **Multi-year search for a diffuse flux of muon neutrinos with AMANDA-II.** *Physical Review D*, **76**:042008, 2007. [Erratum: *Phys. Rev.D*77,089904(2008)]. 67
- [61] J. A. AGUILAR ET AL. **Search for a diffuse flux of high-energy ν_μ with the ANTARES neutrino telescope.** *Physics Letters B*, **696**:16–22, 2011. 67
- [62] M. G. AARTSEN ET AL. **Observation of High-Energy Astrophysical Neutrinos in Three Years of IceCube Data.** *Phys. Rev. Lett.*, **113**:101101, 2014. 67, 68, 70, 71
- [63] C. KOPPER, W. GIANG, AND N. KURAHASHI. **Observation of Astrophysical Neutrinos in Four Years of IceCube Data.** *Proceedings of Science for the 34th International Cosmic Ray Conference*, 2015. 67, 68
- [64] C. KOPPER. **Observation of Astrophysical Neutrinos in Six Years of IceCube Data.** *Proceedings of Science for the 35th International Cosmic Ray Conference*, 2017. 67, 68
- [65] IGNACIO TABOADA. **A View of the Universe with the IceCube and ANTARES Neutrino Telescopes**, 2018. 67

-
- [66] M. G. AARTSEN ET AL. **Atmospheric and astrophysical neutrinos above 1 TeV interacting in IceCube.** *Physical Review D*, **91**(2):022001, 2015. 68, 70, 71
- [67] M. G. AARTSEN ET AL. **Flavor Ratio of Astrophysical Neutrinos above 35 TeV in IceCube.** *Phys. Rev. Lett.*, **114**(17):171102, 2015. 68, 70, 71
- [68] M. G. AARTSEN ET AL. **A combined maximum-likelihood analysis of the high-energy astrophysical neutrino flux measured with IceCube.** *Astrophys. J.*, **809**(1):98, 2015. 69, 70, 71, 72, 73
- [69] L. MOHRMANN. **Combined Analysis of the High-Energy Cosmic Neutrino Flux at the IceCube Detector.** *Proceedings of Science for the 34th International Cosmic Ray Conference*, 2015. 69
- [70] M. G. AARTSEN ET AL. **Probing the origin of cosmic rays with extremely high energy neutrinos using the IceCube Observatory.** *Physical Review D*, **88**:112008, 2013. 70, 71
- [71] M. G. AARTSEN ET AL. **Evidence for Astrophysical Muon Neutrinos from the Northern Sky with IceCube.** *Phys. Rev. Lett.*, **115**(8):081102, 2015. 70, 71
- [72] M. G. AARTSEN ET AL. **Observation and Characterization of a Cosmic Muon Neutrino Flux from the Northern Hemisphere Using Six Years of IceCube Data.** *The Astrophysical Journal*, **833**(1):3, 2016. 70, 71, 72, 73
- [73] LEIF RADEL AND SEBASTIAN SCHOENEN. **A measurement of the diffuse astrophysical muon neutrino flux using multiple years of IceCube data.** *Proceedings of Science for the 34th International Cosmic Ray Conference*, 2015. 70, 71
- [74] CHRISTIAN HAACK AND C. WIEBUSCH. **A measurement of the diffuse astrophysical muon neutrino flux using eight years of IceCube data.** *Proceedings of Science for the 35th International Cosmic Ray Conference*, 2017. 70, 71
- [75] T. K. GAISSER AND M. HONDA. **Flux of atmospheric neutrinos.** *Ann. Rev. Nucl. Part. Sci.*, **52**:153–199, 2002. 74, 77

REFERENCES

- [76] VIVEK AGRAWAL, T. K. GAISSER, PAOLO LIPARI, AND TODOR STANEV. **Atmospheric neutrino flux above 1 GeV.** *Physical Review D*, **53**:1314–1323, 1996. 75
- [77] G. D. BARR, T. K. GAISSER, P. LIPARI, S. ROBBINS, AND T. STANEV. **Three-dimensional calculation of atmospheric neutrinos.** *Physical Review D*, **70**:023006, 2004. 75
- [78] M. HONDA, T. KAJITA, K. KASAHARA, S. MIDORIKAWA, AND T. SANUKI. **Calculation of atmospheric neutrino flux using the interaction model calibrated with atmospheric muon data.** *Physical Review D*, **75**:043006, 2007. 75, 85, 115
- [79] R. ABBASI ET AL. **Measurement of the atmospheric neutrino energy spectrum from 100 GeV to 400 TeV with IceCube.** *Phys. Rev. D*, **83**:012001, 2011. 75
- [80] M. G. AARTSEN ET AL. **Measurement of the Atmospheric ν_e flux in IceCube.** *Phys. Rev. Lett.*, **110**(15):151105, 2013. 75
- [81] G. BATTISTONI, A. FERRARI, P. LIPARI, T. MONTARULI, P.R. SALA, AND T. RANCATI. **A 3-dimensional calculation of the atmospheric neutrino fluxes.** *Astroparticle Physics*, **12**(4):315–333, 2000. 75
- [82] C. G. S. COSTA. **The prompt lepton cookbook.** *Astroparticle Physics*, **16**:193–204, 2001. 76
- [83] RIKARD ENBERG, MARY HALL RENO, AND INA SARCEVIC. **Prompt neutrino fluxes from atmospheric charm.** *Physical Review D*, **78**:043005, 2008. 77, 85, 115
- [84] CLANCY W. JAMES. *KM3NeT Internal Note, KM3NeT-Software*, (2016-003), 2016. 81
- [85] SHELDON L. GLASHOW. **Resonant Scattering of Antineutrinos.** *Physical Review*, **118**:316–317, 1960. 82, 107
- [86] STANISLAW JADACH, JOHANN H. KUHN, AND ZBIGNIEW WAŚ. **TAUOLA - a library of Monte Carlo programs to simulate decays of polarized leptons.** *Computer Physics Communications*, **64**(2):275–299, 1991. 82

-
- [87] G. INGELMAN, A. EDIN, AND J. RATHSMAN. **LEPTO 6.5: A Monte Carlo generator for deep inelastic lepton - nucleon scattering.** *Comput. Phys. Commun.*, **101**:108–134, 1997. 83
- [88] GILES DAVID BARR. *The separation of signals and background in a nucleon decay experiment.* PhD thesis, University of Oxford, 1987. 83
- [89] JÜRGEN BRUNNER. **Updated tag list for the new ANTARES event format.** *ANTARES Internal Note, ANTARES Software*, (1999-003), 1999. 84, 107
- [90] ADAM M. DZIEWONSKI AND DON L. ANDERSON. **Preliminary reference Earth model.** *Physics of the Earth and Planetary Interiors*, **25**(4):297–356, 1981. 86
- [91] DAVID J. L. BAILEY. *Monte Carlo tools and analysis methods for understanding the ANTARES experiment and predicting its sensitivity to Dark Matter.* PhD thesis, University of Oxford, 2002. 87, 105
- [92] D. HECK, G. SCHATZ, T. THOUW, J. KNAPP, AND J. N. CAPDEVIELLE. **CORSIKA: A Monte Carlo code to simulate extensive air showers.** (FZKA-6019), 1998. 87
- [93] Y. BECHERINI, A. MARGIOTTA, M. SIOLI, AND M. SPURIO. **A parameterisation of single and multiple muons in the deep water or ice.** *Astroparticle Physics*, **25**(1):1–13, 2006. 87
- [94] G. CARMINATI, M. BAZZOTTI, A. MARGIOTTA, AND M. SPURIO. **Atmospheric MUons from Parametric formulas: a fast GEnerator for neutrino telescope (MUPAGE).** *Computer Physics Communications*, **179**(12):915–923, 2008. 87
- [95] E. SCAPPARONE. **HEMAS: a Monte Carlo code for hadronic, electromagnetic and TeV muon components in air shower.** 1999. 87
- [96] A. MARGIOTTA. **ANTARES Internal note, ANTARES-Software.** (2004-002), 2004. 87

REFERENCES

- [97] F. RONGA. **Atmospheric neutrino induced muons in the MACRO detector.** *Nuclear Physics B - Proceedings Supplements*, **77**(1):117–122, 1999. 87
- [98] M. SIOLI. **Underground muon physics with the MACRO experiment.** *Nucl. Phys. Proc. Suppl.*, **85**:349–354, 2000. 87
- [99] P. ANTONIOLI, C. GHETTI, E. V. KOROLKOVA, V. A. KUDRYAVTSEV, AND G. SARTORELLI. **A Three-dimensional code for muon propagation through the rock: Music.** *Astropart. Phys.*, **7**:357–368, 1997. 87, 92
- [100] L. T. S. NAVAS. *ANTARES Internal Note, ANTARES-Software*, (1999-011), 1999. 89
- [101] **GEANT3.21 website** <http://wwwasd.web.cern.ch/wwwasd/geant>. 90
- [102] AART J. HEIJBOER. **Reconstruction of Atmospheric Neutrinos in Antares.** *Proceedings of Science for the 31st International Cosmic Ray Conference*, 2009. 95
- [103] MAARTEN DE JONG KAREL MELIS, AART HEIJBOER. **KM3NeT/ARCA Event Reconstruction Algorithms.** *Proceedings of Science for the 35th International Cosmic Ray Conference*, 2017. 97, 98
- [104] GARY C. HILL AND KATHERINE RAWLINS. **Unbiased cut selection for optimal upper limits in neutrino detectors: The Model rejection potential technique.** *Astroparticle Physics*, **19**:393–402, 2003. 112
- [105] GARY J. FELDMAN AND ROBERT D. COUSINS. **Unified approach to the classical statistical analysis of small signals.** *Physical Review D*, **57**:3873–3889, 1998. 112
- [106] LUIGI FUSCO, T. EBERL, S. NAVAS, AND F. VERSARI. **Search for a diffuse flux of cosmic neutrinos with the ANTARES telescope.** *Proceedings of Science for the 35th International Cosmic Ray Conference*, 2017. 119
- [107] JUTTA SCHNABEL. **Muon energy reconstruction in the ANTARES detector.** *Nuclear Instruments and Methods in Physics Research Section A*, **725**:106–109, 2013. 119